Lattice models for Josephson junctions and graphene superlattices

Proefschrift

ter verkrijging van
de graad van Doctor aan de Universiteit Leiden,
op gezag van Rector Magnificus prof. mr. C.J.J.M. Stolker,
volgens besluit van het College voor Promoties
te verdedigen op woensdag 27 juni 2018
klokke 15.00 uur

door

Viacheslav Ostroukh

geboren te Lugansk, Oekraïne in 1991

Promotor:	Prof. Dr. C. W. J. Beenakker
Co-promotor:	Dr. A. R. Akhmerov (TU Delft)
Promotiecommissie:	Dr. V. V. Cheianov
	Prof. Dr. E. R. Eliel
	Prof. Dr. Ir. L. P. Kouwenhoven (Microsoft & TU Delft)
	Prof. Dr. Ir. W. van Saarloos
	Dr. M. T. Wimmer (TU Delft)

Casimir PhD Series Delft-Leiden 2018-14
ISBN 978-90-8593-346-5
An electronic version of this thesis can be found
at `https://openaccess.leidenuniv.nl`

Cover: current distribution in a disordered graphene quantum dot (front), computed in a tight-binding model (back).

To my parents.
Моїм батькам.

Contents

Chapter 1

Introduction

1.1 Preface

The topic of this thesis is the modeling of electronic devices on the nanometer scale. The need for such modeling appears because modern device engineering requires going to lower and lower length scales, where classical circuit dynamics does not work anymore. The first commercially available microprocessor from the early 1970's, the Intel 4004 processor, had a minimal feature size of 10 micrometers. In 2018 we are approaching one thousand times smaller minimal dimensions. This 10 nanometer length scale is still two orders of magnitude above the atomic limit, but comparable to the electron wave length. A quantum mechanical modeling, including the effects of quantum interference, is required to properly describe these devices.

Our focus is on lattice models, which describe how the electron dynamics is modified by the periodic potential of the atomic lattice. The modification can be dramatic, as in graphene, a carbon monolayer, where the conduction electrons move through the honeycomb lattice of carbon atoms as if they were massless relativistic particles. We explore what happens if the electrons are subject to an additional "superlattice" from a copper substrate.

Superconductivity is a macroscopic quantum effect, that is modified as well on the nanoscale. We consider the induced superconductivity in topological insulators, which have an insulating bulk but a conducting surface or edge. In one of these investigations we have collaborated with an experimental group in Delft, so that our modelling could be directly

applied to the measured data.

In the next subsections we introduce the topics that will play a central role in the following chapters of the thesis.

1.2 Josephson junctions

A Josephson junction is a weak link between two superconductors. A dissipationless supercurrent can flow through the junction and it can be controlled by application of a magnetic field. For that reason a Josephson junction is the basic circuit element in superconducting technology. Applications include sensitive magnetometers [1], single-electron transistors [2], quantum computers (in flux [3], charge [4], or phase [5] qubits), scanning probe microscopy [6], and metrology [7, 8].

Our interest in Josephson junctions is as a probe of current-carrying paths in the junction region. Different paths will include different amounts of magnetic flux, so a study of the magnetic field dependence of the supercurrent will provide information on where the current flows. This is of particular interest if the junction is formed out of a topological insulator, which is predicted to have a current flow confined to the edge of the material.

1.2.1 Josephson effect

Superconductors are characterized by a complex order parameter $\Delta = |\Delta|e^{i\phi}$. The amplitude gives the energy gap for single-particle excitations from the ground state [9]. The gap appears because an effective attraction between electrons (which can have a variety of origins) imparts an energy penalty for the appearance of an unpaired single electron. The phase of Δ plays no role in a single homogenous superconductor, but when there is a weak link, a phase difference can drive a supercurrent. This is the Josephson effect.

The Josephson effect has two manifestations, as a stationary effect (DC) and as a time-dependent effect (AC). We will be only concerned with the DC Josephson effect. This effect is fully characterized by the dependence of the free energy $F(\phi)$ on the superconducting phase difference ϕ across the junction. The derivative gives the supercurrent according to

$$I(\phi) = \frac{2e}{\hbar}\frac{dF}{d\phi}. \tag{1.1}$$

Because ϕ appears as a phase factor $e^{i\phi}$ in the order parameter, all physical properties must be 2π-periodic functions of ϕ. This includes the supercurrent, $I(\phi) = I(\phi + 2\pi)$.

A periodic function must have a maximum value, this is called the critical current $I_c = \max_\phi I(\phi)$. The ϕ dependence can be complicated at low temperatures, but at elevated temperatures all harmonics except the lowest one are suppressed, and we have the simple relation

$$I(\phi) = I_c \sin \phi. \tag{1.2}$$

The size of the critical current depends on the properties of the junction. If the weak link is formed by a point contact I_c is quantized in units of $e|\Delta|/\hbar$ [10].

1.2.2 Fraunhofer oscillations and Dynes-Fulton relation

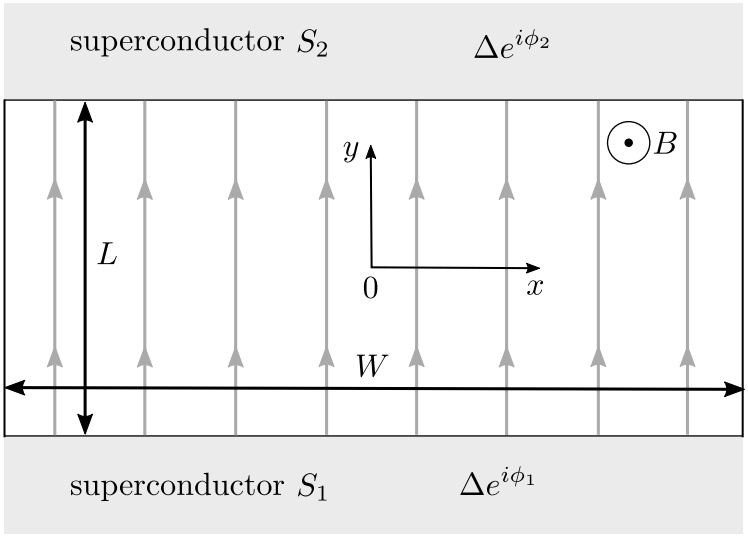

Figure 1.1. Schematic image of a Josephson junction. If the current is passing approximately along the y direction (grey arrows), the Dynes-Fulton analysis is applicable.

When a magnetic field B penetrates the junction region, the critical current depends on the enclosed flux in an oscillatory manner. These are called Fraunhofer oscillations, because the electron interference effect that gives rise to the oscillations is similar to the Fraunhofer diffraction pattern

in optics. We will use the Fraunhofer oscillations to find the current flow in the junction, and for that purpose we adopt a method developed by Dynes and Fulton [11].

We describe the method for a rectangular two-dimensional Josephson junction (se Fig. 1.1). Assume the existence of a local supercurrent density function $J(x, \phi)$, which is non-uniform because of some local inhomogeneities in the junction or, more interestingly, because of the edge states in a topological insulator. The magnetic-field dependence enters when we replace the phase ϕ by the gauge-invariant expression

$$\gamma(x) = \phi - \frac{2e}{\hbar} \int_{-L/2}^{L/2} A_y(x, y)\, dy = \phi - \frac{2e}{\hbar} BxL, \tag{1.3}$$

in the gauge $\mathbf{A} = (0, Bx, 0)$. The total current through the junction is

$$I(\phi, B) = \int_{-W/2}^{W/2} J(x, \phi - \frac{2e}{\hbar} BxL)\, dx. \tag{1.4}$$

We assume a sinusoidal current-phase relationship, $J(x, \phi) = J_c(x) \sin \phi$, with a spatially dependent critical current density $J_c(x)$. If the junction is $\pm x$ symmetric, so that $J_c(x)$ is an even function of x, we may decouple the coordinate and phase dependence,

$$I(\phi, B) = \left(\int_{-W/2}^{W/2} J_c(x) \cos\left(\frac{2e}{\hbar} BLx \right)\, dx \right) \sin \phi, \tag{1.5}$$

which leads to the critical current

$$I_c(B) = \left| \int_{-W/2}^{W/2} J_c(x) \cos\left(\frac{2e}{\hbar} BLx \right)\, dx \right|. \tag{1.6}$$

If $J_c(x)$ is uniform inside the junction, we recover the classical Fraunhofer pattern,

$$I_c(B) = I_c(0) \left| \frac{\sin(\pi\Phi/\Phi_0)}{\pi\Phi/\Phi_0} \right|, \tag{1.7}$$

where $\Phi = BWL$ is the total flux through the junction and $\Phi_0 = h/2e$ is the superconducting flux quantum. In contrast, if we have only edge currents, $J_c(x) = j_0 \left[\delta(x + W/2) + \delta(x - W/2)\right]$, we obtain an entirely different B-dependence,

$$I_c(B) = I_c(0) \left| \cos(\pi\Phi/\Phi_0) \right|, \tag{1.8}$$

characteristic of a SQUID (a superconducting quantum interference device).

More generally, the dependence $J_c(x)$ can be extracted from the measured $I_c(B)$ by a Fourier transformation,

$$J_c(x) = \frac{L}{\Phi_0} \int_{-\infty}^{\infty} \tilde{I}_c(B) \cos\left(2\pi BLx/\Phi_0\right) dB. \tag{1.9}$$

The tilde $\tilde{I}$ indicates that one should distinguish $+I_c$ from $-I_c$. In practice this means that one has to switch between + and − every time, when $I_c(B)$ touches zero.

The Dynes-Fulton analysis is simple and informative, but the basic assumption of a local supercurrent density function can give false results. In fact, Chapters 2, 3, and 4 describe situations where we must go beyond this approximation.

1.3 Graphene superlattices

Materials consisting of single-atom monolayers are actively studied for two main reasons: Firstly, due to effectively 2D physics, they often have unique physical properties. Secondly, they fit well into the modern electronics design, where elements are primarily located on a surface. For many decades it was assumed that monolayers are not thermodynamically stable, but would roll up as a scroll. We now know that this does not necessarily happen. Andre Geim and Konstantin Novoselov were awarded the 2010 Nobel Prize for their demonstration that carbon can form a stable monolayer, called graphene. The European Union research initiative "Graphene Flagship" [12] aims at bringing graphene and other 2D materials from scientific laboratories to industrial applications.

Our research has addressed a particular topic in this arena, the modification of graphene by a periodic potential imposed by a commensurate substrate, forming a "superlattice".

1.3.1 Electronic properties

Graphene has a honeycomb lattice consisting of two triangular sublattices. The unit cell has two atoms, labeled A and B. The tight-binding Hamiltonian is

$$H = -t \sum_{\langle i,j \rangle} (a_i^\dagger b_j + b_i^\dagger a_j), \tag{1.10}$$

with $\langle i, j \rangle$ indicating nearest neighbor atoms. The nearest-neighbor hopping amplitude is t, and a, b denote fermion annihilation operators on the A and B sublattice. Atoms on the same sublattice are not coupled by nearest-neighbor hopping.

The first Brillouin zone is a hexagon, with a band structure that has a conical singularity (a socalled Dirac point) at the corners of the hexagon. Near a corner the Hamiltonian can be linearized in momentum $\mathbf{k}$, resulting in the Dirac Hamiltonian

$$H = \hbar v_F \begin{pmatrix} 0 & k_x - ik_y \\ k_x + ik_y & 0 \end{pmatrix} = \hbar v_F (k_x \sigma_x + k_y \sigma_y). \tag{1.11}$$

This 2×2 matrix operator acts on a two-component wave function $\psi = (\psi_A, \psi_B)$, containing the wave amplitudes on the A and B sublattice. The Pauli matrices σ_x and σ_y are called "pseudospin" operators, because this sublattice degree of freedom is not a real spin. (The real spin plays no role in zero magnetic field.)

The energy spectrum of this Hamiltonian forms a Dirac cone,

$$E(\mathbf{k}) = \pm \hbar v_F |\mathbf{k}|. \tag{1.12}$$

The Fermi velocity $v_F = 3ta/2 \approx 10^6$ m/s plays the role of the speed of light in the relativistic Dirac equation for particles without mass. For this reason electrons in graphene are often referred as "massless". The Hamiltonian (1.11) has the property that the current operator

$$\mathbf{j} = \frac{\partial H}{\partial \mathbf{k}} = v_F \boldsymbol{\sigma} \tag{1.13}$$

locks the sublattice degree of freedom to the direction of propagation — one speaks of "pseudospin-momentum locking".

In particle physics there is the notion that massless electrons on a lattice must come in pairs, an effect known as "fermion-doubling". The same effect is operative in graphene: the two opposite corners of the hexagonal Brillouin zone, labeled K and K', are not related by a reciprocal lattice vector, so they are inequivalent "valleys" in the bandstructure. Each produces a massless Dirac fermion, described by the same Hamiltonian (1.11). The valley degree of freedom could be used to store information, and by analogy with electronics (information processing using the electron charge) and spintronics (spin-based information processing) one speaks of "valleytronics".

In this thesis we will propose a way to control the valley degree of freedom by means of a superlattice potential of the Kekulé type.

1.3.2 Kekulé-type superlattices

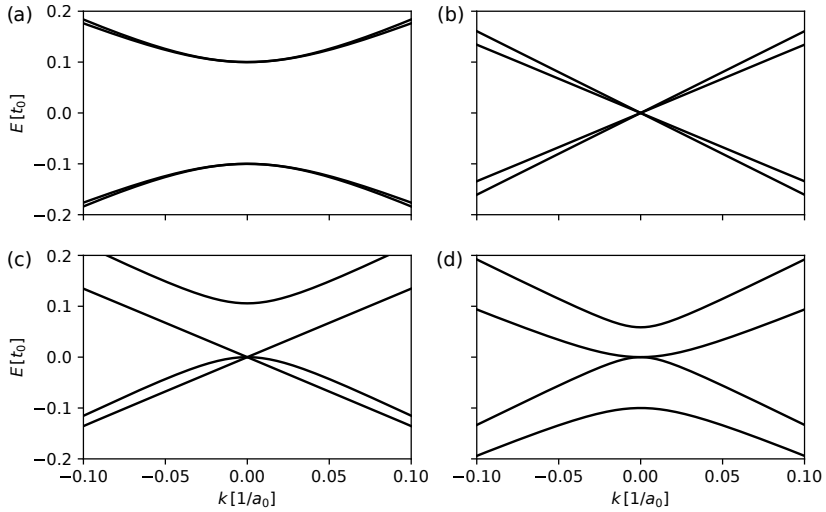

Figure 1.2. Four types of low-energy dispersion relations for the family of graphene superlattices with 6 atoms in the unit cell. The threefold enlargement of the unit cell (scaled by $\sqrt{3} \times \sqrt{3}$) folds the K and K' Dirac points onto the center of the Brillouin zone (the Γ point). Panels (a) and (b) correspond to a hopping amplitude modulation of Kekulé-O type (panel a) or Kekulé-Y type (panel b). Panels (c) and (d) correspond to a modulation of the atomic potential, resulting in a linear triple-point crossing (panel c) or a quadratic band crossing (panel d).

If graphene is deposited epitaxially on a substrate with the same honeycomb lattice, the dominant effect of the substrate is to couple the K and K' valleys of the Dirac fermions [13, 14]. The effect depends on whether the substrate predominantly modulates the hopping amplitudes or the atomic potentials. When the hopping amplitudes are modulated one speaks of a Kekulé-type superlattice. This name refers to the bond modulation in a benzene ring, studied by the chemist August Kekulé. Four different types of bandstructures in a graphene superlattice are shown in Fig. 1.2.

Our study of Kekulé-type graphene superlattices was motivated by an experiment performed by Gutierrez *et al.* [15], who realized a Y-shaped bond modulation by placing graphene on top of a copper substrate. That experiment was interpreted in terms of a gapped spectrum, as in panel

(a) of Fig. 1.2, however as we will show in Chapter 5, the spectrum remains gapless as in panel (b) — but with an unexpected valley-momentum locking.

1.4 Lattice models

Due to the rise of numerical computational power, numerical modeling on a lattice is one of the most important methods in modern science. Approximating a continuous differential or integral equation with a matrix analog on a space-time grid is a natural way to reformulate a problem for the machine, if analytical methods are not capable to solve it. Moreover, in practice often it happens also vice versa: numerical modeling can give some tips for actual way of solving the problem or point out interesting parameter regimes to explore.

Often lattice models also arise naturally from the system structure. First of all, this is an atomic-scale tight-binding model. Each atom is represented as a vertex on a graph, and interactions between them are bonds between these vertices. This graph can be mapped to the Hamiltonian matrix, if we know onsite energies for each vertex and hopping integrals for each bond [16]. These unknown values can be taken, for example, from density functional theory simulations, $k \cdot p$ perturbation theory, or from experiment. In general, lattice models are convenient to use whenever the system has some kind of sparse structure. This sparsity need not be obvious at first sight. For example, in Chapter 2 the sparse structure arises not from the microscopic but from the macroscopic properties of the device, namely, the existence of edge states.

1.4.1 Current calculations in tight-binding formalism

Experiments typically probe the system by measuring the electrical current, so that is the quantity we are most interested in when we perform a calculation. Here we briefly describe how the electrical current can be obtained from a lattice model.

We start with a general form of a many-body tight-binding Hamiltonian for non-interacting particles on a lattice:

$$H = -\sum_{i,j} H_{ij} c_i^\dagger(t) c_j(t). \tag{1.14}$$

This Hamiltonian naturally appears either from discretization of a continuous one (then usually square lattice is used), or from microscopic material structure (typical example of this is graphene, each lattice site then represents a real atom). We work in the Heisenberg representation where operators that do not commute with the Hamiltonian are time dependent.

Let us split our system into two arbitrary parts A and B and compute the current I_{BA} from part A to part B,

$$I_{BA} = \frac{dQ_B}{dt} = -e\left\langle \frac{dN_B}{dt} \right\rangle, \tag{1.15}$$

where $N_B(t) = \sum_{i\in B} c_i^\dagger(t)c_i(t)$ is a number operator of part B. Using the Heisenberg equation of motion and the fermionic commutation relations, we may rewrite this as

$$I_{BA} = \frac{ie}{\hbar}\langle [N_B, H]\rangle = \frac{ie}{\hbar}\left\langle \sum_{i\in B}\sum_{j\in A} H_{ij}c_i^\dagger(t)c_j(t) - H_{ji}c_j^\dagger(t)c_i(t) \right\rangle. \tag{1.16}$$

With the help of the lesser Green's function

$$G_{ij}^<(t,t') = \frac{i}{\hbar}\left\langle c_j^\dagger(t')c_i(t)\right\rangle,$$

this expression becomes

$$I_{BA} = e\sum_{i\in B}\sum_{j\in A}\left(H_{ij}G_{ji}^<(t,t) - H_{ji}G_{ij}^<(t,t)\right). \tag{1.17}$$

This expression is convenient for a computation in a tight-binding model, because it takes advantage from the sparsity of the Hamiltonian. We have to compute only those values of the Green's function, that correspond to hoppings which conect subsystems A and B. Usually the number of such sites is much less than the size of a system itself.

In equilibrium the Green's function depends only on the time difference

$$G_{ij}^<(t,t') = G_{ij}^<(t-t',0),$$

which means that we may replace $G_{ij}^<(t,t)$ in Eq. (1.17) with $G_{ij}^<(0,0)$. To compute it, we take a Fourier transform and switch to the frequency domain,

$$\begin{aligned} G_{ij}^<(\omega) &= \int_{-\infty}^{+\infty} G_{ij}^<(t,0)e^{i\omega t}dt, \\ G_{ij}^<(t,t') &= \frac{1}{2\pi}\int_{-\infty}^{+\infty} G_{ij}^<(\omega)e^{-i\omega(t-t')}d\omega. \end{aligned} \tag{1.18}$$

To compute these expressions, let us define the retarded and advanced Green's functions,

$$\begin{aligned} G^R_{ij}(t,t') &= -\frac{i}{\hbar}\Theta(t-t')\left\langle\left\{c_i(t), c_j^\dagger(t')\right\}\right\rangle, \\ G^A_{ij}(t,t') &= \frac{i}{\hbar}\Theta(t'-t)\left\langle\left\{c_i(t), c_j^\dagger(t')\right\}\right\rangle. \end{aligned} \tag{1.19}$$

As it is shown in [17], their Fourier transforms have a convenient form for numerical computation,

$$G^{R/A}_{ij}(\omega) = (\hbar\omega - H \pm i\eta)^{-1}. \tag{1.20}$$

which in a finite system requires a numerical inversion of the Hamiltonian. For an infinite system it needs to be modified by inclusion of the self-energy of the translation-invariant part of the system Σ^R or Σ^A, usually referred to as a "lead":

$$G^{R/A}_{ij}(\omega) = \left(\hbar\omega - H - \Sigma^{R/A} \pm i\eta\right)^{-1}. \tag{1.21}$$

In this thesis we make use of the Kwant toolbox [16], which implements the calculation of the Green's functions for arbitrary tight-binding Hamiltonians.

Once we have determined the Green's functions, we proceed as follows. In equilibrium one has [17, 18]

$$G^<_{ij}(\omega) = i f_0(\hbar\omega) A_{ij}(\omega), \tag{1.22}$$

where $f_0(\epsilon) = (\epsilon/k_BT + 1)^{-1}$ is the Fermi distribution function at energy ϵ and temperature T. The quantity $A_{ij}(\omega)$ is the socalled spectral density, defined by

$$A_{ij}(\omega) = i\left(G^R_{ij}(\omega) - G^A_{ij}(\omega)\right). \tag{1.23}$$

Using this relation, we may write the Green's function in Eq. (1.17) as

$$G^<_{ij}(0,0) = -\frac{1}{2\pi}\int_{-\infty}^{+\infty} f_0(\hbar\omega)\left(G^R_{ij}(\omega) - G^A_{ij}(\omega)\right)d\omega. \tag{1.24}$$

We can evaluate this integral by contour integration in the complex energy plane. The Fermi distribution function has poles at $\omega = i\omega_p$, where $\omega_p = (2p+1)\pi k_BT/\hbar$ for integer p is a fermionic Matsubara frequency. The retarded Green's function has poles only in lower half of the complex

plane, and the advanced Green's function only in the upper half. Closing the contour in the upper half of the complex plane for the retarded Green's function and in the lower half for the advanced Green's function, and evaluating the integrals by summing over the residues at the poles, we arrive at

$$G_{ij}^{<}(0,0) = i\frac{k_B T}{\hbar} \sum_{p=-\infty}^{+\infty} G_{ij}^{R}(i\omega_p). \tag{1.25}$$

Now we may insert this into Eq. (1.17) to obtain an equation for the equilibrium current,

$$\begin{aligned} I_{BA} &= i\frac{ek_B T}{\hbar} \sum_{p=-\infty}^{+\infty} \sum_{i\in B} \sum_{j\in A} H_{ij} G_{ji}^{R}(i\omega_p) - H_{ji} G_{ij}^{R}(i\omega_p) \\ &= 2\frac{ek_B T}{\hbar} \sum_{p=0}^{+\infty} \sum_{i\in B} \sum_{j\in A} \Im\left(H_{ji} G_{ij}^{R}(i\omega_p) - H_{ij} G_{ji}^{R}(i\omega_p)\right). \end{aligned} \tag{1.26}$$

This result forms the basis of our calculations of the supercurrent through a Josephson junction.

1.5 This thesis

Here we will give a brief overview of what will be explored in this thesis.

1.5.1 Chapter 2

Work, represented in this chapter, was motivated by V. S. Pribiag *et. al.* [19] (at that moment this paper was not yet published). Authors were performing superconducting quantum interference measurements in Josephson junctions, made with InAs/GaSb quantum wells. InAs/GaSb is a two-dimensional topological insulator [20, 21], therefore we expect existence of helical quantum spin Hall edge modes in the regime, when Fermi energy is inside the topological gap. This means, that SNS junction can be driven by gate from bulk-dominated regime to edge dominated (when the transport happens through the helical modes, and bulk is gapped). This transition was indeed observed in the SQI measurements, alongside with more peculiar phenomenon, displayed on the Fig. 1.3.

In the edge-dominated regime, in addition to expected SQUID-like dependency of switching current on transversal magnetic field (series of

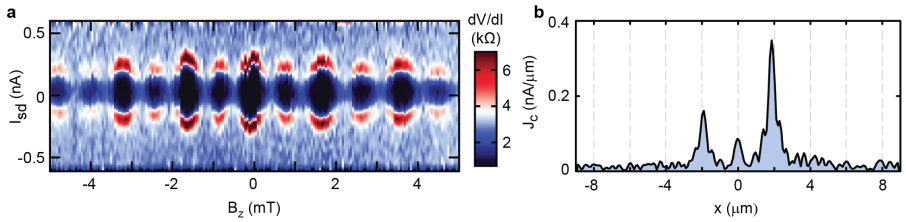

Figure 1.3. (a) Quantum interference pattern in Josephson junction with edge-dominated transport through normal part, that demonstrates $2\Phi_0$ periodicity in SQUID-like Josephson junction instead of expected Φ_0. Taken from Ref. [19]. (b) Current profile through the bulk of the junction, assuming validity of Dynes-Fulton analysis [11]. This picture was our original motivation for the research, represented in Chapter 2. Reprinted by permission from Springer Customer Service Centre GmbH: Springer Nature, Nature Nanotechnology, V. S. Pribiag, A. J. A. Beukman, F. Qu, M. C. Cassidy, C. Charpentier *et al.*, "Edge-mode superconductivity in a two-dimensional topological insulator", Nature Nanotech. **10**, 593–597 (2015), Copyright 2015.

equally spaced peaks of equal height with period of Φ_0/A, where A is area of Josephson junction and $\Phi_0 = h/2e$ is a superconducting flux quantum), authors observed a modulation between peaks amplitude, usually referred to as even-odd effect or $2\Phi_0$-periodicity. This could be explained by the fermion-parity anomaly [22], but would require quasiparticle poisoning time of order of tens of seconds [23], therefore it was extremely unlikely. Other possibility would be an existence of a conducting channel in the middle of SNS junction, but this requires fine-tuning and improbable to occur in different devices, which happened in the experiments.

In this chapter we build a phenomenological model, that assumes existence of scattering between opposite quantum spin Hall edges along the NS interfaces, that is formed due to the influence of superconductor, locally pushing the Fermi level from the topological gap to conduction band. This opens several paths for even-odd beating in critical current to occur (see Fig. 2.1). To describe the effect quantitatively, we build a network model of quantum spin Hall Josephson junction and explore the relative amplitude of even-odd beating versus coupling strength between helical edge channel and non-helical channel near the NS interface of the junction.

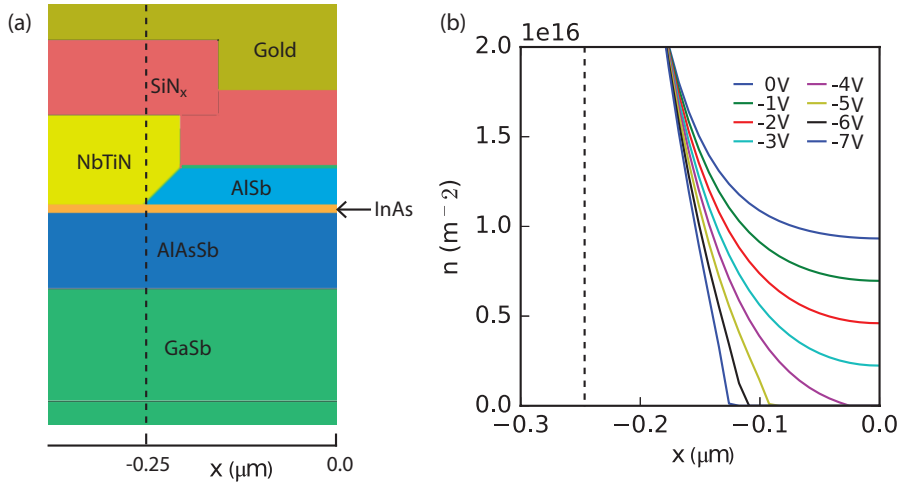

Figure 1.4. Schematic image of NS contact in experiment from Chapter 3. (a) Geometry of NS contact, that leads to the formation of a conducting channel along it, that enables transport between InAs edge channels. As it is shown in Chapter 2, this can lead to even-odd beating on top of SQUID-like quantum interference pattern. (b) Results of electrostatic simulations, that are performed using a finite element Poisson solver, based on this geometry. The electron density profile is changing as the top and bottom gate voltages are swept. The top gate voltage is indicated in the legend. In the lower gate voltage traces the electrons in the bulk are depleted while there is still a large electron density in the vicinity of the contacts. For clarification, the x-axis value where the NbTiN contact is on top of the InAs is indicated by the dashed line in both (a) and (b). The top gate is screened close to the contacts due to the triangular shape of the top AlSb barrier. Reprinted with permission from F. K. de Vries, T. Timmerman, V. P. Ostroukh, J. van Veen *et. al.*, Phys. Rev. Lett. **120**, 047702 (2018). Copyright 2018 by the American Physical Society.

1.5.2 Chapter 3

This chapter naturally continues the work from Chapter 2. At that moment it was already clarified, that alongside with topological edge channels, InAs/GaSb can host also trivial ones due to Fermi level pinning. Here we focus on superconducting transport through these trivial edges. Similarly to the previous chapter, we explore SNS junction, using superconducting quantum interference measurements and varying chemical potential in the normal part using top and bottom gates. Again, in the edge-conducting regime even-odd beating is observed.

On the experimental side of this chapter we describe in details experiments performed and obtained results. From the theoretical side (which was mainly the area of responsibility of author of this Thesis), we build a tight-binding model of the system, reproduce experimental data and demonstrate, that even-odd beating originates most probably from the conducting channel along the NS interface of the Josephson junction.

1.5.3 Chapter 4

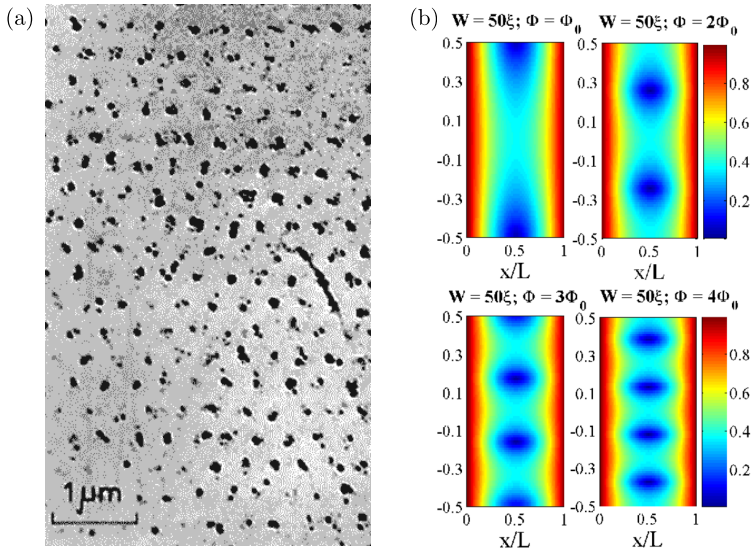

Figure 1.5. (a) Historically first observation of Abrikosov lattice from the experiment of Essman and Träuble [24]. Each black dot is a cobalt particle, bound to vortex core. Reprinted from U. Essmann and H. Träuble, "The direct observation of individual flux lines in type II superconductors", Physics Letters A **24**, 526–527 (1967), Copyright 1967, with permission from Elsevier. (b) Josephson vortex line formation in diffusive Josephson junctions, with increasing magnetic flux Φ, that penetrates normal part of the junction. Simulations by Cuevas and Bergeret [25]. Colorscale corresponds to the pair correlation function amplitude (which is effectively density of Cooper pairs), each minimum corresponds to the Josephson vortex core. Reprinted figure with permission from J. C. Cuevas and F. S. Bergeret, Phys. Rev. Lett. **99**, 217002 (2007). Copyright 2007 by the American Physical Society.

Vortices in superconductors are known already for a while and is still a subject of investigations. For example, Abrikosov [26] proposed a vortex

lattice in type-II superconductors to explain critical field scaling near the critical temperature (for type-II superconductors $H_c \propto T_c - T$, instead of $H_c \propto \sqrt{T_c - T}$ for type-I superconductors). Each Abrikosov vortex carries magnetic flux Φ_0, usually they organize into triangular lattice for magnetic field higher than first critical, or can be pinned to defects in the bulk [9]. Correct description of thermodynamical or transport properties of type-II superconductors is impossible without taking them into account.

Another superconducting setup, where one can find vortices, is a Josephson junction. Its two NS interfaces act as two reflecting surfaces in Fabry-Pérot interferometer, and interference in this setup leads to the destruction of current in several points along the 1D line in the normal part. [9]. These points are cores of so-called Josephson vortices. Contrary to Abrikosov vortices, they carry not quantized flux and generally appear in vortex-antivortex pairs. They are also responsible for the formation of Fraunhofer oscillations of critical current in magnetic field in the case of short wide Josephson junction:

$$I_c(\Phi) = I_{c0}\frac{\sin(\pi\Phi/\Phi_0)}{\Phi/\Phi_0}, \tag{1.27}$$

where $\Phi = BWL$ is a magnetic flux, penetrating to the junction area, and $\Phi_0 = h/2e$ is a superconducting flux quantum. However, cases, when then arrange to 2D structure instead of 1D chain, were unknown.

In this chapter we point out, that in the case of warped Fermi surface is is possible also to achieve two-dimensional Josephson vortex lattice. This happens, because current carriers receive preferred direction of motion, that drastically changes interference pattern inside a junction. We illustrate this finding using semiclassical description and a tight-binding model, both independently leading to the consistent picture. Also we explore, how this vortex lattice and edge effects impact $I_c(B)$ dependency of a junction and figure out, that it plays important role in high-B asymptotic behavior of critical current decay.

1.5.4 Chapter 5

Graphene offers a rich platform for wide range of applications in nanoelectronics. Conduction electrons in graphene have three distinct spin-like quantum numbers: spin itself, sublattice pseudospin and valley isospin. One of goals in graphene research is to provide handles for controlling these degrees of freedom. Another important quest is opening controllable gap

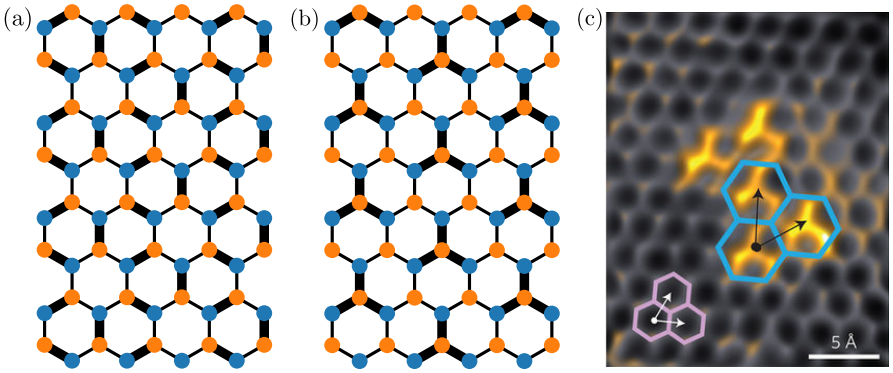

Figure 1.6. (a) Kek-O bond density modulation, that couples valleys in graphene spectrum and opens a gap [27]. (b) Kek-Y bond density modulation, that couples valleys in grapene spectrum and removes their degeneracy without opening a gap, but inducing different velocities (Chapter 5). (c) An STM image from, that demonstrates Kek-Y bond density modulation in graphene on top of copper substrate [15]. Reprinted by permission from Springer Customer Service Centre GmbH: Springer Nature, Nature Physics, C. Gutiérrez, C.-J. Kim, L. Brown, T. Schiros, D. Nordlund *et al.*, "Imaging chiral symmetry breaking from Kekulé bond order in graphene", Nature Phys. **12**, 950 (2016), Copyright 2016.

in graphene spectrum, that will turn it into a semiconductor. That was the motivation of Cristopher Gutierrez *et. al.* [15], who tried to realize proposal [28] and open a gap by special bond density modulation (see Fig. 1.6(a)). They successfully induced the superlattice, placing graphene on top of Cu-111 substrate, but the bond modulation was different from one expected (Fig. 1.6(b, c)).

In this chapter we investigate this type of graphene-based superlattice. We demonstrate, that this type of modulation removes degeneracy between two Dirac cones of graphene spectrum, leaving the spectrum non-gapped. These Dirac cones are still symmetry-protected, as well as zeroth Landau level, that stays at zero energy with a double degeneracy, while all other Landau level get split. This is remarkably different from the expectations and opens a way to control valley degree of freedom in transport experiments in graphene or its analogues in optics or acoustics.

Chapter 2

Even-odd flux quanta effect in the Fraunhofer oscillations of an edge-channel Josephson junction

2.1 Introduction

Superconductor–normal-metal–superconductor (SNS) junctions with edge channel conduction in the normal region are governed by the interplay of charge e and charge $2e$ transport: charge can only enter or exit the superconductor in units of $2e$, but in the normal region this Cooper pair can be split over opposite edges, when an electron incident on the NS interface along one edge is Andreev reflected as a hole along the opposite edge.

For quantum Hall edge channels this mechanism produces Fraunhofer oscillations (oscillations of the critical current with enclosed flux Φ) hav-

The contents of this chapter have been published and reprinted with permission from B. Baxevanis, V. P. Ostroukh, and C. W. J. Beenakker, Phys. Rev. B **91**, 041409(R) (2015).

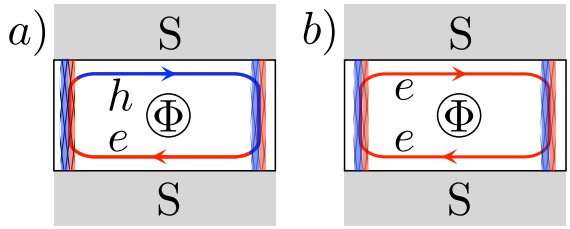

Figure 2.1. Beating mechanism for the even-odd effect in the Fraunhofer oscillations. For uncoupled edges the flux periodicity is $h/2e$, corresponding to the transfer of a charge-$2e$ Cooper pair along the left or right edge channel (blue/red hatched strips). The edge channels are coupled by a conducting path along the NS interface, allowing for a circulating loop of charge $\pm e$ with h/e flux periodicity. The circulating loop may be partly e-type (red lines) and partly h-type (blue), as in panel a, or it may be entirely of one charge-type (entirely e, as in panel b, or entirely h). Both loops contribute to the even-odd effect, but panel a dominates when the Andreev reflection probability Γ is small. (It is of order Γ, while panel b is of order Γ^2.)

ing a fundamental period of h/e, twice the usual periodicity [29]. These are chiral edge channels, so Andreev reflection along the edge of incidence is forbidden and only the circulating path of Fig. 2.1(a) contributes to the supercurrent. When the edge channels allow for propagation in both directions, the critical current includes the usual $h/2e$-periodic contributions from Andreev reflection along a single edge, and further h/e periodic contributions from circulating paths without charge transfer (Fig. 2.1(b)).

Here we investigate this beating of h/e and $h/2e$ periodic contributions to the Fraunhofer oscillations. We are motivated by recent work on proximity induced superconductivity in quantum spin-Hall (QSH) insulators[1] [19, 23, 31–34], which in one series of experiments [19] showed Fraunhofer oscillations with an even-odd effect: Large peaks in the critical current at even multiples of $h/2e$ alternate with smaller peaks at odd multiples.

The QSH insulator has helical edge channels (with direction of motion tied to the spin), so we consider that case in what follows (although the beating mechanism for the even-odd effect does not rely on helicity). Fol-

[1] G. Tkachov *et. al.* [30] calculate the flux dependence of $I_m(\Phi) = |I(\phi_0, \Phi)|$ at the fixed phase ϕ_0 that maximizes the zero-field supercurrent $I(\phi, 0)$. This partial maximization provides a lower bound to the critical current $I_c(\Phi) = \max_\phi |I(\phi, \Phi)|$, but the flux-periodicity of I_c cannot be deduced from I_m. Although authors find an even-odd effect in I_m, the critical current has no even-odd effect in their model.

lowing Ref. [23] we assume that the superconductors dope the contacted QSH insulator, locally pushing the Fermi level in the conduction band. The broad conducting pathway that appears along the NS interface will be gapped by the superconducting proximity effect, but a narrow gapless channel may remain because superconductivity only becomes effective at some penetration length ξ_0 from the NS interface. (Ref. [19] estimates $\xi_0 \gtrsim 240\,\mathrm{nm}$, comparable to the estimated width of the edge states.) This channel provides a connection between the helical edge states that is non-helical, meaning that either spin can propagate in both directions.

To describe the phase-coherent coupling of helical and non-helical edge channels we study a network model of the Josephson junction, inspired by the spectral theory of graphs [35] and as a counterpart to network models of the quantum Hall effect [36, 37]. As we will show, all information on the temperature and flux dependence of the supercurrent can be encoded in the product of a permutation matrix, representing the connectivity of the network, and a block-diagonal matrix describing the relation between incoming and outgoing modes at each node of the network.

2.2 Edge-channel Josephson junction

We consider the Josephson junction geometry of Fig. 2.2(a). A current I is passed between two superconducting electrodes at phase difference ϕ, related to the voltage V over the junction by the Josephson relation $d\phi/dt = (2e/\hbar)V$. Upon increasing the current bias, the junction switches from zero to finite DC voltage at a critical current I_c, dependent on the enclosed magnetic flux Φ. If phase fluctuations can be neglected (for a low-impedance environment), the critical current is given by

$$I_c(\Phi) = \max_\phi |I(\phi, \Phi)|. \tag{2.1}$$

We seek the oscillatory Φ-dependence of I_c (Fraunhofer oscillations) in a junction where the current flows along the edges, rather than through the bulk.

Referring to Fig. 2.2(b), the junction has width W (edges at $x = 0, W$) and length L (normal-superconductor or NS interfaces at $y = 0, L$). We choose a gauge where the superconducting pair potential Δ_0 is real. A vector potential $\boldsymbol{A} = A_y \hat{y}$ in the y-direction,

$$A_y = \frac{\Phi x}{LW} + \frac{\Phi_0 \phi}{2\pi}\delta(y - L/2), \quad \Phi_0 \equiv \frac{h}{2e}, \tag{2.2}$$

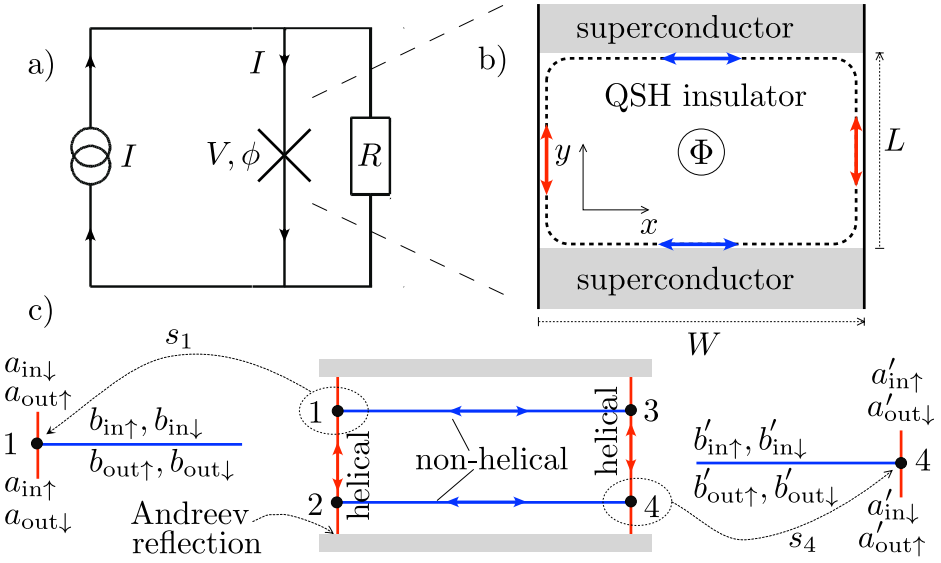

Figure 2.2. Josephson junction in a current-biased circuit (panel a), to study the dependence of the critical current I_c on the magnetic flux Φ enclosed by a circulating edge channel (panel b). The network model of the Josephson junction is illustrated in panel c. Helical modes (red, amplitudes $a_\uparrow, a_\downarrow$) and non-helical modes (blue, amplitudes $b_\uparrow, b_\downarrow$) are coupled at four nodes by a scattering matrix s_n, relating incoming and outgoing amplitudes.

then accounts for the phase difference between the NS interfaces.

2.3 Network model

To capture the essence of the problem, while still allowing for analytical solution, we represent the scattering processes by a network (Fig. 2.2(c)). At the nodes $n = 1, 2, 3, 4$ the helical edge channels along $x = 0, W$ are coupled to a single-mode non-helical channel along $y = 0, L$. Each node has a 4×4 electronic scattering matrix s_n, which relates incoming and outgoing wave amplitudes of the helical channel, $a = (a_\uparrow, a_\downarrow)$, and the non-helical channel, $b = (b_\uparrow, b_\downarrow)$, according to

$$\begin{pmatrix} a \\ b \end{pmatrix}_{\text{out}} = s_n \begin{pmatrix} a \\ b \end{pmatrix}_{\text{in}} . \tag{2.3}$$

The short-range scattering at a node can be taken as energy-independent, so the hole scattering matrix is simply the complex conjugate s_n^*. We collect these matrices in the unitary matrix $s_{\rm node} = s_1 \oplus s_1^* \oplus \cdots \oplus s_4 \oplus s_4^*$, consisting of eight 4×4 blocks arranged along the diagonal.

Since the effect of the magnetic field is only felt on long length scales, we can assume that s_n preserves time-reversal symmetry. The requirement

$$s_n = \begin{pmatrix} \sigma_y & 0 \\ 0 & \sigma_y \end{pmatrix} s_n^{\rm T} \begin{pmatrix} \sigma_y & 0 \\ 0 & \sigma_y \end{pmatrix}, \tag{2.4}$$

together with unitarity, $s_n^\dagger s_n = 1$, imposes the form [38]

$$s_n = \begin{pmatrix} e^{2i\psi_n}\sigma_0\sqrt{\Gamma_n} & e^{i\psi_n + i\psi_n'} U_n \sqrt{1-\Gamma_n} \\ e^{i\psi_n + i\psi_n'} U_n^\dagger \sqrt{1-\Gamma_n} & -e^{2i\psi_n'}\sigma_0\sqrt{\Gamma_n} \end{pmatrix}. \tag{2.5}$$

Helical and non-helical channels are coupled with probability $1-\Gamma_n$, while $U_n \in {\rm SU}(2)$ describes the spin-mixing associated with that coupling. (Eq. 2.4 is satisfied because $\sigma_y U_n^{\rm T} \sigma_y = U_n^\dagger$ for any SU(2) matrix $U(n)$.) Time-reversal symmetry forbids spin mixing within the helical or non-helical channel, which is why the upper-left and lower-right blocks of s_n are proportional to the 2×2 unit matrix σ_0.

The nodes are connected by a unitary bond matrix $s_{\rm bond}$, which is the product of a diagonal matrix of phase factors and a permutation matrix. We decompose $s_{\rm bond} = s_{\rm left} \oplus s_{\rm right} \oplus s_{\rm bottom} \oplus s_{\rm top}$ in terms of matrices $s_{\rm left}$ and $s_{\rm right}$ that connect the a-amplitudes (along $x = 0$ and $x = W$, with phase factor $e^{i\varepsilon L/\hbar v} \exp[i\tau_z (e/\hbar) \int A_y \, dy]$) and matrices $s_{\rm bottom}$ and $s_{\rm top}$ that connect the b-amplitudes (along $y = 0$ and $y = L$, with phase factor $e^{i\varepsilon W/\hbar v}$). Andreev reflection is included in $s_{\rm left}$ and $s_{\rm right}$ via matrix elements that connect a node to itself, switching electron-hole and spin-band with phase factor

$$s_{\rm A} = i\alpha\tau_y \otimes \sigma_y, \quad \alpha(\varepsilon) = i\varepsilon/\Delta_0 + \sqrt{1 - \varepsilon^2/\Delta_0^2}. \tag{2.6}$$

(The Pauli matrices τ_i and σ_i act, respectively, on the electron-hole e, h and spin $\uparrow, \downarrow$ degrees of freedom.)

Knowledge of $s_{\rm node}$ and $s_{\rm bond}$ determines the entire spectrum of the network [35]. A bound state at energy $|\varepsilon| < \Delta_0$ corresponds to a unit eigenvalue of $M(\varepsilon) = s_{\rm node} s_{\rm bond}(\varepsilon)$, leading to the determinantal equation ${\rm Det}\,[1 - M(\varepsilon)] = 0$. The density of states of the continuous spectrum at

$|\varepsilon| > \Delta_0$ is given by

$$\rho(\varepsilon) = -\frac{1}{\pi}\frac{d}{d\varepsilon}\,\mathrm{Im}\,\ln\,\mathrm{Det}[1 - M(\varepsilon + i0^+)] + \text{constant}, \tag{2.7}$$

where the "constant" refers to ϕ-independent terms (see Sec. 2.8 for defivation). The Josephson current at temperature T then follows from [39, 40]:

$$I(\phi, \Phi) = -kT\frac{2e}{\hbar}\frac{d}{d\phi}\sum_{p=0}^{\infty}\ln\mathrm{Det}\,[1 - M(i\omega_p)], \tag{2.8}$$

as a sum over fermionic Matsubara frequencies $\omega_p = (2p+1)\pi kT$. This expression assumes that the system equilibrates without restrictions on the fermion parity, so it holds on time scales long compared to the quasiparticle poisoning time (otherwise there would appear an additional sum over bosonic Matsubara frequencies) [22].

2.4 Uncoupled edges

When $kT \gg \hbar v/W$ there is no phase-coherent coupling between the edges at $x = 0$ and $x = W$. We may then set s_{top} and s_{bottom} to zero in the evaluation of the determinant in Eq. 2.8, with the result

$$I(\phi, \Phi) = I_{\mathrm{edge}}(\phi) + I_{\mathrm{edge}}(\phi + 2\pi\Phi/\Phi_0), \tag{2.9}$$

$$I_{\mathrm{edge}}(\phi) = kT\frac{4e}{\hbar}\sin\phi\sum_{p=0}^{\infty}[2\cos\phi + \zeta(\omega_p) + 1/\zeta(\omega_p)]^{-1},$$

$$\zeta(\omega) = \Gamma^2 e^{-2\omega L/\hbar v}\left[\sqrt{1 + \omega^2/\Delta_0^2} - \omega/\Delta_0\right]^2. \tag{2.10}$$

(To simplify the formulas we have taken identical $\Gamma_n \equiv \Gamma$.)

For $\Gamma \to 1$ we recover the short-junction-to-long-junction crossover formula of Ref. [22], which in the short-junction limit $L \ll \hbar v/\Delta_0$ and for low temperatures $kT \ll \Delta_0$ results in a critical current

$$I_c(\Phi) = \frac{e\Delta_0}{2\hbar}(1 + |\cos(\pi\Phi/\Phi_0)|) \tag{2.11}$$

with minima that are offset from zero, in agreement with Ref. [23]. For $\Gamma \ll 1$, still in the short-junction and low-temperature limit, we find

instead

$$I(\phi,\Phi) = I_0 \sin(\phi + \pi\Phi/\Phi_0)\cos(\pi\Phi/\Phi_0) \tag{2.12}$$

$$\Rightarrow I_c(\Phi) = I_0|\cos(\pi\Phi/\Phi_0)|, \quad I_0 = \frac{8e\Delta_0}{3\pi\hbar}\Gamma^2. \tag{2.13}$$

For these uncoupled edges the critical current is $h/2e$ periodic in Φ.

2.5 Coupled edges

The effect on the supercurrent of a phase-coherent coupling of the edges can be studied perturbatively in powers of $e^{-\pi kTW/\hbar v}$, by expanding the logarithmic determinant in Eq. 2.8 with the help of the formula

$$\ln \mathrm{Det}\,(1 - M_0 - \delta M) = \ln \mathrm{Det}\,(1 - M_0) - \sum_{n=1}^{\infty} \frac{1}{n} \mathrm{Tr}\left[(1 - M_0)^{-1}\delta M\right]^n. \tag{2.14}$$

The lowest order contribution with h/e periodicity in Φ is given by

$$\delta I_{h/e} = kT\frac{2e}{\hbar}\frac{d}{d\phi}\,\mathrm{Tr}\, s_{\mathrm{node}}(1 - s_{\mathrm{left}}s_{\mathrm{node}})^{-1}s_{\mathrm{top}}s_{\mathrm{node}} \cdot (1 - s_{\mathrm{right}}s_{\mathrm{node}})^{-1}s_{\mathrm{bottom}}\big|_{\varepsilon=i\omega_0} + \{s_{\mathrm{left}} \leftrightarrow s_{\mathrm{right}}\}, \tag{2.15}$$

describing a quasiparticle that encircles the junction clockwise or anticlockwise.

The effect of this contribution is largest for small Andreev reflection probability $\Gamma_n \ll 1$. To first order in Γ, and in the low-temperature, short-junction limit, we find

$$\delta I_{h/e} = (8e/\hbar)kTe^{-2\pi kTW/\hbar v}\sin(\phi + \pi\Phi/\Phi_0) \times (\sqrt{\Gamma_1\Gamma_2} + \sqrt{\Gamma_1\Gamma_4} + \sqrt{\Gamma_3\Gamma_4} + \sqrt{\Gamma_3\Gamma_2}) \times \sin(\gamma_2 - \gamma_4)\sin(\gamma_1 - \gamma_3). \tag{2.16}$$

(To simplify a lengthy general expression we made a definite choice $U_n = e^{i\gamma_n\sigma_x}$, $\psi_n = \psi'_n = 0$ for the spin-mixing matrices.) Without spin mixing, for $\gamma_n = 0$, the contribution 2.16 of order Γ vanishes, but there is a nonzero contribution of order Γ^2,

$$\delta I_{h/e} = (8e/\hbar)kTe^{-2\pi kTW/\hbar v}\left[(\sin(\phi - \pi\Phi/\Phi_0)\Gamma_1\Gamma_2 + \sin(\phi + 3\pi\Phi/\Phi_0)\Gamma_3\Gamma_4)\right]. \tag{2.17}$$

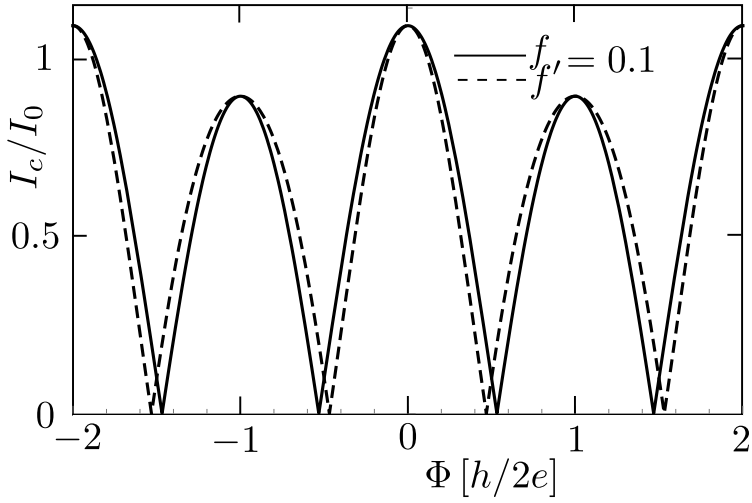

Figure 2.3. Even-odd effect in the Fraunhofer oscillations of the critical current due to the beating of h/e and $h/2e$ oscillations. The curves are calculated with spin mixing from Eq. 2.18 (solid lines, dominated by the path of Fig. 2.1(a)) and without spin mixing from Eq. 2.19 (dashed lines, dominated by the path of Fig. 2.1(b)).

The contributions 2.16 and 2.17 correspond to the pathways show in Figs. 2.1(a) and 2.1(b), respectively.

Addition of $\delta I_{h/e}$ to the zeroth order supercurrent 2.12 (for identical $\Gamma_n \equiv \Gamma$) gives the critical current

$$I_c(\Phi) = I_0 |\cos(\pi\Phi/\Phi_0) + f|, \tag{2.18a}$$

$$f = \frac{12\pi kT}{\Delta_0 \Gamma} e^{-2\pi kTW/\hbar v} \sin(\gamma_2 - \gamma_4) \sin(\gamma_1 - \gamma_3), \tag{2.18b}$$

with spin mixing at the nodes, and

$$I_c(\Phi) = I_0 |\cos(\pi\Phi/\Phi_0) + f' \cos(2\pi\Phi/\Phi_0)|, \tag{2.19a}$$

$$f' = (6\pi kT/\Delta_0) e^{-2\pi kTW/\hbar v}, \tag{2.19b}$$

without spin mixing. Both types of Fraunhofer oscillations are h/e periodic, with an even-odd effect of relative magnitude f or f', see Fig. 2.3.

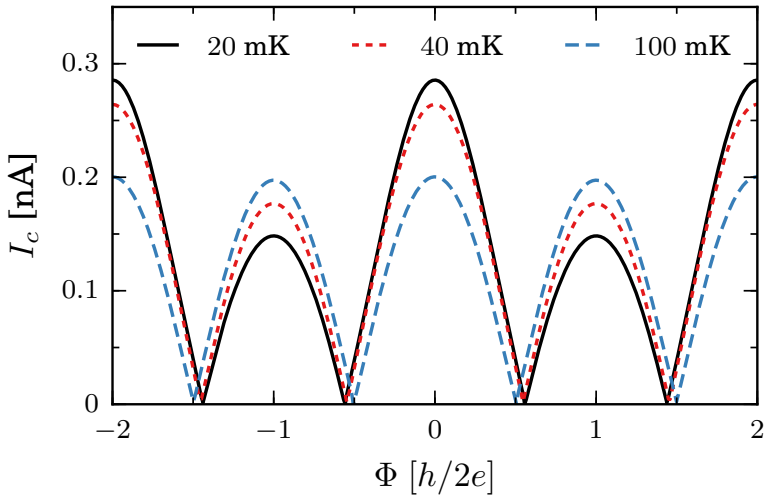

Figure 2.4. Fraunhofer oscillations for the experimentally relevant parameters given in the text, calculated from Eq. 2.8 for three different temperatures.

2.6 Comparison with experiment

Turning now to the experiment that motivated this analysis [19], we first of all notice that the observed even-odd effect appears already for the first few peaks around zero field. An explanation in terms of a Lorentz-force induced asymmetry in the current distribution is therefore unlikely[2]. The h/e-periodic Josephson effect of Majorana zero-modes [45] is spoiled, on the time scale of the experiment, by any small amount of quasiparticle poisoning [23], so an explanation along these lines is not viable. A conducting pathway through the bulk, parallel to the edges, can explain the data [19] — but only if it is located within 10% of the device center (the flux Φ needs to be accurately partitioned into twice $\Phi/2$). The mechanism proposed here does not require any such fine tuning.

The InAs/GaSb quantum well with Ti/Al electrodes of Ref. [19] has superconducting gap $\Delta_0 = 0.125\,\mathrm{meV}$ and edge state velocity[46] $v = 4.6 \cdot 10^4\,\mathrm{m/s}$. We take the same v for the non-helical channel. There is some uncertainty in the effective dimensions of the junction, we set

[2] In a device with aspect ratio W/L the Lorentz force produces an even-odd effect in the Fraunhofer oscillations for flux $\Phi \gtrsim (W/L)h/e$, as calculated in Refs. [41, 42] and measured in Refs. [43, 44].

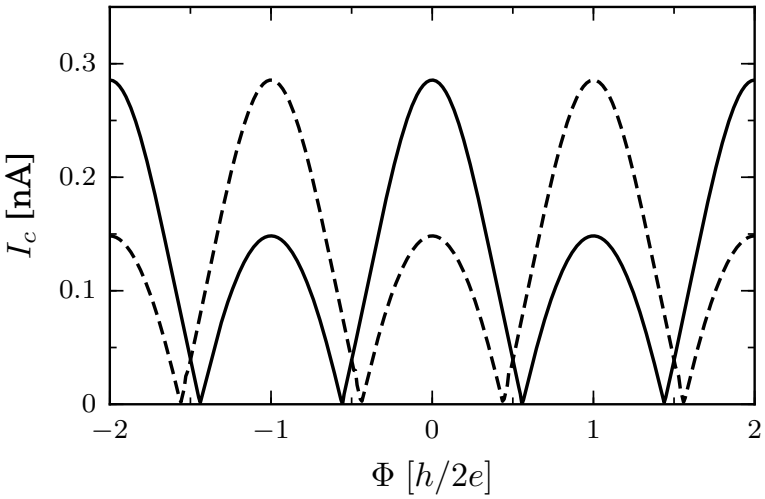

Figure 2.5. The solid curve is the $T = 20\,\mathrm{mK}$ critical current of Fig. 2.4, without phase shifts at the scattering nodes, while the dashed curve shows the inverted even-odd effect for $\psi_1' + \psi_3' = \pi$ (and all other phase shifts kept at zero).

$L = 0.5\,\mu\mathrm{m}$, $W = 3.5\,\mu\mathrm{m}$. We then have comparable L and $\xi_0 = \hbar v/\Delta_0$, so we calculate the supercurrent directly from Eq. 2.8 — without taking the short-junction limit. The observed critical current in the 0.25 nA range implies an Andreev reflection probability $\Gamma \approx 0.2$, which is the value we take for Γ_n at all four scattering nodes.

The degree of spin mixing upon propagation along the nonhelical channel is quantified by setting $U_1 U_3^\dagger = U_2 U_4^\dagger = e^{i\gamma\sigma_x}$. The value of γ is unknown, we take a moderately strong spin mixing with $\gamma = \pi/6$, but note that the even-odd effect exists also without any spin mixing (see Fig. 2.3). The critical current shown in Fig. 2.4 exhibits an even-odd effect of a similar magnitude as observed experimentally [19]. The temperature dependence is somewhat stronger: In the experiment traces of the even-odd effect are still visible at 100 mK, but not in our calculation.

The beating mechanism has one qualitative feature that can help to distinguish it from other explanations of the even-odd effect: The sign of the effect — whether the $\Phi = 0$ peak is larger or smaller than the $\Phi = h/2e$ peak — depends on microscopic details. This is evident from Eq. 2.18, in that the offset f can be of either sign. A similar inversion of the even-odd effect can be induced by varying the phase shifts in the node

scattering matrix 2.5, as we show in Fig. 2.5. Observation of an even-odd effect with the smallest peak at even multiples of $h/2e$ would constitute strong support for the beating mechanism, but no such inversion has been found so far [19].

In our analysis we have assumed helical edge state transport, appropriate for a quantum spin-Hall insulator, but the beating mechanism itself would apply also to nonhelical edge conduction. As was also pointed out in the experimental paper [19], the Fraunhofer oscillations are a sensitive probe of the current distribution, but cannot distinguish between a topologically trivial or nontrivial Josephson junction. That would require observation of a quantized conductance or supercurrent.

2.7 Conclusion

We have analyzed the effect of inter-edge coupling on the Fraunhofer oscillations in a quantum spin-Hall Josephson junction. A network model allows for an efficient description of the beating of $h/2e$ periodic intra-edge and h/e periodic inter-edge contributions to the critical current. The even-odd effect has comparable magnitude to what is observed in a recent experiment [19], see Fig. 2.4, but the sample-dependent inversion of Fig. 2.5 has not been observed.

We note that the beating mechanism studied here in the two-dimensional geometry of a quantum spin-Hall insulator may apply more generally when a pair of conducting pathways enclosing different flux interferes. Indeed, a recent work studies a similar beating effect in a one-dimensional wire geometry [47], to explain multi-periodic Fraunhofer oscillations observed in Bi nanowires [48].

2.8 Appendix

We describe in more detail the network model of a Josephson junction that we have introduced and applied in the main text, and in particular give a selfcontained derivation of the formula (2.7) for the supercurrent through the network.

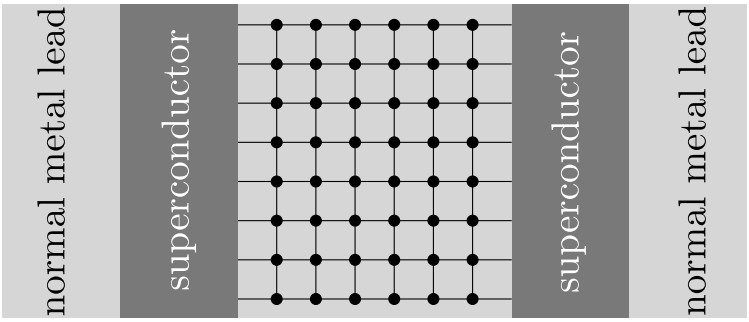

Figure 2.6. Network model of a Josephson junction. The normal metal leads are attached to the superconductor as an intermediate step in the derivation of the scattering matrix formula for the supercurrent. The final expression (2.31) contains only the scattering matrices of the nodes and bonds in the junction region. Andreev reflection at the interface with the superconductor is included in the bond matrix, via Eq. (2.20).

2.8.1 Construction of node and bond scattering matrices

The scattering theory of a Josephson junction developed in Ref. [39] expresses the supercurrent in terms of the two scattering matrices s_{N} of the normal region (N) and s_{A} of Andreev reflection at the normal-superconductor (NS) interfaces. While the matrix s_{A} has a simple expression, see Eq. (2.6), calculation of s_{N} can be quite complicated.

In this work we have used an alternative network representation, where the supercurrent is expressed in terms of the scattering matrices s_{node} and s_{bond} of the nodes and bonds of a network (see Fig. 2.6). These matrices are the direct sum of scattering matrices of individual nodes and bonds, so they have a simple structure that can be written down without any calculation.

The node matrix s_{node} is block-diagonal with the scattering matrices s_n of node $n = 1, 2, \ldots$ on the diagonal. Because electrons and hole are uncoupled in the normal region, each matrix s_n is itself block-diagonal with an electron block $s_{n,e}(\varepsilon)$ and a hole block $s_{n,h}(\varepsilon) = s^*_{n,e}(-\varepsilon)$. We thus have $s_{\mathrm{node}} = s_{1e} \oplus s_{1h} \oplus s_{2e} \oplus s_{2h} \oplus \cdots$.

The bond matrix $s_{\mathrm{bond}} = UP$ is the product of a diagonal matrix U of phase factors and a permutation matrix P that maps the indices of outgoing modes to incoming modes. The mode indices are spin $s \in \{\uparrow, \downarrow\} \equiv \{+1, -1\}$, particle-hole $t \in \{e, h\} \equiv \{+1, -1\}$, and possibly also an orbital degree of freedom $\nu \in \{1, 2, \ldots\}$. (In the system considered in

the main text all bonds support only a single orbital mode.) The matrix element $\langle n\nu' s't'|s_{\rm bond}|m\nu st\rangle$ is zero unless a mode with spin s of particle-hole type t that is outgoing from node m in orbital mode ν is incoming onto node n in orbital mode ν' as a spin-s' type-t' particle. There are no "dangling bonds", meaning that $s_{\rm bond}$ has a single non-zero element in each row and column.

Andreev reflection at the NS interface is included in $s_{\rm bond}$ via the matrix elements

$$\begin{aligned}\langle n\nu' s't'|s_{\rm bond}|m\nu st\rangle &= -i\alpha\, st\, \delta_{mn}\delta_{\nu\nu'}\delta_{s',-s}\delta_{t',-t},\\ \alpha(\varepsilon) &= ie^{-i\arccos(\varepsilon/\Delta_0)} = i\varepsilon/\Delta_0 + \sqrt{1-\varepsilon^2/\Delta_0^2}.\end{aligned} \tag{2.20}$$

Please note that this definition of α differs by a factor i with that used in Ref. [39]; we prefer it this way because now $\alpha(\varepsilon) = \alpha^*(-\varepsilon)$, so it is particle-hole symmetric. The branch of the square root of $1-\varepsilon^2/\Delta_0^2$ is fixed by $\mathrm{Re}\,\alpha(\varepsilon + i0^+) > 0$, so that for $|\varepsilon| > \Delta_0$ one has $\alpha = i\varepsilon/\Delta_0 - i(\mathrm{sign}\,\varepsilon)\sqrt{\varepsilon^2/\Delta_0^2 - 1}$.

For $|\varepsilon| < \Delta_0$ one has $|\alpha| = 1$, hence Eq. (2.20) describes Andreev reflection with unit probability. This is a matter of convenience, because a nonzero probability of normal reflection at the NS interface can be accounted for by inserting a node just before the interface. (See Ref. [49] for an alternative scattering formulation that does not separate normal and Andreev reflection.)

The simplification afforded by the network representation in the construction of the scattering matrices comes at a price: the matrix $s_{\rm node}s_{\rm bond}$ is sparse, but its dimension is much larger than the dimension of $s_{\rm N}s_{\rm A}$. We have not studied this systematically, but we expect both representations in terms of $s_{\rm node}s_{\rm bond}$ and $s_{\rm N}s_{\rm A}$ to have the same computational complexity, scaling $\propto N^3$ with the number of nodes.

2.8.2 Density of states in terms of node and bond matrices

To calculate the density of states of the Josephson junction it is convenient to attach normal metal leads to the superconductors (see Fig. 2.6). The leads support the propagating modes that form basis states for the scattering matrix $S_{\rm SNS}(\varepsilon)$ of the junction. (Without the normal leads we would only have propagating modes above the gap, for $|\varepsilon| > \Delta_0$.)

The density of states $\rho(\varepsilon)$ is determined by the unitary scattering

matrix $S_{\rm SNS}$ via the general expression[50]

$$\rho(\varepsilon) = \frac{1}{2\pi}\frac{d}{d\varepsilon}\,\mathrm{Im}\,\ln\,\mathrm{Det}\,S_{\rm SNS}(\varepsilon + i0^+). \tag{2.21}$$

In Ref. [39] the determinant of $S_{\rm SNS}$ was related to the determinant of $1 - s_{\rm N}s_{\rm A}$. Here we seek to derive a similar expression in terms of the node and bond matrices of the network.

For $|\varepsilon| < \Delta_0$ the bond matrix $s_{\rm bond}(\varepsilon)$ is unitary, but for $|\varepsilon| > \Delta_0$ the Andreev reflection probability $|\alpha|^2$ drops below unity because of propagating modes in the superconductor. Unitarity can be restored by embedding $s_{\rm bond}$ in larger matrix

$$S_{\rm bond} = \begin{pmatrix} s_{\rm bond} & t_{\rm NS} \\ t'_{\rm NS} & r_{\rm NS} \end{pmatrix}, \tag{2.22}$$

containing also the transmission and reflection matrices of the NS interfaces: a mode incident from the normal lead onto the NS interface is reflected with amplitude $r_{\rm NS}$ and is transmitted through the interface with amplitude $t_{\rm NS}$, while $t'_{\rm NS}$ describes the transmission in the opposite direction (into the normal lead). At subgap energies $t_{\rm NS} = t'_{\rm NS} = 0$, while $r_{\rm NS}$ as well as $s_{\rm bond}$ are unitary. Above the gap only the full matrix $S_{\rm bond}$ is unitary.

In order to rewrite Eq. (2.21) in terms of $s_{\rm node}$ and $s_{\rm bond}$ we start from the relation

$$\begin{aligned} S_{\rm SNS} &= r_{\rm NS} + \sum_{n=0}^{\infty} t'_{\rm NS} s_{\rm node} (s_{\rm bond} s_{\rm node})^n t_{\rm NS} \\ &= r_{\rm NS} + t'_{\rm NS} s_{\rm node} (1 - s_{\rm bond} s_{\rm node})^{-1} t_{\rm NS} \\ &= r_{\rm NS} - t'_{\rm NS} (s_{\rm bond} - s^{\dagger}_{\rm node})^{-1} t_{\rm NS}. \end{aligned} \tag{2.23}$$

This relation expresses the fact that modes incident on the SNS junction are either reflected directly at the NS interface, with amplitude $r_{\rm NS}$, or first transmitted through the interface (amplitude $t_{\rm NS}$), followed by multiple scattering in the network (amplitude $s_{\rm node} + s_{\rm node}s_{\rm bond}s_{\rm node} + \cdots$), and finally transmission back through the NS interface (amplitude $t'_{\rm NS}$). In the final equality in Eq. (2.23) we have used that $s_{\rm node}$ (unlike $s_{\rm bond}$) is unitary for all energies.

We now invoke the folding identity,

$$\mathrm{Det}\begin{pmatrix} A & B \\ C & D \end{pmatrix} = (\mathrm{Det}\,A)\,\mathrm{Det}\,(D - CA^{-1}B), \tag{2.24}$$

valid for any invertible submatrix A, to equate

$$\begin{aligned}
&\operatorname{Det}\left(s_{\mathrm{bond}} - s_{\mathrm{node}}^{\dagger}\right) \operatorname{Det} S_{\mathrm{SNS}} \\
&\quad = \operatorname{Det} \begin{pmatrix} s_{\mathrm{bond}} - s_{\mathrm{node}}^{\dagger} & t_{\mathrm{NS}} \\ t'_{\mathrm{NS}} & r_{\mathrm{NS}} \end{pmatrix} \\
&\quad = \operatorname{Det} \left[S_{\mathrm{bond}} - \begin{pmatrix} s_{\mathrm{node}}^{\dagger} & 0 \\ 0 & 0 \end{pmatrix} \right] \\
&\quad = \operatorname{Det} S_{\mathrm{bond}} \operatorname{Det} \left[1 - \begin{pmatrix} s_{\mathrm{node}}^{\dagger} & 0 \\ 0 & 0 \end{pmatrix} S_{\mathrm{bond}}^{\dagger} \right] \\
&\quad = \operatorname{Det} S_{\mathrm{bond}} \operatorname{Det}\left(1 - s_{\mathrm{node}}^{\dagger} s_{\mathrm{bond}}^{\dagger}\right)
\end{aligned} \tag{2.25}$$

$$\begin{aligned}
\Rightarrow \operatorname{Det} S_{\mathrm{SNS}} &= \operatorname{Det} S_{\mathrm{bond}} \operatorname{Det} s_{\mathrm{node}} \frac{\operatorname{Det}\left(1 - s_{\mathrm{node}}^{\dagger} s_{\mathrm{bond}}^{\dagger}\right)}{\operatorname{Det}\left(1 - s_{\mathrm{node}} s_{\mathrm{bond}}\right)} \\
&= \frac{\left(\operatorname{Det} S_{\mathrm{bond}} \operatorname{Det} s_{\mathrm{node}}\right)^{1/2} \operatorname{Det}\left(1 - s_{\mathrm{node}}^{\dagger} s_{\mathrm{bond}}^{\dagger}\right)}{\left(\operatorname{Det} S_{\mathrm{bond}}^{\dagger} \operatorname{Det} s_{\mathrm{node}}^{\dagger}\right)^{1/2} \operatorname{Det}\left(1 - s_{\mathrm{node}} s_{\mathrm{bond}}\right)}.
\end{aligned} \tag{2.26}$$

In the final equality we have used that both S_{bond} and s_{node} are unitary.

The folding identity also tells us that

$$\operatorname{Det} S_{\mathrm{bond}} = \operatorname{Det} s_{\mathrm{bond}} \operatorname{Det} s_{\mathrm{lead}}, \tag{2.27}$$

$$s_{\mathrm{lead}} = r_{\mathrm{NS}} - t'_{\mathrm{NS}} s_{\mathrm{bond}}^{-1} t_{\mathrm{NS}}, \tag{2.28}$$

where s_{lead} describes the reflection of a mode incident from the normal metal lead when all bonds of the network are cut at the first node from the NS interface. We can therefore identify

$$\rho_{\mathrm{lead}}(\varepsilon) = \frac{1}{2\pi} \frac{d}{d\varepsilon} \operatorname{Im} \ln \operatorname{Det} s_{\mathrm{lead}}(\varepsilon + i0^{+}) \tag{2.29}$$

with the density of states of the SNS junction without the normal region.

Combination of Eq. (2.21) with Eqs. (2.26) and (2.28) gives the required scattering formula for the density of states of the Josephson junction,

$$\rho(\varepsilon) = \operatorname{Im} \frac{d}{d\varepsilon} \nu(\varepsilon + i0^{+}) + \rho_{\mathrm{lead}}(\varepsilon), \tag{2.30a}$$

$$\begin{aligned}
\nu(\varepsilon) = &-\pi^{-1} \ln \operatorname{Det}\left(1 - s_{\mathrm{node}} s_{\mathrm{bond}}\right) \\
&+ \tfrac{1}{2}\pi^{-1} \ln \operatorname{Det}\left(s_{\mathrm{node}} s_{\mathrm{bond}}\right).
\end{aligned} \tag{2.30b}$$

This is Eq. (2.7) from the main text, where the ϕ-independent terms $\rho_{\rm lead}$ and $\ln\mathrm{Det}\, s_{\rm node}s_{\rm bond}$ are simply referred to as "constant". The formula describes both the discrete and the continuous spectrum: for $|\varepsilon| < \Delta_0$ it gives a sum of delta functions at the bound state energies, superimposed on the smooth $\rho_{\rm lead}$, while for $|\varepsilon| > \Delta_0$ these peaks are broadened because the bound states can leak out into the superconductor.

2.8.3 Supercurrent in terms of node and bond matrices

In the absence of fermion parity conservation (the case treated in the main text) we need to only retain the ϕ-independent term $\propto \ln\mathrm{Det}\,(1 - s_{\rm node}s_{\rm bond})$ in the density of states (2.30). As derived in Ref. [40], the supercurrent at temperature T is then a sum of the logarithmic determinant over fermionic Matsubara frequencies $\omega_p = (2p+1)\pi kT$,

$$\begin{aligned} I_0 &= -kT\frac{2e}{\hbar}\frac{d}{d\phi}\sum_{p=0}^{\infty}\ln\mathrm{Det}\,[1 - s_{\rm node}(i\omega_p)s_{\rm bond}(i\omega_p)] \\ &= kT\frac{2e}{\hbar}\sum_{p=0}^{\infty}\mathrm{Tr}\left\{[1 - s_{\rm node}s_{\rm bond}]^{-1}s_{\rm node}\frac{ds_{\rm bond}}{d\phi}\right\}_{\varepsilon=i\omega_p}. \end{aligned} \tag{2.31}$$

At zero temperature the sum may be approximated by an integral, $kT\sum_p \mapsto \int_0^\infty d\omega/2\pi$. The factor of $2e$ refers to the Cooper pair charge. Ref. [40] has an additional factor of two because of spin degeneracy, which here we do not assume.

The derivation of Eq. (2.31) in Ref. [40] was for $\mathrm{Det}\,(1 - s_{\rm N}s_{\rm A})$, but it holds equally well for $\mathrm{Det}\,(1 - s_{\rm node}s_{\rm bond})$ because it only relies on two properties of ν that are universally valid: particle-hole symmetry, $\nu(\varepsilon) = \nu^*(-\varepsilon)$, and causality — $\nu(\varepsilon)$ being an analytic function for $\mathrm{Im}\,\varepsilon > 0$.

When fermion parity is conserved the terms $\rho_{\rm lead}$ and $\ln\mathrm{Det}\,(1 - s_{\rm node}s_{\rm bond})$ in Eq. (2.30) must be retained even though they are not ϕ-dependent, because they are needed to determine whether a set of occupation numbers has the right fermion parity. It is for this reason that we were careful to properly account for these ϕ-independent terms in the calculation of the density of states. The expression for the supercurrent in the fermion-parity conserving case contains also a sum over bosonic

Matsubara frequencies $\Omega_p = 2p\pi kT$,

$$I_\pm = I_0 - kT\frac{2e}{\hbar}\frac{d}{d\phi}\ln\tfrac{1}{2}\left[1 \pm e^{J_{\rm lead}}\sqrt{\mathrm{Det}\,X(0)}\right.$$
$$\left.\times\,\exp\left(\sum_{p=1}^{\infty}(-1)^p \ln\mathrm{Det}\,X(i\Omega_p/2)\right)\right], \tag{2.32}$$

$$X = (1 - s_{\rm node}s_{\rm bond})(s_{\rm node}s_{\rm bond})^{-1/2}, \tag{2.33}$$

$$J_{\rm lead} = \int_0^\infty d\varepsilon\,\rho_{\rm lead}(\varepsilon)\ln\tanh(\varepsilon/2kT). \tag{2.34}$$

The $\pm$ sign in Eq. (2.32) indicates even or odd fermion parity of the superconducting ground state. The sign is $+$ at $\phi = 0$, and then switches each time a pair of bound states crosses the Fermi level ($\varepsilon = 0$).

One limitation of the network representation is that we do not have a formula for the ground-state fermion parity in terms of $s_{\rm node}$ and $s_{\rm bond}$. The derivation in Ref. [22] of such a formula in terms of $s_{\rm N}$ and $s_{\rm A}$ does not carry over.

Chapter 3

h/e superconducting quantum interference through trivial edge states in InAs

3.1 Introduction

Topological systems are a hot topic in condensed matter physics [51]. This is largely motivated by the existence of states at the interface between two topologically distinct phases, for example helical edge states in a quantum spin Hall insulator (QSHI) [52, 53]. Inducing superconductivity in these edge states would form a topological superconductor [51]. Superconducting edge transport has already been found in materials that are predicted to be QSHI [19, 32]. However, edge states can also have a non-topological origin. Trivial edge conduction is found in InAs alongside the chiral edge states in the QH regime [54] and recently in the proposed QSHI InAs/GaSb as well [55, 56]. To be able to discriminate between topological and trivial states it is crucial to study transport through triv-

The contents of this chapter have been published and reprinted with permission from F. K. de Vries, T. Timmerman, V. P. Ostroukh, J. van Veen *et. al.*, Phys. Rev. Lett. **120**, 047702 (2018).

ial edges also and clarify differences and similarities between them. In this work we study the superconducting transport through trivial edge states in non-topological InAs Josephson junctions using superconducting quantum interference (SQI) measurements. We find supercurrent carried by these edge states and an intriguing h/e periodic signal in a superconducting quantum interference device (SQUID) geometry.

3.2 Description of the experiment

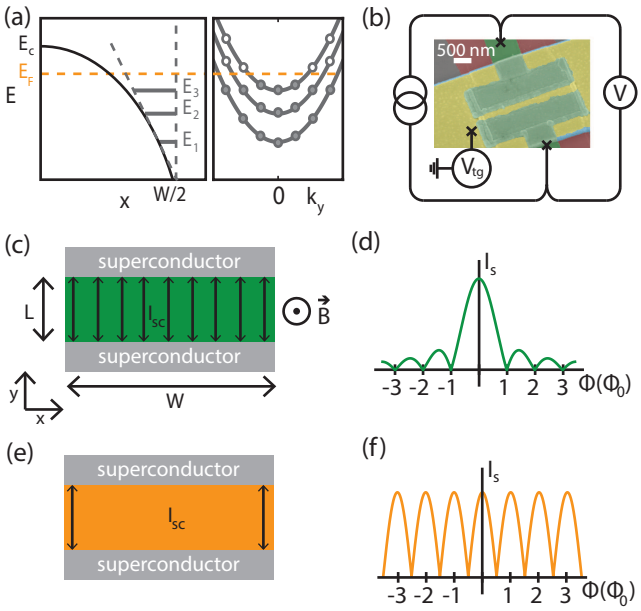

Figure 3.1. (a) Sketch of the conduction band minimum around the edge of a 2DEG with Fermi level pinning at $W/2$. The band bending leads to a roughly triangular quantum well in the vicinity of the edge, therefore one-dimensional sub bands form of which three are drawn, as an example. The orange dashed line indicates the Fermi level corresponding to the current distribution in (e). (b) False coloured SEM image of the device with dimensions $W = 4$ µm and $L = 500$ nm, where the quasi-four terminal measurement setup is added. Red is the mesa, green the NbTiN contacts, blue SiN_x dielectric and yellow the gold top gate. (c) Schematic representation of a Josephson junction of width W and length L. A homogeneously distributed supercurrent I_{sc} is running through the whole junction, resulting in (d) a Fraunhofer SQI pattern. (e) If supercurrent only flows along the edges of the sample, (f) a SQUID pattern is observed.

Trivial edge states arise when the Fermi level resides in the band gap in the bulk, while being pinned in the conduction band at the surface. Then, band bending leads to electron accumulation at that surface as schematically drawn in Fig. 1(a). The Fermi level pinning can have several origins: truncating the Bloch functions in space [57, 58], a work function difference [59], the built-in electric field in a heterostack [60] and the surface termination [61]. In our 2D InAs Josephson junctions the accumulation surface is located at the edge of the mesa that is defined by wet etching. The quantum well is MBE grown on a GaSb substrate serving as a global bottom gate. The superconducting electrodes are made of sputtered NbTiN with a spacing of 500 nm and a width of 4 µm. A SiN_x dielectric separates the top gate from the heterostructure. Electrical quasi-four terminal measurements [see Fig.1(b)] are performed in a dilution refrigerator with an electron temperature of 60 mK unless stated otherwise.

The electron density in the InAs quantum well is altered by using the electrostatic gates, V_{tg} and V_{bg}, located above and below the 2DEG. Decreasing the density subsequently increases the normal state resistance R_n and reduces the switching current I_s as shown in Fig. 2(a). The Josephson junction is first characterized at $V_{tg} = 0$ V and V_{bg} = -1.65 V, where the largest switching current is observed. From the IV trace in Fig. 2(a) we estimate an induced superconducting gap of 0.4 meV and, using the corrected OBTK model [62], a transmission of $T = 0.73$. The junction is quasi-ballistic because the mean free path of 2.8 µm (extracted from a Hall bar device on the same wafer) is larger than its length L of 500 nm. The large superconducting gap and high transmission value indicate a high quality InAs Josephson junction.

3.3 Superconducting quantum interference measurements

SQI measurements have successfully been used before to gather information on the supercurrent density profile in Josephson junctions [19, 32, 63]. This is typically done, using Dynes-Fulton approach [11], which connects critical current dependency on magnetic field $I_c(B)$ and zero-field supercurrent density profile $j(x)$ with a Fourier transform. It was originally developed for tunnel junctions, but can also be applied to transparent junctions under several assumptions. Firstly, we should have a sinusoidal current-phase dependency, which is in accordance with the transmission

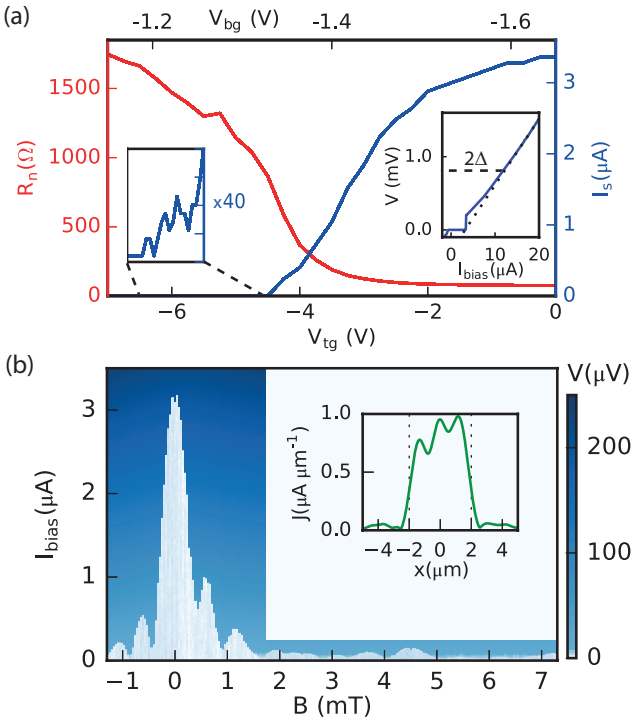

Figure 3.2. (a) Normal state resistance R_n and switching current I_s at the respective top gate V_{tg} and bottom gate V_{bg} voltages. The left inset depicts a seperate measurement at the indicated gate voltages, where a smaller current bias step size is used for higher resolution. The right inset shows an IV trace at $V_{tg} = 0$ V and $V_{bg} =$ -1.65 V , where two dashed lines are added for extraction of the induced superconducting gap Δ and the excess current. (b) The measured voltage as function of the applied current I_{bias} and perpendicular magnetic field B at $V_{tg} = 0$ V and $V_{bg} =$ -1.65 V. The inset depicts the calculated supercurrent density along the width of the device that is indicated by the dotted lines.

value and temperature in our experiment [64]. Secondly, the Andreev levels, that carry supercurrent in the junction, may only weakly deviate from the longitudinal propagation. Our junction satisfies this constraint since the superconducting coherence length $\zeta = \hbar v_F/\Delta \approx 1.3$ µm $> L$ [34]. If both assumptions hold, we expect Fraunhofer SQI pattern in the case of homogeneous current distribution (Fig. 1(c-d)) and SQUID pattern in the case of current flowing along the edges (Fig. 1(e-f)).

A SQI measurement at the largest switching current reveals a Fraun-

hofer like pattern as shown in Fig. 2(b). The central lobe is twice as wide as the side lobes and the amplitude decreases as expected. The slight asymmetry in the amplitudes we contribute to breaking of the mirror symmetry of the sample in the direction along the current [65]. The effective length of the junction [$\lambda = \delta B_{lobe}/(\Phi_0 \cdot W)$] of 1.2 µm is extracted from the periodicity of the SQI pattern. Flux focusing due to the Meissner effect causes it to be larger than the junction length ($\lambda > L$) [66]. The extracted current density profile, plotted in Fig. 2(b), is close to uniform. The supercurrent is thus dominated by bulk transport as expected at these gate voltages.

The interference pattern in Fig. 2(b) deviates from the expected pattern after the second lobe. Recently a similar distorted Fraunhofer tail was observed and discussed in graphene [67]. The perpendicular magnetic field exerts a Lorentz force on the electron and holes suppressing the formation of Andreev bound states. The suppression becomes relevant at a magnetic field scale of Δ/eLv_F, equal to 1 mT in our case, roughly agreeing with the observation. The analysis only holds for the bulk of the junction, since the scattering at the edges reduces the difference in the electron and hole motion in a magnetic field.

Next we study the SQI pattern as the Fermi level is decreased by tuning the top gate to more negative values. The upper two (green) traces in Fig. 3(a) have a wide central lobe, identifying a Fraunhofer pattern. The effective length is λ =1.7 µm, different from before, which we believe is due to different vortex pinning because of the larger magnetic field range of the measurement. In the third (first blue) trace we observe that the first nodes turn into peaks, which is highlighted by the dashed lines. This is the transition from a Fraunhofer to a SQUID pattern. Curiously the amplitude and width of the peaks are alternating in the blue traces in Fig. 3(a). The even-odd pattern is composed of an h/e and $h/2e$ periodic signal. An even-odd pattern was observed before in Pribiag *et al.* [19]. In comparison, in this work the amplitude difference in the lobes is much larger and the pattern is visible over a large gate range. The calculated supercurrent density profiles in Fig. 3(b) have a central peak that is physically unlikely considering the device geometry. The cause of this intriging interference pattern will be discussed in more detail later. Reducing V_{tg} further we find a clear $h/2e$ periodic SQUID interference pattern in the bottom two (orange) traces. This is a strong indication of edge conduction in our device. Confirmed by the edge transport only in the extracted supercurrent den-

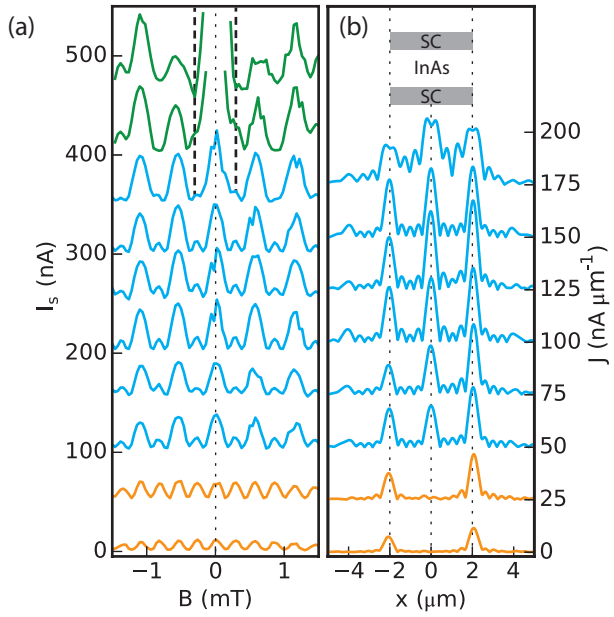

Figure 3.3. (a) The switching current plotted as function of perpendicular magnetic field and (b) the corresponding current density along the width of the device (see inset), assuming the validity of the Dynes-Fulton approach. The gate values used are from bottom to top: V_{tg} -5.4 V to -3.6 V (0.2 V step) and V_{bg} -1.270 V to -1.396 V (0.014 V step). The green, blue and orange traces are Fraunhofer, even-odd and SQUID patterns, respectively. Since the current is only swept up to 100 nA, the green traces are not suitable for extracting a supercurrent density profile. The traces are offset by 50 nA in (a) and 25 nA/μm in (b).

sity profiles in Fig. 3(b). The transition from bulk to edge transport as a function of gate voltage is measured in several other Josephson junctions. Since we observe supercurrent through the trivial edge states of an InAs quantum well, we conclude that a clear demonstration of superconducting edges alone does not prove induced superconductivity in topological edge states.

3.4 Even-odd SQI pattern

We now return to the remarkable h/e SQUID signal to investigate its origin. Figure 4(a) shows a more detailed measurement in this gate regime,

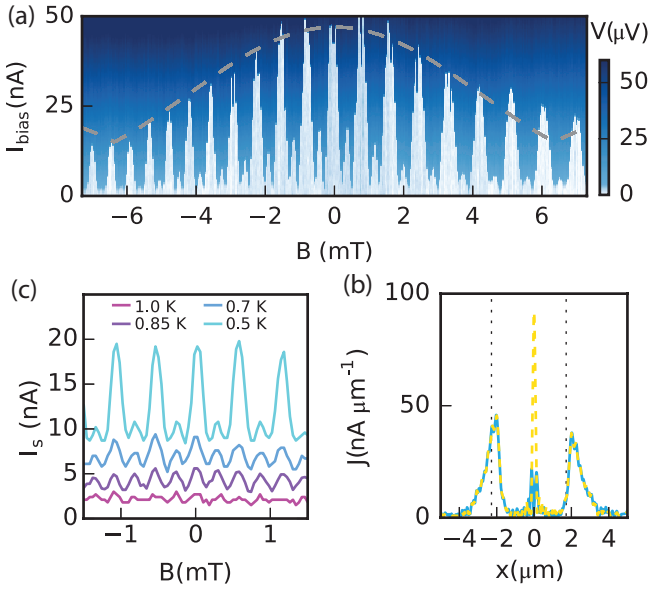

Figure 3.4. (a) Measured voltage as a function of I_{bias} and magnetic field B at V_{tg} = -5 V and V_{bg} = -1.29 V. (b) Switching current versus the magnetic field for different temperatures at the same gate voltages as (a). The traces are offset by 5 nA for clarity. (c) Current density profile, calculated from the SQI pattern of (a). The blue trace uses equation (1), thus correcting the vertical offset in the SQI pattern. The yellow dashed trace is extracted without this correction.

the even-odd pattern is observed over more than 25 oscillations. The envelope of the peaks is attributed to the finite width of the edge channels. The effect is suppressed by raising the temperature [see Fig. 4(b)], for $T >$ 850 mK a regular $h/2e$ SQUID pattern remains. The origin can not lie in effects that occur beyond a certain critical magnetic field, like $0 - \pi$ transitions [68], edge effects [43, 69] and a topological state, because we observe the even-odd pattern around zero magnetic field as well. An effect that does not rely on magnetic field and is strongly temperature dependent is crossed Andreev reflection [70].

The lowest order crossed Andreev reflection (up to electron-hole symmetry) is schematically depicted in Fig. 5(a). An electron travels along one edge, whereafter a hole is retroreflected over the other edge. This process alone is independent of the flux through the junction, but still adds to the critical current (see Sec. 2.5). Higher order processes that include an electron that encircles the junction completely pick up an h/e

phase when a flux quantum threads through the junction, hence the supercurrent becomes h/e periodic [71]. Additionaly, interference processes between crossed Andreev and single edge Andreev states could lead to a h/e contribution [72]. It is important to note that the critical current is h/e periodic in flux trough the sample, but still 2π periodic in superconducting phase difference.

Forming crossed Andreev states in the junction is only possible if the particles can flow along the contacts. Electrostatic simulations indeed show a large electron density close to the contacts at gate voltages where the bulk is already depleted, because of local screening of the top gate. Nevertheless the needed coherence length for a crossed Andreev reflection is on the order of 10 µm, where the estimated superconducting coherence length (from bulk values) is 1.3 µm. The difference between these values remains an open question.

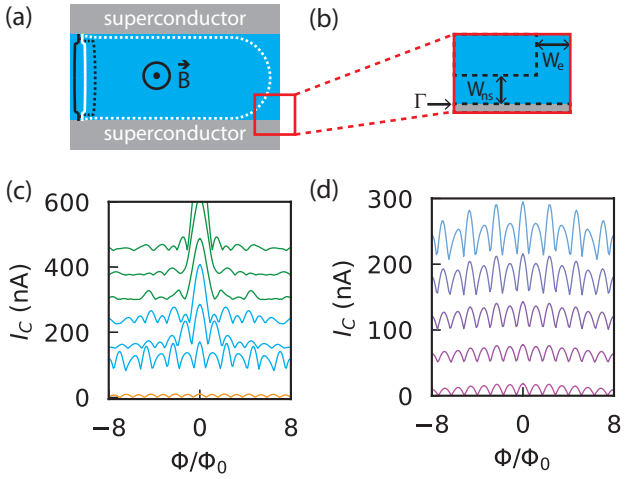

Figure 3.5. (a) Schematic representation of two crossed Andreev processes. The black and white lines indicate electron and hole trajectories or vice versa. The solid lines represent a single edge Andreev state and the dotted lines a crossed Andreev state. (b) Detailed sketch of one corner of junction in our tight binding mode indicating the widths W_{ns} and W_e, and tunnel barrier Γ. (c) Calculated SQI patterns at overall chemical potential ranging from -0.06 eV to 0.18 eV (0.04 eV step) at 0.46 K and (d) at temperatures 0.4 K, 0.9 K, 1.4 K, 1.9 K, 2.3 K at a chemical potential of -0.2 eV. Traces are offset by 10 nA for clarity. In (c) the color represents the type of interference pattern, green for Fraunhofer, blue for even-odd and orange for SQUID, respectively.

3.5 Phenomenological model: crossed Andreev reflection impact

The phenomenological model proposed in Chapter 2 considers both single edge and crossed Andreev states. In our device we expect the lowest order crossed Andreev states to contribute most because of the short coherence length. Combining their flux insensitive contribution to the critical current and the usual $h/2e$ periodic contribution from single edge Andreev bound states, the model predicts an even-odd or h/e SQUID pattern:

$$I_c(\Phi) = I_0 \left|\cos(\pi\Phi/\Phi_0) + f\right|. \tag{3.1}$$

Where I_0 the critical field at zero magnetic field and Φ is the applied flux. Constant f can be arbitrarily large, it dependes on the ratio Γ between the probability to Andreev reflect on a node versus the probability to scatter to another edge and is exponentially suppressed by the width of the sample:

$$f \sim \Gamma^{-1} \frac{k_B T}{\Delta} e^{-2\pi(k_B T/\Delta)(W/\zeta)}. \tag{3.2}$$

The predicted pattern is thus the absolute value of a vertically offsetted cosine function. That is exactly the pattern we measured in Fig. 3(a) and 4(a) as both the amplitude and width of the lobes alternate From the data we estimate $f = 0.3$ and, using the other known parameters, find $\Gamma \sim 10^{-1}$. Taking the Fourier transform in the Dynes-Fulton analysis, offset f leads to a non-physical current density around zero, like we observe in the current density profiles in Fig. 3(b) and the yellow dashed line in Fig. 4(c). Moreover, the Dynes-Fulton approach is not valid here since crossed Andreev reflection does not meet the second assumption of having straight trajectories only. We can compensate the crossed Andreev contribution by subtracting the constant offset of $f \cdot I_0$=11 nA. This results in a current distribution with mainly current along the edges, as plotted in the blue trace of Fig. 4(c). We did not take into account that I_0 is actually not constant due to the Fraunhofer envelope of the SQI pattern, so the current density in the center of the junction is not entirely eliminated.

3.6 Tight-binding simulations

Even though the SQI pattern from the phenomenological model is in qualitative agreement with our data, we also present a tight binding model of

system in order to connect it directly to experimentally accessible parameters. In the microscopic model we include the superconducting gap as measured, the width of the paths along the contacts W_{ns} of 20 nm [extracted from the Fraunhofer envelope in Fig. 4(a)], and Fermi level pinning on the edges leading to edge current in the region W_e. It is crucial to also take into account a tunnel barrier Γ at the contacts that has a magnitude consistent with the measured transmission value. This barrier enhances normal reflection and therefore elongates the length electrons and holes travel before Andreev reflecting. Incorporating these experimental values we find an h/e SQUID pattern. Emulating the experimental gating effect by changing the overall chemical potential results in a crossover from even-odd to Fraunhofer [Fig. 5(c)], consistent with the measurement in Fig. 3. As a check, W_{ns} is reduced in steps to zero, which results in a SQUID pattern. Additionally, in Fig. 5(d) we observe that increasing the temperature indeed smears out the even-odd pattern and leaves us with a regular SQUID pattern, similar to the experimental data in Fig. 4(b). Summarizing, both the phenomenological model and the microscopic model support our hypothesis of the h/e SQUID originating from crossed Andreev states.

3.7 Conclusion

We have experimentally shown that trivial edge states can support highly coherent superconducting transport that also becomes visible in an h/e periodic SQI pattern. Both effects have been considered as possible signatures for inducing superconductivity in topological edge states before [19, 32]. Therefore we conclude that superconducting edge transport and an h/e SQUID pattern only, cannot distinguish between topological and trivial edge states, nor can it be considered a definite proof for a topological phase.

3.8 Appendix

3.8.1 Tight binding model

We have taken the following Hamiltonian for tight binding simulations:

$$H = \left(\frac{\hbar^2(k_x^2 + k_y^2)}{2m_{\text{eff}}} - \mu(x,y) \right) \tau_z + \alpha(k_x\sigma_y - k_y\sigma_x)\tau_z + g\mu_{\text{B}}B(x)\sigma_z + \Delta(x)\tau_x, \tag{3.3}$$

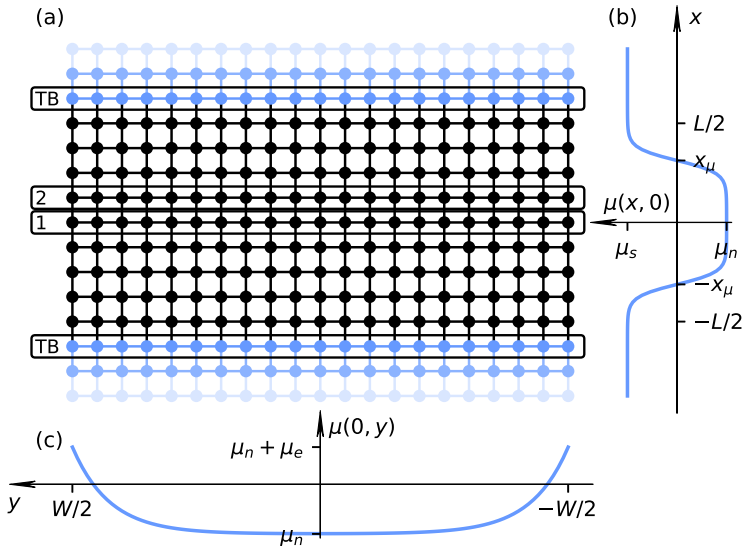

Figure 3.6. (a) Schematical representation of a tight-binding model. Bogolyubov-de Gennes Hamiltonian is discretized on a square lattice. Superconducting sites of the system have a blue color, normal – black. A tunnel barrier is created, using one row of sites with decreased chemical potential (marked TB on the scheme). The current was calculated from Green's function of sites, marked 1 and 2 on the scheme (see the detailed explanation below). (b) Chemical potential profile for $x = 0$. Offset between location of chemical potential step and superconducting region together with the tunnel barrier leads to formation of scattering channel between edges. (c) Chemical potential profile for $y = 0$. Band bending is represented with an increased chemical potential at the edges, leading to edge conductivity in a doped regime.

where σ Pauli matrices correspond to the spin degree of freedom, and τ – to the electron and hole one. It is discretized on a square lattice with lattice constant $a = 2$ nm. The normal part of a SNS junction is represented as a rectangle $-L/2 \leq x \leq L/2$ and $-W/2 \leq y \leq W/2$, the superconducting parts – as translationally invariant in x direction stripes with $-W/2 \leq y \leq W/2$. Proximity-induced pairing potential $\Delta(x)$ is zero in a normal part and constant in a superconducting part of the system, with a step-like transition. The magnetic field is assumed to be fully

screened by the superconductors. Its impact is included as Zeeman term and via Peierls substitution.

At first realistic values of $\alpha = 5 \cdot 10^{-12}\,\mathrm{eV} \cdot \mathrm{m}$ and $g = 11.5$ for the Rashba and Zeeman term were used to verify that they do not play an important role in this parameter regime. After we were sure that Zeeman and Rashba terms can be neglected, we have put $\alpha = 0$ and $g = 0$ for the sake of numerical performance. This allowed to decouple spins and decrease the dimensionality of the Hamiltonian twice, since both decoupled subblocks contribute equally to the current.

Chemical potential $\mu(x, y)$ is selected to capture primary features of the device: band bending near the edges and screening near the NS boundaries top gate. It has the following form:

$$\mu(x,y) = \frac{\mu_{\mathrm{norm}} + \delta\mu_{\mathrm{edge}}(y)}{2}\left(\tanh\frac{x+x_\mu}{\lambda_\mu} - \tanh\frac{x-x_\mu}{\lambda_\mu}\right) + \frac{\mu_{\mathrm{sc}}}{2}\left(2 - \tanh\frac{x+x_\mu}{\lambda_\mu} + \tanh\frac{x-x_\mu}{\lambda_\mu}\right), \tag{3.4}$$

where

$$\delta\mu_{\mathrm{edge}}(y) = 2\mu_{\mathrm{e}} e^{-W/2\lambda_e}\cosh\frac{y}{\lambda_e} \tag{3.5}$$

is the term, that introduces band bending near the edges of a normal part. μ_{norm} and μ_{sc} are chemical potentials in gated area (primarily normal part) and area screened by the superconducting contacts. If normal part is governed to the insulating state with negative μ_{norm}, the offset between $L/2$ and x_μ leads to formation of a conducting channel on the NS boundaries of the junction, with a width:

$$W_{\mathrm{ns}} = L/2 - x_\mu. \tag{3.6}$$

The tunnel barrier on the NS interface was represented as a single row of sites with a chemical potential reduced by $\Delta\mu_{\mathrm{TB}}$.

The finite-temperature critical current of the SNS junction was calculated by maximizing the current-phase dependency, similarly to the approach, used in [73]. The Green's function was numerically calculated for several Matsubara frequencies on two neighbouring rows of the sites in the normal part of the junction, then the current was obtained by the summation:

$$I = \frac{2ek_BT}{\hbar}\sum_{n=0}^{N_{\max}}\left(\Im\,\mathrm{tr}\,H_{21}G_{12}(i\omega_n) - \Im\,\mathrm{tr}\,H_{12}G_{21}(i\omega_n)\right). \tag{3.7}$$

Here H_{21} and G_{21} denote hopping matrix and Green's function subblock from cells of row 1 to row 2, indicated on Fig. 3.6 (all the hoppings, that form a cut through the system), and vice versa. $\omega_n = (2n+1)\pi k_B T$ is the n-th Matsubara frequency. Value $N_{\max}$ was obtained dynamically, based on the estimated convergence rate. The Green's functions were calculated, using package Kwant [16].

The numerical values of parameters, used for simulations, are presented in Table 3.1. A lattice constant of $a = 2$ nm was selected small enough to capture characteristic length scales of an edge and NS boundary current channels.

W [nm]	L [nm]	λ_e [nm]	λ_μ [nm]	x_μ [nm]
400	200	28	1	$0 \div 50$

m_{eff}/m_e	Δ [eV]	μ_{sc} [eV]	$\delta\mu_e$ [eV]
0.04	$4 \cdot 10^{-4}$	0.2	0.15

Table 3.1. Numerical parameters, used for tight-binding simulations.

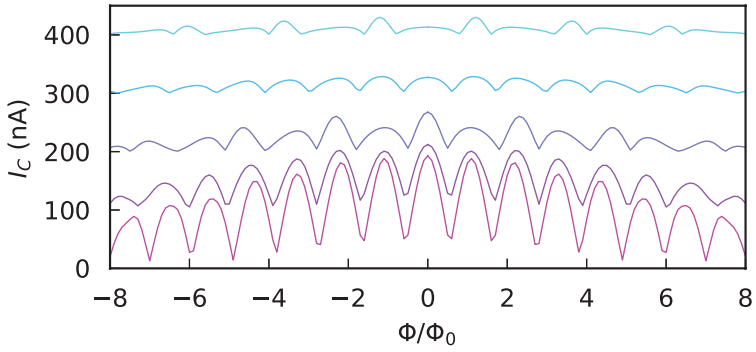

Figure 3.7. Tight binding calculation of the superconducting quantum interference as a function of tunnel barrier strength at the contact. Increasing the tunnel barrier height leads to enhanced normal reflection with respect to Andreev reflection. The electrons or holes then have a higher chance of traversing along the contact before Andreev reflecting. Forming a crossed Andreev states requires the charge carriers to traverse around the junction fully. Therefore enhanced normal reflection is benefecial for forming these states and the resulting even-odd SQI pattern. Here we plot the SQI patterns for a tunnel barrier strength ranging from 0.6 eV to 1.40 eV (bottom to top) in 0.2 eV steps.

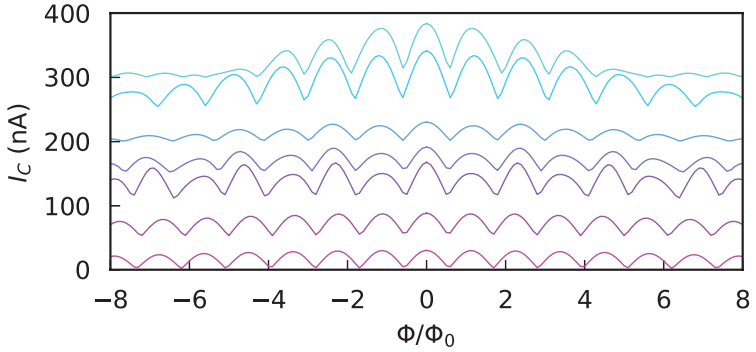

Figure 3.8. Tight binding calculation of the superconducting quantum interference as a function of width of the channel along the edge. As a sanity check: if the width is 2 nm (bottom trace), we do not see even-odd effect. Increasing the width (in 8 nm steps up to 50 nm), increases the number of channels along the contact and the coherence length, up to the point that the 1D channel become 2D and the even-odd effect reduces again.

Chapter 4

Two-dimensional Josephson vortex lattice and anomalously slow decay of the Fraunhofer oscillations in a ballistic SNS junction with a warped Fermi surface

4.1 Introduction

A junction between two superconductors responds to an imposed magnetic flux Φ by producing a chain of circulating current vortices, known as Josephson vortices [9]. The critical current $I_c(\Phi)$ oscillates with period $\Phi_0 = h/2e$ and amplitude $\propto \Phi_0/\Phi$. These socalled Fraunhofer oscillations are a macroscopic quantum interference effect, first observed in 1963 in a tunnel junction [74]. The effect is now used as a sensitive probe of ballistic transport and edge currents in graphene and topological insulators [19, 32,

The contents of this chapter have been published and reprinted with permission from V. P. Ostroukh, B. Baxevanis, A. R. Akhmerov, and C. W. J. Beenakker, Phys. Rev. B **94**, 094514 (2016).

63, 67, 75, 76].

Since the self-field of the current vortices is typically too weak to screen the imposed magnetic field B from the junction area, the arrangement of Josephson vortices is governed by quantum interference — unaffected by the classical electrostatics that governs the two-dimensional (2D) Abrikosov vortex lattice in the bulk superconductor [9]. The fundamental question addressed here, is whether quantum interference by itself is capable of producing a 2D vortex lattice in a Josephson junction. It is known that the linear arrangement of the vortices along the superconducting interface is modified by insulating boundaries [41–43, 77], in a junction of lateral width W comparable to the separation L of the interfaces. But in wide junctions ($W \gg L$), when boundary effects are irrelevant, only linear arrangements of Josephson vortices are known [25, 78–81].

We have discovered that a 2D Josephson vortex lattice appears when the circular Fermi surface acquires a square or hexagonal distortion. Such a warped Fermi surface has flattened facets that produce a nonisotropic velocity distribution of the conduction electrons, peaked at velocity directions normal to the facets. Analytical and numerical calculations of the supercurrent distribution in the high-field regime (magnetic length $l_m = \sqrt{\hbar/eB}$ less than L) reveal the appearance of multiple rows of vortex-antivortex pairs, forming a 2D bipartite rectangular lattice in the normal region with lattice constant

$$a_{\text{vortex}} = \frac{W\Phi_0}{\Phi} = \frac{\pi l_m^2}{L}. \tag{4.1}$$

As shown in Fig. 4.1 (resulting from a numerical simulation discussed in Sec. 4.7), in the weak-field regime $l_m \gtrsim L$ there is only a single row of W/a_{vortex} vortex-antivortex pairs. However, when l_m drops well below L multiple rows of vortex-antivortex pairs appear. The appearance of this 2D vortex lattice is associated with a crossover from a $1/B$ to a $1/\sqrt{B}$ decay of the amplitude of the Fraunhofer oscillations. In contrast, for a circular Fermi surface the amplitude crosses over to an accelerated $1/B^2$ decay when $l_m < L$ [69].

The outline of this chapter is as follows. In Secs. 4.2 and 4.3 we formulate the problem of magnetic interference in a ballistic Josephson junction and present the semiclassical analytical solution for the current distribution. The resulting vortex lattice is described in Sec. 4.4, far from the lateral boundaries. As shown in Sec. 4.5, within a magnetic length l_m from the boundaries there is a lattice reconstruction that produces

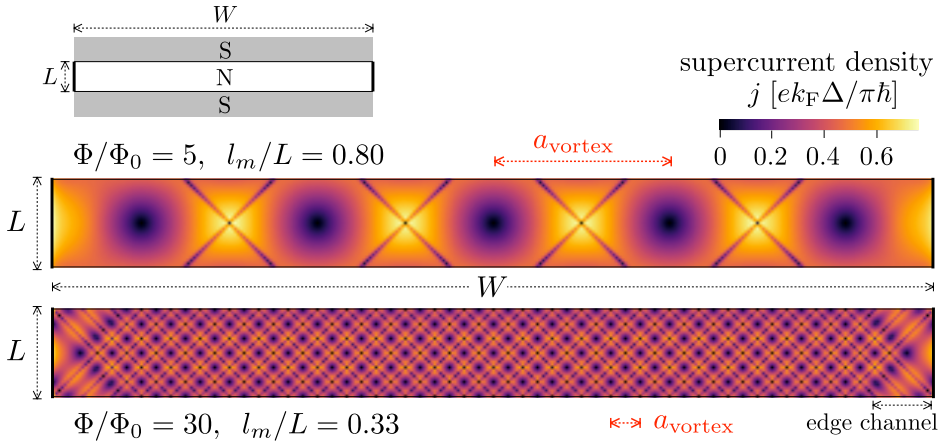

Figure 4.1. Supercurrent density in an SNS (superconductor–normal-metal–superconductor) Josephson junction, resulting from the numerical simulation of Sec. 4.7 on a square lattice with a half-filled band and a square Fermi surface (lattice constant a_0, normal region of size $W = 10L = 300\,a_0$, band width $2E_0$, Fermi velocity $v_F \equiv E_0 a_0/\sqrt{2}\hbar$, resulting in $N = 282$ transverse modes per spin direction at the Fermi level, superconducting gap $\Delta = 2.5 \cdot 10^{-3}\,E_0 \Rightarrow \xi \equiv \hbar v_F/\Delta = 283\,a_0$, zero phase difference). The two panels are for a weak and strong perpendicular magnetic field, both at a low temperature $k_B T/\Delta = 10^{-2}$ in the short-junction regime $L/\xi = 0.1$. The cyclotron radius $l_{\rm cycl}$ remains large compared to L also for the strongest fields considered, $l_{\rm cycl}/L = (W/a_0)(\Phi_0/\Phi) \gtrsim 10$. A bipartite square lattice of vortex-antivortex pairs in the normal region (lattice constant $a_{\rm vortex} = \pi l_m^2/L$) forms in the lower panel. Notice the edge reconstruction of the vortex lattice, producing an edge channel of width $\simeq l_m$ large compared to $a_{\rm vortex}$. This edge channel results purely from magnetic interference, it is unrelated to the skipping orbits along the edge that would form in higher fields (when $l_{\rm cycl} < L$).

an edge channel purely as a result of quantum interference, at magnetic fields that are still so weak that the curvature of the trajectories due to the Lorentz force can be neglected. Because of the edge channel the amplitude of the Fraunhofer oscillations decays as $l_m/W \propto B^{-1/2}$ rather than as $l_m^2/LW \propto B^{-1}$, see Sec. 4.6. In Sec. 4.7 we test the semiclassics with a fully quantum mechanical solution of a tight-binding model. This numerical simulation also allows us to assess the sensitivity of the results against the effects of disorder and nonideal NS interfaces. We conclude in Sec. 4.8.

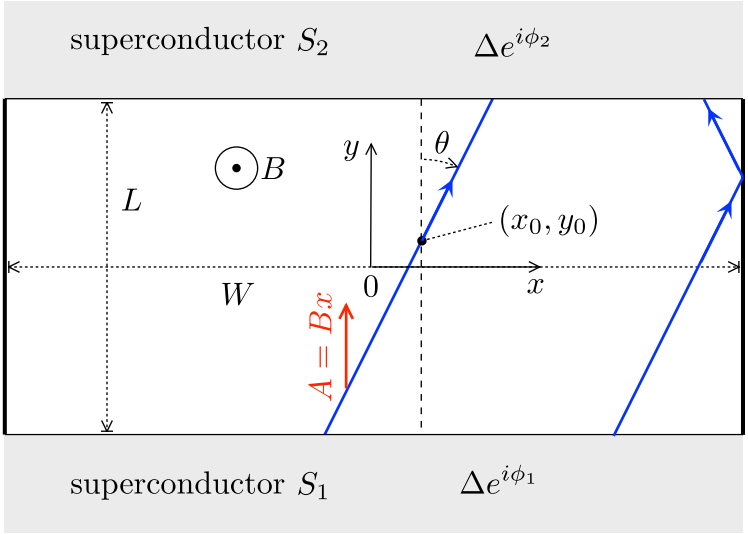

Figure 4.2. Josephson junction formed by a normal metal (width W, length L) connecting two superconductors at a phase difference $\phi = \phi_1 - \phi_2$. A perpendicular magnetic field B is applied to the normal region. Electron trajectories used in the semiclassical calculation of the supercurrent density are indicated.

4.2 Description of the problem

We consider a two-dimensional (2D) normal metal (N) layer in the x–y plane, covered by two superconducting electrodes (S_1 and S_2) a distance L apart (see Fig. 4.2). The proximity effect induces an excitation gap Δ in the S-region $|x| < W/2$, $|y| > L/2$, producing a discrete excitation spectrum in the N-region $|x| < W/2$, $|y| < L/2$.

We work in the short-junction regime $L \ll \xi$, with $\xi = \hbar v_{\rm F}/\Delta$ the superconducting coherence length induced by the proximity effect. (The short-junction regime is chosen for simplicity, we do not expect our qualitative findings to change when L becomes longer than ξ.) The lateral width W of the junction is $\gg L$, it may be comparable to ξ. The gap Δ_0 in the bulk superconductors is assumed to be much larger than Δ, with a bulk coherence length ξ_0 much smaller than ξ.

A perpendicular magnetic field B (magnetic length $l_m = \sqrt{\hbar/eB}$) produces oscillations in the critical current of the Josephson junction (Fraunhofer oscillations), periodic with period $\Phi_0 = h/2e$ in the enclosed flux $\Phi = BWL$. We assume that the magnetic field is screened from the S-

region by a short screening length in the bulk superconductors, even in the high-field regime $l_m \lesssim L$.

In the analytical calculation we take the semiclassical limit $k_F L \gg 1$, in which bound states in the junction can be associated with classical trajectories. The junction is ballistic (no impurity scattering), so the trajectories are arcs of cyclotron radius $l_{\rm cycl} = \hbar k_F/eB$. We assume that $k_F L$ is sufficiently large that the ratio $l_{\rm cycl}/L = k_F L \times (l_m/L)^2$ remains $\gg 1$ for the largest fields considered, so we neglect the curvature of the trajectories in the analytical calculation (but not in the numerics). In particular, skipping orbits along the edge play no role in our analysis.

The single-electron dispersion relation $E_{\boldsymbol{k}}$ has a nonisotropic dependence on the 2D wave vector $\boldsymbol{k} = (k_x, k_y)$, resulting in a nonisotropic distribution of the velocity $\boldsymbol{v}_{\boldsymbol{k}} = \hbar^{-1}\partial E_{\boldsymbol{k}}/\partial \boldsymbol{k}$ over the Fermi surface. Our analysis is general, but for a specific example we consider the warping of the Fermi surface on a square lattice (unit lattice constant), with dispersion relation

$$\begin{aligned} E_{\boldsymbol{k}} &= E_0 - \tfrac{1}{2}E_0(\cos k_x + \cos k_y). \\ \Rightarrow v_{\boldsymbol{k}} &= \frac{E_0}{2\hbar}(\sin k_x, \sin k_y). \end{aligned} \tag{4.2}$$

The Fermi surface is deformed from a circle to a square as we raise the Fermi energy from the bottom of the band to the band center. For later use we record the relation at the Fermi energy $E_F \in (0, E_0)$ between k_x and the angle of incidence θ on the NS interface:

$$\begin{aligned} \tan\theta = \frac{v_x}{v_y} &= \frac{\sin k_x}{\sqrt{1-(\cos k_x + 2E_F/E_0 - 2)^2}}, \\ -k_F < k_x < k_F, &\quad k_F = \arccos(1 - 2E_F/E_0). \end{aligned} \tag{4.3}$$

4.3 Semiclassical calculation of the supercurrent

In semiclassical (WKB) approximation [82] a bound state at energy $|\varepsilon| < \Delta$ corresponds to a periodic classical trajectory that traverses the junction, accumulating a phase shift that is a multiple of 2π. We distinguish two types of periodic trajectories, one in which an *electron* propagates from superconductor S_1 to S_2, is Andreev reflected as a hole and retraces its path to S_1, and another in which a *hole* propagates from S_1 to S_2 and retraces its path as an electron. The first path is indicated by $\sigma_{\rm eh} = +1$, the second path by $\sigma_{\rm eh} = -1$.

For a given periodic trajectory the total phase shift is given by

$$\begin{aligned} \phi_{\text{total}} &= -2\arccos(\varepsilon/\Delta) + \sigma_{\text{eh}}(\phi-\gamma), \\ \gamma &= \frac{2e}{\hbar}\int_{S_1}^{S_2} \boldsymbol{A}\cdot d\boldsymbol{l}. \end{aligned} \tag{4.4}$$

The ε-dependent term, which has the same sign for $\sigma_{\text{eh}} = \pm 1$, is the phase shift accumulated over a penetration depth in the superconductor (in the Andreev approximation [83] $\Delta \ll E_{\text{F}}$). The σ_{eh}-dependent terms consist of the contribution from the pair potential in S_1, S_2 (phase difference $\phi = \phi_1 - \phi_2$) and the phase shift γ accumulated in the N-region from the vector potential $\boldsymbol{A} = (0, Bx, 0)$.

In the short-junction regime $L \ll \xi$ we may neglect the phase shift in N arising from the energy difference 2ε of electron and hole[1]. For $0 < \phi - \gamma < \pi$ the (spin degenerate) bound state corresponding to this periodic trajectory is at energy $\sigma_{\text{eh}}\varepsilon$ with

$$\varepsilon = \Delta\cos(\phi/2 - \gamma/2). \tag{4.5}$$

A tube of width of the order of the Fermi wave length, extending along the trajectory that passes through the point (x_0, y_0) at an angle θ with the y-axis, can be thought of as a single-mode wave guide connecting the two superconductors. In thermal equilibrium at temperature T the single-mode supercurrent is given by [84]

$$\begin{aligned} \delta I(x_0, y_0, \theta) &= -\tanh\left(\frac{\varepsilon}{2k_{\text{B}}T}\right)\frac{2e}{\hbar}\frac{d\varepsilon}{d\phi} \\ &= \frac{e\Delta}{\hbar}\sin(\phi/2-\gamma/2)\tanh\left(\frac{\Delta\cos(\phi/2-\gamma/2)}{2k_{\text{B}}T}\right), \end{aligned} \tag{4.6}$$

including a factor of two from the spin degeneracy. The trajectory dependence enters via the phase shift $\gamma \equiv \gamma(x_0, y_0, \theta)$. Notice that, notwithstanding the appearance of the half-phases $\phi/2$, the supercurrent is 2π-periodic in ϕ — as it should be.

The total supercurrent I through the Josephson junction follows upon integration of Eq. (4.6) over the phase space of the propagating modes at the Fermi level, with measure $dx_0 dk_x/2\pi$:

$$I = \int \frac{dk_x}{2\pi}\int dx_0\, \delta I(x_0, y_0, \theta_{\boldsymbol{k}}). \tag{4.7}$$

[1] At grazing incidence angles $|\theta| \to \pi/2$ the short-junction criterion is more stringent than $L \ll \xi$, we require $L \ll \xi\cos\theta$. In the analytics we ignore this complication, but it is fully incorporated in the numerics.

There is no dependence of I on y_0 because of current conservation.

In zero magnetic field $B = 0 \Rightarrow \gamma = 0$ the dependence of δI on x_0, y_0, θ disappears, so we recover the familiar expression [85]

$$I_0 = k_{\mathrm{F}} W \frac{e\Delta}{\pi\hbar} \sin(\phi/2) \tanh\left(\frac{\Delta\cos(\phi/2)}{2k_{\mathrm{B}}T}\right) \tag{4.8}$$

for the supercurrent in a ballistic Josephson junction. The zero-temperature critical current, reached at $\phi = \pi - 0^+$, is

$$I_{c,0} = k_{\mathrm{F}} W \frac{e\Delta}{\pi\hbar}. \tag{4.9}$$

We also require the spatial distribution of the supercurrent density. To avoid notational complexity we assume that there is a one-to-one relation between $k_x \in (-k_{\mathrm{F}}, k_{\mathrm{F}})$ and $\theta_{\boldsymbol{k}} \in (-\pi/2, \pi/2)$. This applies to a warping of the Fermi circle that keeps it singly-connected and convex. For a circular Fermi surface the measure $dk_x \mapsto k_{\mathrm{F}} \cos\theta \, d\theta$. Upon warping we have instead

$$\frac{dk_x}{2\pi} \mapsto \frac{k_{\mathrm{F}}}{2\pi} \rho(\theta) \cos\theta \, d\theta, \tag{4.10}$$

with a nonuniform angular profile $\rho(\theta)$. The current density can then be written as

$$\begin{pmatrix} j_x \\ j_y \end{pmatrix} = \frac{k_{\mathrm{F}}}{2\pi} \int_{-\pi/2}^{\pi/2} d\theta \, \rho(\theta) \begin{pmatrix} \sin\theta \\ \cos\theta \end{pmatrix} \delta I(x_0, y_0, \theta), \tag{4.11}$$

with $(\sin\theta, \cos\theta)$ a unit vector in the direction of motion (note that θ is the angle with the y-axis, see Fig. 4.2). This is an intuitive expression, but for the calculations it is more convenient to return to k_x as integration variable,

$$\begin{aligned} j_x(x_0, y_0) &= \int \frac{dk_x}{2\pi} \, \delta I(x_0, y_0, \theta_{\boldsymbol{k}}) \tan\theta_{\boldsymbol{k}}, \\ j_y(x_0, y_0) &= \int \frac{dk_x}{2\pi} \, \delta I(x_0, y_0, \theta_{\boldsymbol{k}}). \end{aligned} \tag{4.12}$$

4.4 Supercurrent vortex lattice

To demonstrate the emergence of a supercurrent vortex lattice we calculate the current density at a point (x_0, y_0) in the normal region, in the limit

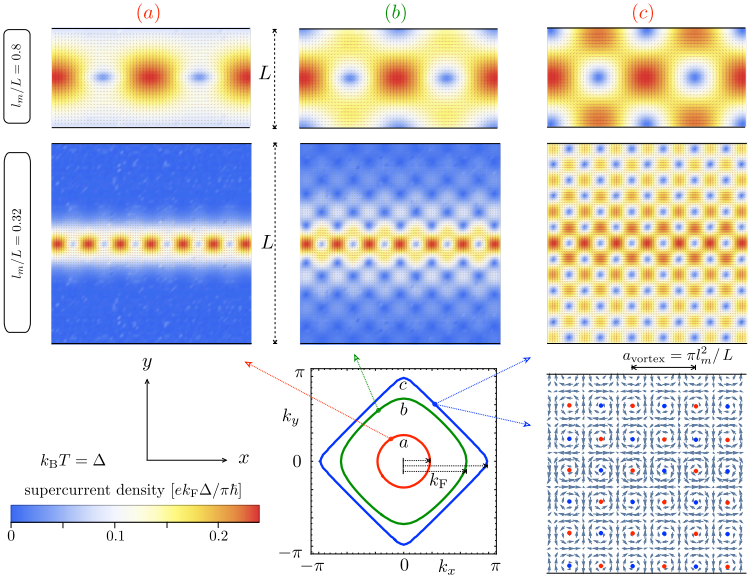

Figure 4.3. The six color scale plots show the supercurrent density in a wide Josephson junction, far from the lateral boundaries, for two values of the magnetic field (first and second row of panels at $l_m/L = 0.8$ and 0.32, respectively) and for three values of the Fermi energy (labeled a, b, c and corresponding to the square-lattice Fermi surfaces at $E_F/E_0 = 0.2$, 0.8, and 0.99, respectively). The plots are calculated from Eqs. (4.3), (4.12), (4.13), at temperature $k_B T = \Delta$. The bottom right panel shows the bipartite vortex lattice (vortices and antivortices indicated by red and blue dots, lattice constant $a_{\rm vortex} = \pi l_m^2/L = 0.32\, L$ at $l_m/L = 0.32$) that develops for $l_m \lesssim L$ in a square-warped Fermi surface.

$W \to \infty$ that boundary effects can be ignored. (These are considered in the next section.) At a given angle θ with the y-axis (see Fig. 4.2), the phase shift γ in Eq. (4.4) equals

$$\gamma = \frac{2L}{l_m^2}(x_0 - y_0 \tan\theta). \tag{4.13}$$

The resulting current density follows from Eq. (4.12) upon integration, once we have specified the relation between k_x and θ. To be definite we take a square lattice dispersion, where $\tan\theta$ is given as a function of k_x by Eq. (4.3). Results are shown in Fig. 4.3.

If the angular distribution $\rho(\theta)$ on the Fermi surface is peaked at angles $\pm\theta_0$, the phase shift (4.13) produces a bipartite rectangular lattice

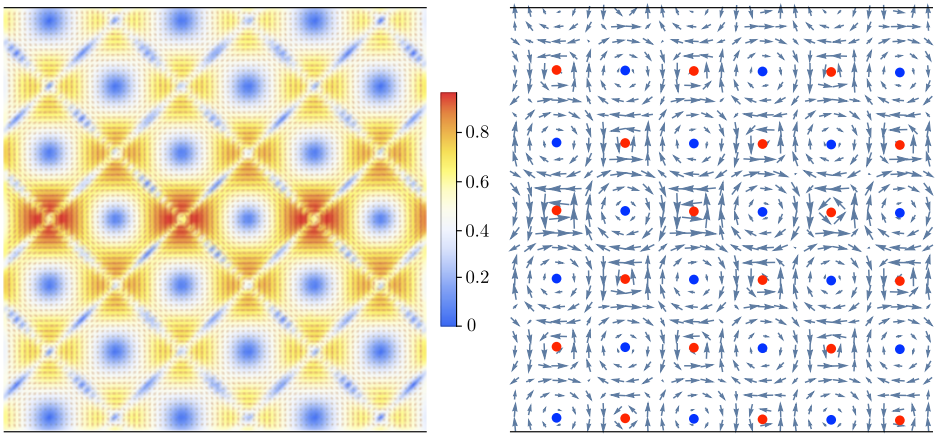

Figure 4.4. Same as Fig. 4.3c for $l_m/L = 0.32$, at a much lower temperature of $k_B T = 0.05\,\Delta$. The vortex and antivortex sublattices (red and blue dots) are no longer equivalent.

of vortex-antivortex pairs. (Notice that the superconducting phase difference ϕ simply shifts the lattice in the x-direction.) The lattice constants are $a_\parallel = a_{\rm vortex}$ parallel to the NS interfaces and $a_\perp = a_{\rm vortex}/\tan\theta_0$ in the perpendicular direction, with $a_{\rm vortex}$ given by Eq. (4.1).

In the square lattice the Fermi surface has a square warping near the center of the band, and if the NS interfaces are oriented along a principal axis one has $\tan\theta_0 = 1$, so the vortex-antivortex lattice is a square lattice with lattice constant $a_{\rm vortex}$ in both directions, see panels (c) in Fig. 4.3. The two-dimensional lattice disappears — leaving only a single row of vortices — if we move away from band center, see panels (a), as the angular distribution $\rho(\theta)$ broadens around normal incidence. Since $a_\perp \to \infty$ for $\theta \to 0$ this broadening of $\rho(\theta)$ produces a broad range of perpendicular lattice constants, which smear out the structure of the vortex lattice in the direction perpendicular to the NS interface. Only the θ-independent structure parallel to the NS interfaces remains.

At the elevated temperatures $k_B T \gtrsim \Delta$ of Fig. 4.3 the vortices and antivortices are equivalent, but at lower temperatures this symmetry between the two sublattices is broken, see Fig. 4.4. Counterclockwise vortices and clockwise antivortices are centered at points where $\phi - \gamma$ equals, respectively, π or 0, modulo 2π. At elevated temperatures the current-phase relationship (4.6) is nearly sinusoidal, with the same slope at $\phi = 0, \pi$ (up to a sign difference). At low temperatures the slope at $\phi = 0$ is not much

affected, so the antivortices retain their circular shape, but the vortices at $\phi = \pi$ see a much larger slope and contract in a square-like shape around the lattice points.

4.5 Edge reconstruction of the vortex lattice

The vortex lattice is modified if we approach the lateral boundaries at $x = \pm W/2$. We still assume $W \gg L$, so we can treat the boundaries separately. At each boundary we impose a hard-wall confinement with specular reflection (see Fig. 4.2).

A trajectory from superconductor S_1 to S_2 that passes through the point (x_0, y_0) at an angle θ with the y-axis is affected by the boundary at $x = W/2$ if x_0 is in the interval

$$\tfrac{1}{2}W - \tfrac{1}{2}L|\tan\theta| + y_0 \tan\theta < x_0 < \tfrac{1}{2}W. \tag{4.14}$$

In this interval the boundary reflection replaces the expression (4.13) for the phase shift γ by

$$\gamma = \beta - \frac{1}{2l_m^2|\tan\theta|}(W - 2x_0 + 2y_0\tan\theta)^2, \tag{4.15a}$$

$$\beta = \frac{LW}{l_m^2}\left(1 - \frac{L|\tan\theta|}{2W}\right), \tag{4.15b}$$

see App. 4.9.1. The corresponding expression for the boundary at $x = -W/2$ follows from the symmetry relation

$$\gamma(x_0, y_0, \theta) = -\gamma(-x_0, y_0, -\theta). \tag{4.16}$$

The resulting supercurrent distribution near the boundary is shown in Fig. 4.5. For $l_m \lesssim L$ an edge channel appears when the Fermi surface is strongly warped, see panel (c), becoming less pronounced as the Fermi surface becomes more and more circular, see panels (b) and (a). The streamlines in the edge channel inherit their periodicity from the vortex lattice, but the width $w_{\rm edge} \simeq l_m$ of the edge channel is larger than $a_{\rm vortex} \simeq l_m^2/L$. The net current flowing along the edge channel is sensitive to the phase difference ϕ between superconductors S_1 and S_2, see Fig. 4.6.

To understand this edge reconstruction of the vortex lattice, we note that because the phase shift γ now depends quadratically rather than linearly on x_0, there is a point of stationary phase: $\partial\gamma/\partial x_0 = 0$ at $x_0 =$

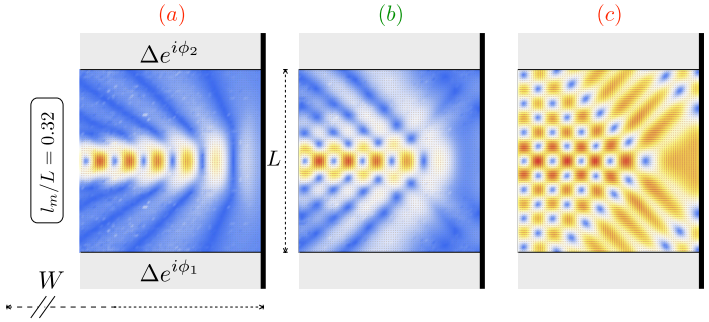

Figure 4.5. Effect of a hard-wall lateral boundary on the supercurrent vortex lattice. The panels a,b,c correspond to the three labeled Fermi surfaces in Fig. 4.3, with the same color scale; the other parameters are $l_m/L = 0.32$, $W/L = 10.16$, $\phi_1 - \phi_2 \equiv \phi = \pi/2$, and $k_B T = \Delta$.

$y_0 \tan\theta + W/2$. For a warped Fermi surface with $\rho(\theta)$ peaked at $\pm\theta_0$ an edge channel extends along the lines of stationary phase, of width

$$w_{\rm edge} \equiv 2\left|\partial^2\gamma/\partial x_0^2\right|^{-1/2} = l_m\sqrt{\tan\theta_0}. \tag{4.17}$$

The edge channel carries a net current from S_1 to S_2 that depends on the parameter β and the superconductor phase difference ϕ: the edge current is minimal for $\phi - \beta = 0$ and maximal for $\phi - \beta = \pi/2$, modulo π. (In Fig. 4.6 we have $\beta \approx 0 \mod \pi$, so minimal and maximal current corresponds to $\phi = 0$ and $\pi/2$, respectively.) As we will show in the next section, this edge current produces a critical current of order $(w_{\rm edge}/W)I_{c,0}$, with the anomalously slow decay $\propto 1/\sqrt{B}$.

4.6 High-field decay of the Fraunhofer oscillations

To obtain the critical current $I_c = \max_\phi I(\phi)$ of the Josephson junction, we first need to calculate at a given phase difference ϕ the total supercurrent $I(\phi)$ by integrating $j_y(x_0, y_0)$ over x_0 from $-W/2$ to $W/2$. From Eq. (4.11) we thus have

$$I = \frac{k_F}{2\pi}\int_{-\pi/2}^{\pi/2}\rho(\theta)\cos\theta\, d\theta \int_{-W/2}^{W/2} dx_0\, \delta I(x_0, y_0, \theta). \tag{4.18}$$

Analytical progress is simplest in the high-temperature regime $k_B T \gtrsim \Delta$, when the ϕ-dependence of δI from Eq. (4.6) becomes approximately

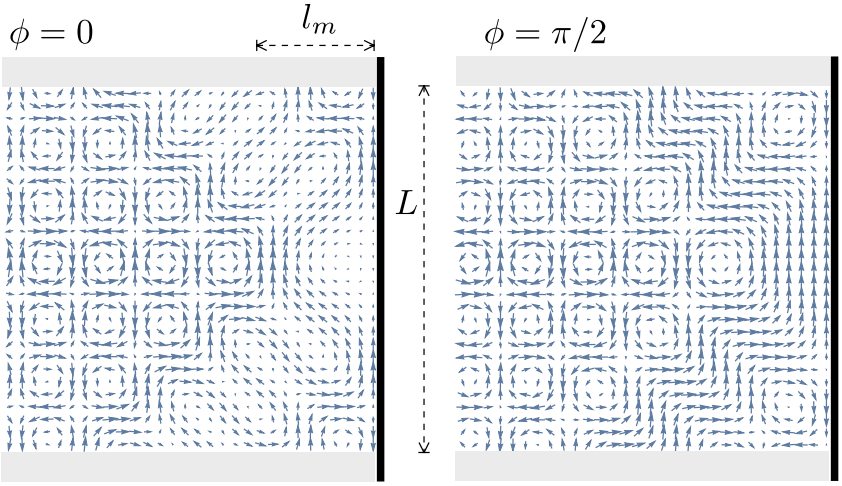

Figure 4.6. Streamlines corresponding to the vortex lattice in panel (c) of Fig. 4.5, for two values of the superconducting phase difference $\phi = \phi_1 - \phi_2$ (all other parameters are kept the same). The left and right panels correspond, respectively, to minimal and maximal current flowing along the edge channel.

sinusoidal,

$$\delta I \approx \frac{e\Delta^2}{4\hbar k_{\rm B} T} \sin(\phi - \gamma), \quad \gamma = \frac{2e}{\hbar} \int_{S_1}^{S_2} \boldsymbol{A} \cdot d\boldsymbol{l}. \tag{4.19}$$

We assume that the velocity distribution on the Fermi surface is symmetric around normal incidence, $\rho(\theta) = \rho(-\theta)$. Because of Eq. (4.16) we may then restrict the θ-integration in Eq. (4.18) to positive angles,

$$\begin{aligned} I = {} & \frac{e\Delta^2 k_{\rm F}}{8\pi\hbar k_{\rm B} T} \int_0^{\pi/2} \rho(\theta) \cos\theta \, d\theta \int_{-W/2}^{W/2} dx_0 \\ & \times [\sin(\phi - \gamma) + \sin(\phi + \gamma)]. \end{aligned} \tag{4.20}$$

We thus find that the integrated supercurrent retains a sinusoidal ϕ-dependence, with critical current

$$\begin{aligned} I_c &= I_{c,0} \left| \int_0^{\pi/2} \rho(\theta) \cos\theta \, d\theta \int_{-W/2}^{W/2} \frac{dx_0}{W} \cos\gamma \right|, \\ I_{c,0} &= \frac{e\Delta^2 k_{\rm F} W}{4\pi\hbar k_{\rm B} T}. \end{aligned} \tag{4.21}$$

In the interval $0 < \theta < \arctan(W/L)$ there is at most one boundary collision. We restrict ourselves to this interval, because the contributions to I_c near grazing incidence are anyway suppressed exponentially at finite temperature. (All contributions are included in the numerics.) Fixing the arbitrary y-coordinate at $y_0 = -L/2$, we have from Eqs. (4.13) and (4.15) the expression for γ that we need:

$$\gamma = \frac{2L}{l_m^2}(x_0 + \tfrac{1}{2}L\tan\theta) \;\text{ if }\; x_0 + L\tan\theta < W/2, \tag{4.22a}$$

$$\gamma = \beta - \frac{(W - 2x_0 - L\tan\theta)^2}{2l_m^2\tan\theta} \;\text{ if }\; x_0 + L\tan\theta > W/2, \tag{4.22b}$$

with β defined in Eq. (4.15b).

The integral over x_0 in Eq. (4.21) can be carried out analytically:

$$I_c = I_{c,0}\left|\int_0^{\pi/2}\rho(\theta)\Gamma(\theta)\cos\theta\,d\theta\right|, \tag{4.23}$$

$$\Gamma(\theta) \equiv \int_{-W/2}^{W/2}\frac{dx_0}{W}\cos\gamma = \frac{l_m^2}{LW}\sin\beta' \tag{4.24}$$
$$+ (l_m/W)\sqrt{\pi\tan\theta}[F_C(\alpha)\cos\beta + F_S(\alpha)\sin\beta],$$

$$\alpha = \frac{L\sqrt{\tan\theta}}{l_m\sqrt{\pi}},\quad \beta' = \frac{LW}{l_m^2}\left(1 - \frac{L}{W}\tan\theta\right). \tag{4.25}$$

The functions F_C and F_S are the Fresnel cosine and sine integrals,

$$F_C(\alpha) = \int_0^\alpha \cos(\tfrac{\pi}{2}t^2)\,dt,\quad F_S(\alpha) = \int_0^\alpha \sin(\tfrac{\pi}{2}t^2)\,dt. \tag{4.26}$$

Both $F_C(\alpha)$ and $F_S(\alpha)$ tend to $1/2$ for $\alpha \to \infty$.

If the angular distribution $\rho(\theta)$ is sharply peaked around $\pm\theta_0$, we obtain from Eqs. (4.23) and (4.24) the high-field ($l_m \ll L$) critical current

$$I_c(\text{high-field}) = I_{c,0}\frac{w_{\text{edge}}}{W}\sqrt{\pi/2}\left|\sin\left(\frac{\pi}{4} + \frac{LW_{\text{eff}}}{l_m^2}\right)\right|, \tag{4.27}$$

with effective junction width $W_{\text{eff}} = W - \frac{1}{2}L\tan\theta_0$ and edge channel width $w_{\text{edge}} = l_m\sqrt{\tan\theta_0}$. Comparing with the low-field ($l_m \gg L$) Fraunhofer oscillations,

$$I_c(\text{low-field}) = I_{c,0}\frac{l_m^2}{LW}\left|\sin(LW/l_m^2)\right|, \tag{4.28}$$

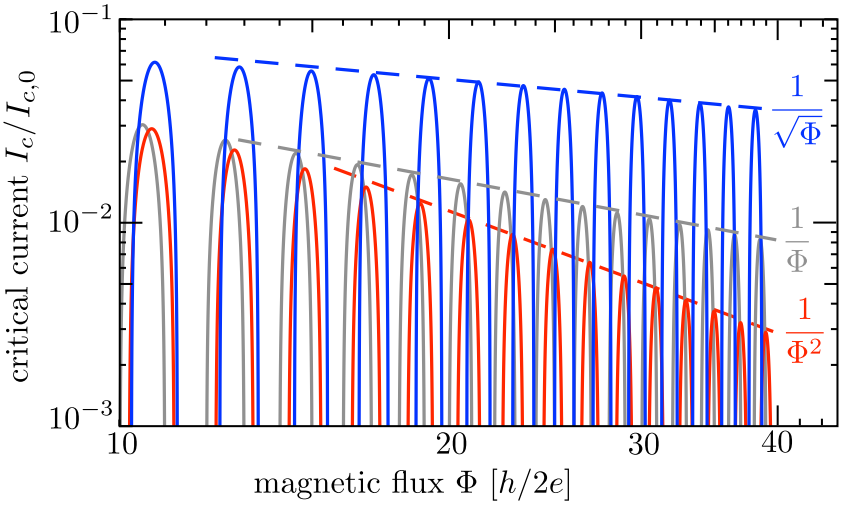

Figure 4.7. Log-log plot of the critical current I_c versus the flux Φ through the normal region (aspect ratio $W/L = 10.16$), calculated from Eq. (4.23) for a circular Fermi surface ($\rho(\theta) = 1$, red curve decaying $\propto 1/\Phi^2$), and for a square Fermi surface ($\rho(\theta) = \delta(\theta - \pi/4)$, blue curve decaying $\propto 1/\sqrt{\Phi}$). The low-field Fraunhofer oscillations (4.28) are included for comparison (grey curve decaying $\propto 1/\Phi$).

we note three differences: the amplitude decays more slowly, $\propto 1/\sqrt{B}$ instead of $\propto 1/B$; the flux periodicity is larger by a factor W/W_{eff}; and the maxima are phase shifted by 1/4 flux quantum. This qualitatively different behavior is illustrated in Fig. 4.7, compare blue and grey curves.

At the other extreme of an isotropic angular distribution, for a circular Fermi surface, we obtain the opposite effect: instead of a slower decay of the high-field Fraunhofer oscillations the decay is faster, $\propto 1/B^2$ instead of $\propto 1/B$, compare red and blue curves.[2] This accelerated decay is a known result [69]. What we have found here is that the switch from a circular to a square Fermi surface slows down the decay by a fourth root, from B^{-2} to $B^{-1/2}$.

[2] The $1/B^2$ decay of the critical current for a circular Fermi surface follows upon numerical integration of Eq. (4.23) with $\rho(\theta) = 1$, see Fig. 4.7. Unlike the $1/\sqrt{B}$ decay for a square Fermi surface, we have not managed to derive the $1/B^2$ decay analytically.

4.7 Numerical simulations

To test the analytical semiclassical theory we have performed numerical simulations of a tight-binding model. We start from the Bogoliubov-De Gennes Hamiltonian,

$$H(\boldsymbol{k}) = \begin{pmatrix} E(\boldsymbol{k} - e\boldsymbol{A}) - E_{\mathrm{F}} & \Delta \\ \Delta^* & E_{\mathrm{F}} - E(\boldsymbol{k} + e\boldsymbol{A}) \end{pmatrix}, \tag{4.29}$$

with the single-particle dispersion $E(\boldsymbol{k})$ on a square lattice given by Eq. (4.2). The pair potential Δ and vector potential $\boldsymbol{A}$ are chosen as in Fig. 4.2, with $\Delta = 0$ for $|y| < L/2$ (no pairing interaction in the normal region) and $\boldsymbol{A} = 0$ for $|y| > L/2$ (complete screening of the magnetic field from the superconductor). The self-field of the currents in the normal region is neglected, so $\boldsymbol{A}$ is entirely due to the externally imposed field B. The orbital effect of the magnetic field is fully included, but we neglect the coupling to the electron spin[3] and can therefore omit the spin degree of freedom from the Hamiltonian.

The 2×2 matrix Green's function $G(\varepsilon) = (\varepsilon - H)^{-1}$ is calculated at imaginary energy $\varepsilon = i\omega$ using the Kwant toolbox for tight-binding models [16]. The expectation value of the current density in thermal equilibrium,

$$\boldsymbol{j}(\boldsymbol{r}) = \frac{2e}{\hbar} k_{\mathrm{B}} T \,\mathrm{Re} \sum_{p=0}^{\infty} \mathrm{Tr}\, \langle \boldsymbol{r}|G(i\omega_p)|\boldsymbol{r}\rangle \langle \boldsymbol{r}|\frac{\partial H}{\partial \boldsymbol{k}}|\boldsymbol{r}\rangle, \tag{4.30}$$

is then obtained from a (rapidly convering) sum over Matsubara frequencies $\omega_p = (2p+1)\pi k_{\mathrm{B}} T$ [73]. (See Ref. [87] for an alternative approach.)

The time-consuming step in this calculation is the calculation of the inverse operator $(i\omega - H)^{-1}$, but once this is done for one value of the superconducting phase difference ϕ, we can use Dyson's equation to obtain the result for other values of ϕ without further inversions.

Results for the vortex lattice in the case of a nearly square Fermi surface ($E_{\mathrm{F}}/E_0 = 0.99$) are shown in Figs. 4.1 and 4.8. The agreement with the semiclassical result is not fully quantitative, see Fig. 4.9, but all

[3] As explained in [86], the influence of the Zeeman energy on the Josephson effect is quantified by the phase shift $\theta = g\mu_B BL/\hbar v_{\mathrm{F}} = \frac{1}{2} gL/l_{\mathrm{cycl}}$. In the magnetic field regime where the cyclotron radius $l_{\mathrm{cycl}} = mv_{\mathrm{F}}/eB$ is large compared to the separation L of the NS interfaces (which is the regime of interest here), the condition $\theta \ll 1$ is ensured provided the g-factor is not much larger than unity.

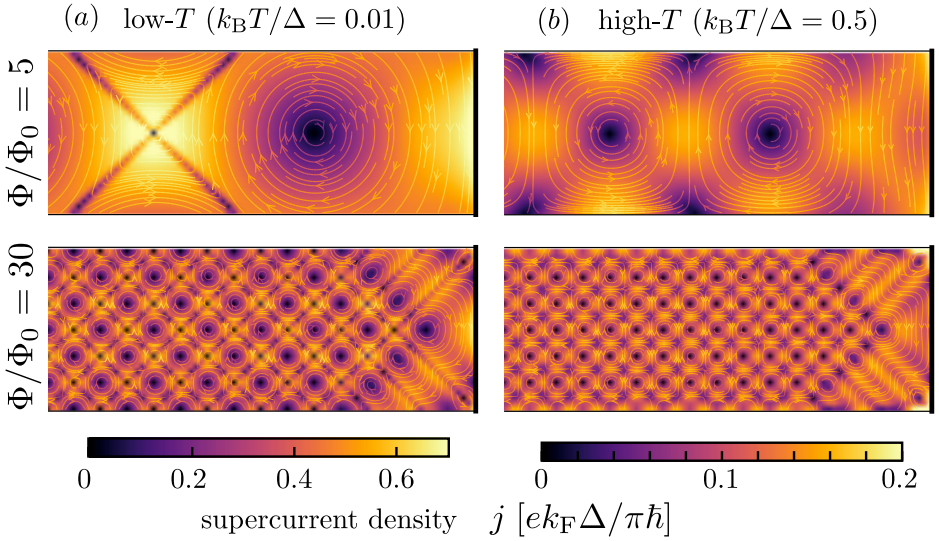

Figure 4.8. (a): Same as Fig. 4.1, zoomed in at the right boundary. (b): At a higher temperature the vortices and antivortices are approximately equivalent.

the qualitative features of the vortex lattice coming out of the analytics are well reproduced in the numerics. Also the $1/\sqrt{B}$ decay is recovered in the simulation, see Fig. 4.10.

In both the analytics and numerics so far we took a ballistic Josephson junction, without any disorder in the normal region, and ideal (fully transparent) NS interfaces. The numerical simulation provides a way to test for the effects of impurity scattering and nonideal interfaces. Disorder was modeled by adding a random component δU to the on-site electrostatic potential, drawn uniformly from the interval $[-U_0, U_0]$. For the tunnel barrier we reduced the hopping amplitude at the two NS interfaces. As shown in Fig. 4.11, the slow $1/\sqrt{B}$ decay persists even if the critical current is reduced substantially by the tunnel barrier. Disorder provides a stronger perturbation, in the form of random sample-specific fluctuations [69], but averaged over series of peaks the slow decay persists.

4.8 Discussion

Two-dimensional vortex lattices are well established for Abrikosov vortices in a bulk superconductor [9], but Josephson vortices in an SNS junction

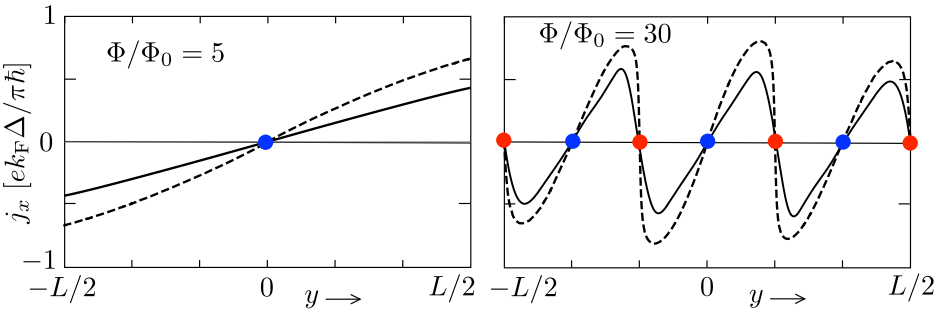

Figure 4.9. Current density profile along a cut through $x = 0$, for the same parameters as Fig. 4.1. Since $j_y = 0$ along this cut, the plotted j_x is the full current density. The red and blue dots identify the center of a vortex or antivortex, which are distinct at this low temperature of $k_BT = 0.01\,\Delta$. The solid curves are the results of the numerical simulation, the dashed curves are the semiclassical result (4.12) in the short-junction regime.

were only known to arrange as a *one-dimensional* chain [25, 78, 80]. Our key conceptual finding is that the 2D arrangement is hidden by angular averaging over the Fermi surface. For a distribution of angles of incidence peaked at $\pm\theta$, resulting from a strong square or hexagonal warping of the Fermi surface, a 2D lattice develops when the magnetic length $l_m = \sqrt{\hbar/eB}$ drops below the separation L of the NS interfaces. The lattice is bipartite, with a vortex and antivortex in a rectangular unit cell of size $\pi l_m^2/L$ parallel to the interface and $\pi l_m^2/(L\tan\theta)$ perpendicular to the interface. For a circular Fermi surface the 2D lattice degrades to a 1D chain.

It would be interesting to search for this 2D Josephson vortex lattice in some of the quasi-two-dimensional systems that are known to have a warped Fermi surface, such as the hexagonal warping on the surface of a three-dimensional topological insulator [88]. By way of illustration, Fig. 4.12 shows the vortex lattice calculated for the [111] surface dispersion of Bi_2Te_3 [89],

$$E_{\boldsymbol{k}} = E_0\sqrt{\lambda^2k_x^2 + \lambda^2k_y^2 + \lambda^6(k_x^3 - 3k_xky^2)^2}, \tag{4.31}$$

with the x-axis (the NS interface) oriented along the ΓK direction in the Brillouin zone.

The vortices could be detected directly by a scanning tunneling probe [90–92], or indirectly through the flux Φ-dependent Fraunhofer oscillations [93,

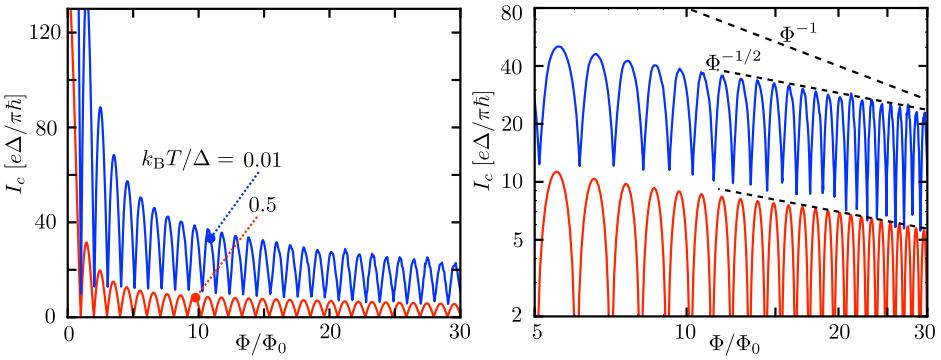

Figure 4.10. Plot of the critical current I_c versus the flux Φ through the normal region, resulting from the numerical simulation with the parameters of Figs. 4.1 and 4.8. The minima of the Fraunhofer oscillations no longer go to zero at low temperatures (blue curves), because of the skewed current-phase relationship. The upper panel shows a linear scale, the lower panel a log-log scale with the $\Phi^{-1/2}$ decay indicated (black dashed line). (The $1/\Phi$ decay of the conventional Fraunhofer oscillations is also included for comparison.)

94] — we have found that the transition from a 1D to a 2D arrangement of vortices is accompanied by a slow-down of the decay of the oscillation amplitude from $1/\Phi$ to $1/\sqrt{\Phi}$. While in the main text we have focused on the current distribution, we note that a 2D lattice structure with the same periodicity appears also in the superconducting pair potential (see App. 4.9.2) and in the local density of states (see App. 4.9.3).

A particularly intriguing feature of the vortex lattice is the reconstruction at the edge, resulting in an edge channel of width $\simeq l_m$ parametrically larger than the lattice constant. It is this edge channel that effectively carries the supercurrent when $l_m \lesssim L$, resulting in the decay scaling as $l_m/W \propto 1/\sqrt{B}$. Notice that the edge channel appears entirely as a result of quantum interference — in contrast to the quantum Hall edge channel any orbital effects of the magnetic field play no role here.

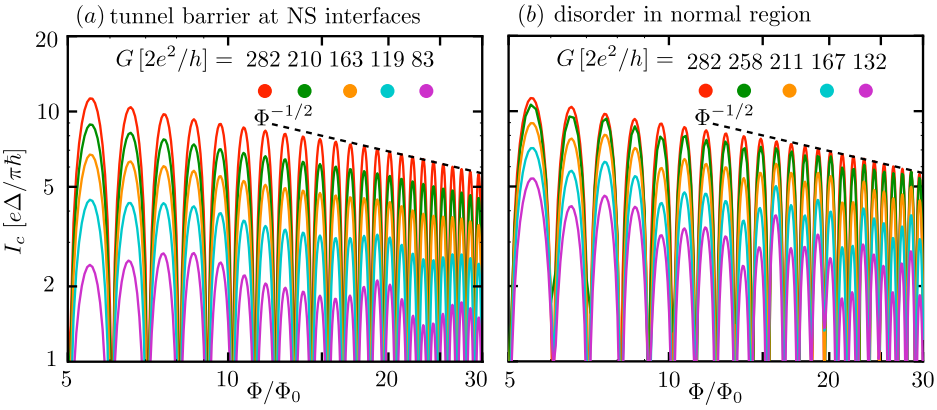

Figure 4.11. Effect on the Fraunhofer oscillations of a tunnel barrier at the NS interfaces (panel a) or of disorder in the normal region (panel b). The data results from the numerical simulation with the parameters of Fig. 4.8b. The disorder strength or tunnel barrier height is quantified by the reduction of the normal state conductance G. The topmost (red) curve corresponds to the ideal case without disorder or tunnel barrier.

4.9 Appendix

4.9.1 Calculation of the Aharonov-Bohm phase shift

We calculate the Aharonov-Bohm phase shift

$$\gamma = \frac{2e}{\hbar} \int_{S_1}^{S_2} \boldsymbol{A} \cdot d\boldsymbol{l} \tag{4.32}$$

accumulated along a trajectory across the Josephson junction, from superconductor S_1 at $y = -L/2$ to S_2 at $y = +L/2$, including the effects of multiple specular reflections at the side walls $x = \pm W/2$. The geometry is shown in Fig. 4.2. Assume that the trajectory starts at $t = 0$ from the point $x = x(0)$, $y = -L/2$ at the lower NS interface, at an angle $\theta(0) \in (-\pi/2, \pi/2)$ with the positive y-axis. The opposite NS interface at $y = L/2$ is reached at the time $t_L = L/v_y$, with $v_y = v_{\rm F} \cos\theta(0)$ the velocity component in the y-direction (which does not change at a boundary reflection).

In the gauge $\boldsymbol{A} = (0, Bx, 0)$ the line integral takes the form

$$\gamma = \frac{2v_y}{l_m^2} \int_0^{t_L} x(t) dt. \tag{4.33}$$

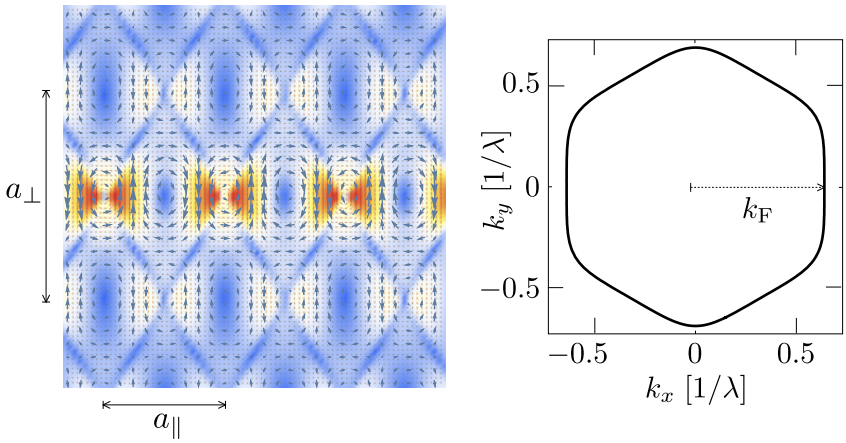

Figure 4.12. Vortex lattice for a Fermi surface having the hexagonal warping of the Bi_2Te_3 dispersion relation (4.31) (parameters $\lambda \approx 1\,\mathrm{nm}$, $E_0 \approx 260\,\mathrm{meV}$, $E_F = 6^{-3/4}\sqrt{7}\,E_0$, $k_F = 6^{-1/4}\lambda^{-1}$, other parameters and color scale as in Fig. 4.4). The difference with square warping is that the lattice is rectangular rather than square, with aspect ratio $a_\perp/a_\parallel = 1/\tan(\pi/6) = \sqrt{3}$.

The time dependence of $x(t)$ is given by

$$\begin{aligned} x(t) &= (-1)^{\nu_{u(t)}}[u(t) - \nu_{u(t)}W], \\ u(t) &= x(0) + v_F t \sin\theta(0), \end{aligned} \tag{4.34}$$

where we have defined $\nu_u \in \mathbb{Z}$ as the integer nearest to u/W. The absolute value of ν counts the number of boundary reflections up to time t. At time $t_L = L/[v_F \cos\theta(0)]$ we have

$$x(t_L) = (-1)^{\nu_L}[x(0) + L\tan\theta(0) - \nu_L W], \tag{4.35}$$

where $\nu_L \equiv \nu_{u(t_L)}$ is the integer nearest to $[x(0) + L\tan\theta(0)]/W$.

Integration of Eq. (4.33) results in

$$\gamma = \frac{1}{l_m^2 \tan\theta(0)} \left(\tfrac{1}{4}W^2 - x^2(0) + (-1)^{\nu_L}\left[x^2(t_L) - \tfrac{1}{4}W^2\right] \right). \tag{4.36}$$

This is sufficient to calculate the total current through the Josephson junction, by integrating the current density through the lower NS interface.

To obtain the current distribution within the junction, say at the point (x_0, y_0), we need to find the corresponding coordinates $(x(0), -L/2)$ of

the trajectory at the lower NS interface. The angle θ at the point (x_0, y_0) equals $\pm\theta(0)$. The point (x_0, y_0) is reached at a time $t_0 = (y_0 + L/2)/v_y$ after

$$\nu_0 = \nu_{x_0 - v_{\rm F} t_0 \sin\theta} = \nu_{x_0 - (y_0 + L/2)\tan\theta} \tag{4.37}$$

boundary reflections. Retracing back the trajectory, we find

$$\begin{aligned} x(0) &= (-1)^{\nu_0}[x_0 - (y_0 + L/2)\tan\theta - \nu_0 W], \\ \theta(0) &= (-1)^{\nu_0}\theta. \end{aligned} \tag{4.38}$$

This calculation of the Aharonov-Bohm phase γ holds for any number of boundary collisions at $x = \pm W/2$. In the main text we only need the result for a single boundary collision at $x = W/2$. One readily checks that Eq. (4.36) reduces to Eq. (4.15) upon substitution of $\nu_L = 1$, $\nu_0 = 0$ for $\tan\theta > 0$ or $\nu_L = 1$, $\nu_0 = 1$ for $\tan\theta < 0$.

4.9.2 Two-dimensional lattice structure of the superconducting order parameter

The coherent superposition of electrons and holes in an Andreev level produces a nonzero order parameter $F(\boldsymbol{r})$ in the normal region, in the absence of any pairing interaction [9]. In this appendix we show that the amplitude $|F|$ has a 2D lattice structure with the same periodicity as the current vortex lattice studied in the main text.

An Andreev level in the SNS junction of Fig. 4.2, at the positive energy

$$\varepsilon = \Delta\cos(\psi/2), \quad \psi = \phi_1 - \phi_2 - \gamma \in (-\pi, \pi), \tag{4.39}$$

has a wave function $\Psi(\boldsymbol{r})$ that penetrates into the superconducting regions $|y| > L/2$ over a distance

$$\xi_\varepsilon = \hbar v_y(\Delta^2 - \varepsilon^2)^{-1/2} = (\hbar v_y/\Delta)|\sin(\psi/2)|^{-1}. \tag{4.40}$$

In the normal region $|y| < L/2$ the wave function has a constant amplitude, given in WKB approximation by [82]

$$\Psi(\boldsymbol{r}) = \begin{pmatrix} u(\boldsymbol{r}) \\ v(\boldsymbol{r}) \end{pmatrix} = (2\xi_\varepsilon)^{-1/2} e^{i\boldsymbol{k}\cdot\boldsymbol{r}} \begin{pmatrix} e^{i\eta/2} \\ e^{-i\eta/2} \end{pmatrix}. \tag{4.41}$$

The electron and hole components u, v differ in phase by

$$\eta = \tfrac{1}{2}(\phi_1 + \phi_2 + \gamma) - \frac{2e}{\hbar}\int_{S_1}^{\boldsymbol{r}} \boldsymbol{A}\cdot d\boldsymbol{l}, \tag{4.42}$$

in accord with the Andreev reflection boundary condition at the NS interfaces [84],

$$\eta = \begin{cases} \phi_1 - \sigma \arccos(\varepsilon/\Delta) & \text{at } y = -L/2, \\ \phi_2 + \sigma \arccos(\varepsilon/\Delta) & \text{at } y = +L/2. \end{cases} \tag{4.43}$$

We have defined $\sigma = \operatorname{sign}\psi$, so that $\arccos(\varepsilon/\Delta) = \sigma\psi/2$ for $\psi \in (-\pi, \pi)$.

The electron-hole mode (u, v) at energy ε contributes to the superconducting order parameter an amount [9]

$$\delta F(\boldsymbol{r}) = \tanh\left(\frac{\varepsilon}{2k_{\mathrm{B}}T}\right) u^*(\boldsymbol{r}) v(\boldsymbol{r}). \tag{4.44}$$

Integration over the modes gives the full order parameter,

$$\begin{aligned} F(\boldsymbol{r}) &= \int \frac{dk_x}{2\pi} \delta F(\boldsymbol{r}) \\ &= \frac{k_{\mathrm{F}}}{2\pi} \int_{-\pi/2}^{\pi/2} d\theta\, \rho(\theta) \cos\theta \tanh\left(\frac{\varepsilon}{2k_{\mathrm{B}}T}\right) \frac{e^{-i\eta}}{2\xi_\varepsilon}. \end{aligned} \tag{4.45}$$

This expression has the proper 2π-periodicity in the superconducting phase, since $\eta \mapsto \eta + \pi$ and $\varepsilon \mapsto -\varepsilon$ if ϕ_1 or ϕ_2 is incremented by 2π.

We evaluate $F(\boldsymbol{r})$ in a wide SNS junction, at a point $\boldsymbol{r} = (x_0, y_0)$ far from the lateral boundaries. A mode passing through this point at an angle θ relative to the y-axis has Aharonov-Bohm phase

$$\begin{aligned} \frac{2e}{\hbar} \int_{S_1}^{r} \boldsymbol{A} \cdot d\boldsymbol{l} &= \frac{(y_0 + L/2)}{l_m^2} [2x_0 - (y_0 + L/2)\tan\theta], \\ \gamma = \frac{2e}{\hbar} \int_{S_1}^{S_2} \boldsymbol{A} \cdot d\boldsymbol{l} &= \frac{2L}{l_m^2}(x_0 - y_0 \tan\theta), \end{aligned} \tag{4.46}$$

so that the phase shift (4.42) is given by

$$\eta = \bar{\phi} - \frac{2x_0 y_0}{l_m^2} + \frac{y_0^2 + \frac{1}{4}L^2}{l_m^2} \tan\theta, \quad \bar{\phi} = \tfrac{1}{2}(\phi_1 + \phi_2). \tag{4.47}$$

For the warped Fermi surface of a square lattice (unit lattice constant, see Sec. 4.2) we have

$$\tan\theta = \frac{\sin k_x}{\Xi}, \quad v_y = \frac{E_0 \Xi}{2\hbar}, \tag{4.48}$$

$$\psi = \phi_1 - \phi_2 - \frac{2L}{l_m^2}\left(x_0 - \frac{y_0}{\Xi}\sin k_x\right), \tag{4.49}$$

$$\Xi = \sqrt{1 - (\cos k_x + 2E_{\mathrm{F}}/E_0 - 2)^2}. \tag{4.50}$$

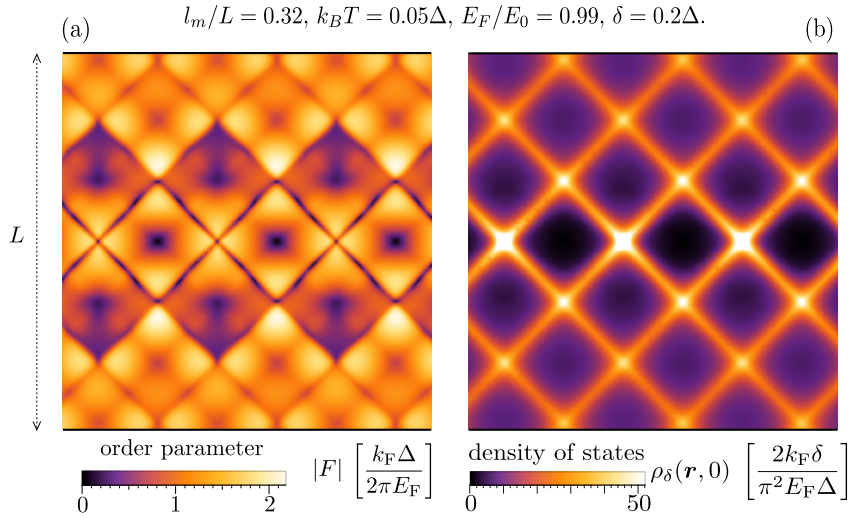

Figure 4.13. (a) Absolute value of the superconducting order parameter $F(\boldsymbol{r})$, calculated from Eq. (4.51). Current vortices and antivortices in Fig. 4.4 correspond to local minima of $|F|$. (b) Local density of states ρ_δ at the Fermi level (with a Lorentzian broadening δ), calculated from Eq. (4.54). Current vortices and antivortices in Fig. 4.4 correspond to local maxima and minima of ρ_δ.

The order parameter then results from the integral

$$F(\boldsymbol{r}) = \frac{\Delta}{2\pi E_0} e^{-i\bar{\phi}} \exp(2ix_0y_0/l_m^2) \int_{-k_F}^{k_F} dk_x \, \frac{1}{\Xi} \, |\sin(\psi/2)| \\ \times \tanh\left(\frac{\Delta\cos(\psi/2)}{2k_BT}\right) \exp\left(-\frac{i(y_0^2 + \frac{1}{4}L^2)}{l_m^2\Xi} \sin k_x\right), \tag{4.51}$$

with $k_F = \arccos(1-2E_F/E_0)$. The resulting 2D lattice structure is shown in Fig. 4.13(a), corresponding to the current vortex lattice of Fig. 4.4.

4.9.3 Two-dimensional lattice structure of the density of states

To complete the picture, we also demonstrate the development of a 2D lattice structure in the density of states. The states at $\pm\varepsilon$ contribute $|\Psi(\boldsymbol{r})|^2[\delta(E+\varepsilon) + \delta(E-\varepsilon)]$ to the local density of states $\rho(\boldsymbol{r}, E)$. The

total contribution is

$$\rho(\boldsymbol{r},E) = \int \frac{dk_x}{2\pi}\left(|u(\boldsymbol{r})|^2+|v(\boldsymbol{r})|^2\right)\sum_{\sigma=\pm}\delta(E-\sigma\varepsilon)$$
$$= \int \frac{dk_x}{2\pi}\frac{\Delta}{\hbar v_y}|\sin(\psi/2)|\sum_{\sigma=\pm}\delta\big(E-\sigma\Delta\cos(\psi/2)\big). \tag{4.52}$$

We regularize the delta function by introducing a Lorentzian broadening δ,

$$\rho_\delta(\boldsymbol{r},E) = \int \frac{dk_x}{2\pi}\frac{\Delta}{\hbar v_y}\sum_{\sigma=\pm}\frac{(\delta/\pi)|\sin(\psi/2)|}{\delta^2+\big(E-\sigma\Delta\cos(\psi/2)\big)^2}. \tag{4.53}$$

At the Fermi level, $E=0$, we evaluate

$$\rho_\delta(\boldsymbol{r},0) = \frac{2\delta}{\pi^2 E_0\Delta}\int_{-k_\mathrm{F}}^{k_\mathrm{F}} dk_x\,\frac{\Xi^{-1}|\sin(\psi/2)|}{(\delta/\Delta)^2+\cos^2(\psi/2)}. \tag{4.54}$$

The resulting 2D lattice is shown in Fig. 4.13(b).

Chapter 5

Valley-momentum locking in a graphene superlattice with Y-shaped Kekulé bond texture

5.1 Introduction

The coupling of orbital and spin degrees of freedom is a promising new direction in nano-electronics, referred to as "spin-orbitronics", that aims at non-magnetic control of information carried by charge-neutral spin currents [95–97]. Graphene offers a rich platform for this research [98, 99], because the conduction electrons have three distinct spin quantum numbers: in addition to the spin magnetic moment $s = \pm 1/2$, there is the sublattice pseudospin $\sigma =$ A,B and the valley isospin $\tau = K, K'$. While the coupling of the electron spin s to its momentum p is a relativistic effect, and very weak in graphene, the coupling of σ to p is so strong that one has a pseudospin-momentum locking: the pseudospin points in the

The contents of this chapter have been published at O. V. Gamayun, V. P. Ostroukh, N. V. Gnezdilov, İ. Adagideli, and C. W. J. Beenakker, New J. Phys. **20**, 023016 (2018) and may be used under the terms of the Creative Commons Attribution 3.0 licence.

direction of motion, as a result of the helicity operator $\boldsymbol{p}\cdot\boldsymbol{\sigma} \equiv p_x\sigma_x + p_y\sigma_y$ in the Dirac Hamiltonian of graphene.

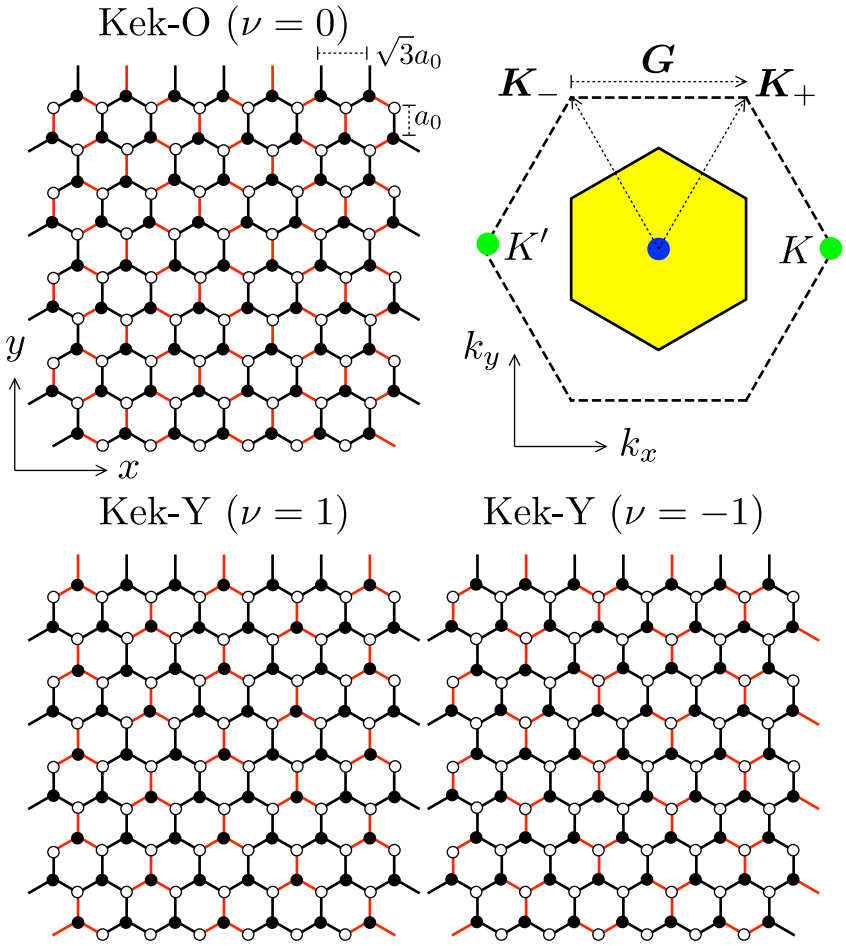

Figure 5.1. Honeycomb lattices with a Kek-O or Kek-Y bond texture, all three sharing the same superlattice Brillouin zone (yellow hexagon, with reciprocal lattice vectors $\boldsymbol{K}_\pm$). Black and white dots label A and B sublattices, black and red lines distinguish different bond strengths. The lattices are parametrized according to Eq. (5.4) (with $\phi = 0$) and distinguished by the index $\nu = 1 + q - p$ modulo 3 as indicated. The K and K' valleys (at the green Dirac points) are coupled by the wave vector $\boldsymbol{G} = \boldsymbol{K}_+ - \boldsymbol{K}_-$ of the Kekulé bond texture and folded onto the center of the superlattice Brillouin zone (blue point).

The purpose of this work is to propose a way to obtain a similar handle

on the valley isospin, by adding a term $\boldsymbol{p} \cdot \boldsymbol{\tau}$ to the Dirac Hamiltonian, which commutes with the pseudospin helicity and locks the valley to the direction of motion. We find that this valley-momentum locking should appear in a superlattice that has recently been realized experimentally by Gutiérrez *et al.* [15, 100, 101]: a superlattice of graphene grown epitaxially onto Cu(111), with the copper atoms in registry with the carbon atoms. One of six carbon atoms in each superlattice unit cell ($\sqrt{3} \times \sqrt{3}$ larger than the original graphene unit cell) have no copper atoms below them and acquire a shorter nearest-neighbor bond. The resulting Y-shaped periodic alternation of weak and strong bonds (see Fig. 5.1) is called a Kekulé-Y (Kek-Y) ordering, with reference to the Kekulé dimerization in a benzene ring (called Kek-O in this context) [101].

The Kek-O and KeK-Y superlattices have the same Brillouin zone, with the K and K' valleys of graphene folded on top of each other. The Kek-O ordering couples the valleys by opening a gap in the Dirac cone [27, 28, 102–104], and it was assumed by Gutiérrez *et al.* that the same applies to the Kek-Y ordering [15, 101]. While it is certainly possible that the graphene layer in the experiment is gapped by the epitaxial substrate (for example, by a sublattice-symmetry breaking ionic potential [13, 105, 106]), we find that the Y-shaped Kekulé bond ordering by itself does not impose a mass on the Dirac fermions[1]. Instead, the valley degeneracy is broken by the helicity operator $\boldsymbol{p} \cdot \boldsymbol{\tau}$, which preserves the gapless Dirac point while locking the valley degree of freedom to the momentum. In a magnetic field the valley-momentum locking splits all Landau levels except for the zeroth Landau level, which remains pinned to zero energy.

5.2 Tight-binding model

5.2.1 Real-space formulation

A monolayer of carbon atoms has the tight-binding Hamiltonian

$$H = -\sum_{\boldsymbol{r}} \sum_{\ell=1}^{3} t_{\boldsymbol{r},\ell}\, a_{\boldsymbol{r}}^{\dagger} b_{\boldsymbol{r}+\boldsymbol{s}_\ell} + \text{H.c.}, \tag{5.1}$$

describing the hopping with amplitude $t_{\boldsymbol{r},\ell}$ between an atom at site $\boldsymbol{r} = n\boldsymbol{a}_1 + m\boldsymbol{a}_2$ $(n, m \in \mathbb{Z})$ on the A sublattice (annihilation operator $a_{\boldsymbol{r}}$)

[1] That the Kek-Y bond ordering by itself preserves the massless nature of the Dirac fermions in graphene could already have been deduced from Ref. [13] (it is a limiting case of their equation 4), although it was not noticed in the experimental Ref. [15]. We thank Dr. Gutiérrez for pointing this out to us.

and each of its three nearest neighbors at $\boldsymbol{r} + \boldsymbol{s}_\ell$ on the B sublattice (annihilation operator $b_{\boldsymbol{r}+\boldsymbol{s}_\ell}$). The lattice vectors are defined by $\boldsymbol{s}_1 = \frac{1}{2}(\sqrt{3}, -1)$, $\boldsymbol{s}_2 = -\frac{1}{2}(\sqrt{3}, 1)$, $\boldsymbol{s}_3 = (0, 1)$, $\boldsymbol{a}_1 = \boldsymbol{s}_3 - \boldsymbol{s}_1$, $\boldsymbol{a}_2 = \boldsymbol{s}_3 - \boldsymbol{s}_2$. All lengths are measured in units of the unperturbed C–C bond length $a_0 \equiv 1$.

For the uniform lattice, with $t_{\boldsymbol{r},\ell} \equiv t_0$, the band structure is given by [107]

$$E(\boldsymbol{k}) = \pm|\varepsilon(\boldsymbol{k})|, \quad \varepsilon(\boldsymbol{k}) = t_0 \textstyle\sum_{\ell=1}^{3} e^{i\boldsymbol{k}\cdot\boldsymbol{s}_\ell}. \tag{5.2}$$

There is a conical singularity at the Dirac points $\boldsymbol{K}_\pm = \frac{2}{9}\pi\sqrt{3}(\pm 1, \sqrt{3})$, where $E(\boldsymbol{K}_\pm) = 0$. For later use we note the identities

$$\varepsilon(\boldsymbol{k}) = \varepsilon(\boldsymbol{k} + 3\boldsymbol{K}_\pm) = e^{2\pi i/3}\varepsilon(\boldsymbol{k} + \boldsymbol{K}_+ + \boldsymbol{K}_-). \tag{5.3}$$

The bond-density wave that describes the Kek-O and Kek-Y textures has the form

$$t_{\boldsymbol{r},\ell}/t_0 = 1 + 2\,\mathrm{Re}\left[\Delta e^{i(p\boldsymbol{K}_+ + q\boldsymbol{K}_-)\cdot\boldsymbol{s}_\ell + i\boldsymbol{G}\cdot\boldsymbol{r}}\right] \tag{5.4a}$$

$$= 1 + 2\Delta_0 \cos[\phi + \tfrac{2}{3}\pi(m - n + N_\ell)], \tag{5.4b}$$

$$N_1 = -q, \quad N_2 = -p, \quad N_3 = p + q, \quad p, q \in \mathbb{Z}_3.$$

The Kekulé wave vector

$$\boldsymbol{G} \equiv \boldsymbol{K}_+ - \boldsymbol{K}_- = \tfrac{4}{9}\pi\sqrt{3}(1, 0) \tag{5.5}$$

couples the Dirac points. The coupling amplitude $\Delta = \Delta_0 e^{i\phi}$ may be complex, but the hopping amplitudes $t_{\boldsymbol{r},\ell}$ are real in order to preserve time-reversal symmetry.

As illustrated in Fig. 5.1, the index

$$\nu = 1 + q - p \mod 3 \tag{5.6}$$

distinguishes the Kek-O texture ($\nu = 0$) from the Kek-Y texture ($\nu = \pm 1$). Each Kekulé superlattice has a $2\pi/3$ rotational symmetry, reduced from the $2\pi/6$ symmetry of the graphene lattice. The two $\nu = \pm 1$ Kek-Y textures are each others mirror image [2].

[2] There are three sets of integers $p, q \in \mathbb{Z}_3$ for a given index $\nu = 1 + q - p \mod 3$, corresponding to textures on the honeycomb lattice that are translated by one hexagon, or equivalently related by a $\pm 2\pi/3$ phase shift of Δ.

5.2.2 Transformation to momentum space

The Kek-O and Kek-Y superlattices have the same hexagonal Brillouin zone, with reciprocal lattice vectors $\boldsymbol{K}_\pm$ — smaller by a factor $1/\sqrt{3}$ and rotated over 30° with respect to the original Brillouin zone of graphene (see Fig. 5.1). The Dirac points of unperturbed graphene are folded from the corner to the center of the Brillouin zone and coupled by the bond density wave.

To study the coupling we Fourier transform the tight-binding Hamilonian (5.1),

$$\begin{aligned} H(\boldsymbol{k}) = & -\varepsilon(\boldsymbol{k}) a^\dagger_{\boldsymbol{k}} b_{\boldsymbol{k}} - \Delta\varepsilon(\boldsymbol{k} + p\boldsymbol{K}_+ + q\boldsymbol{K}_-) a^\dagger_{\boldsymbol{k}+\boldsymbol{G}} b_{\boldsymbol{k}} \\ & - \Delta^*\varepsilon(\boldsymbol{k} - p\boldsymbol{K}_+ - q\boldsymbol{K}_-) a^\dagger_{\boldsymbol{k}-\boldsymbol{G}} b_{\boldsymbol{k}} + \text{H.c.} \end{aligned} \tag{5.7}$$

The momentum $\boldsymbol{k}$ still varies over the original Brillouin zone. In order to restrict it to the superlattice Brillouin zone we collect the annihilation operators at $\boldsymbol{k}$ and $\boldsymbol{k} \pm \boldsymbol{G}$ in the column vector

$$c_{\boldsymbol{k}} = (a_{\boldsymbol{k}}, a_{\boldsymbol{k}-\boldsymbol{G}}, a_{\boldsymbol{k}+\boldsymbol{G}}, b_{\boldsymbol{k}}, b_{\boldsymbol{k}-\boldsymbol{G}}, b_{\boldsymbol{k}+\boldsymbol{G}}) \tag{5.8}$$

and write the Hamiltonian in a 6×6 matrix form:

$$H(\boldsymbol{k}) = -c^\dagger_{\boldsymbol{k}} \begin{pmatrix} 0 & \mathcal{E}_\nu(\boldsymbol{k}) \\ \mathcal{E}^\dagger_\nu(\boldsymbol{k}) & 0 \end{pmatrix} c_{\boldsymbol{k}}, \tag{5.9a}$$

$$\mathcal{E}_\nu = \begin{pmatrix} \varepsilon_0 & \tilde\Delta\varepsilon_{\nu+1} & \tilde\Delta^*\varepsilon_{-\nu-1} \\ \tilde\Delta^*\varepsilon_{1-\nu} & \varepsilon_{-1} & \tilde\Delta\varepsilon_\nu \\ \tilde\Delta\varepsilon_{\nu-1} & \tilde\Delta^*\varepsilon_{-\nu} & \varepsilon_1 \end{pmatrix}, \tag{5.9b}$$

$$\tilde\Delta = e^{2\pi i(p+q)/3}\Delta, \quad \varepsilon_n = \varepsilon(\boldsymbol{k} + n\boldsymbol{G}), \tag{5.9c}$$

where we used Eq. (5.3).

5.3 Low-energy Hamiltonian

5.3.1 Gapless spectrum

The low-energy spectrum is governed by the four modes

$$u_{\boldsymbol{k}} = (a_{\boldsymbol{k}-\boldsymbol{G}}, a_{\boldsymbol{k}+\boldsymbol{G}}, b_{\boldsymbol{k}-\boldsymbol{G}}, b_{\boldsymbol{k}+\boldsymbol{G}}), \tag{5.10}$$

which for small $\boldsymbol{k}$ lie near the Dirac points at $\pm\boldsymbol{G}$. (We identify the K valley with $+\boldsymbol{G}$ and the K' valley with $-\boldsymbol{G}$.) Projection onto this

subspace reduces the six-band Hamiltonian (5.9) to an effective four-band Hamiltonian,

$$H_{\text{eff}} = -u_{\boldsymbol{k}}^{\dagger} \begin{pmatrix} 0 & h_\nu \\ h_\nu^{\dagger} & 0 \end{pmatrix} u_{\boldsymbol{k}}, \quad h_\nu = \begin{pmatrix} \varepsilon_{-1} & \tilde{\Delta}\varepsilon_\nu \\ \tilde{\Delta}^* \varepsilon_{-\nu} & \varepsilon_1 \end{pmatrix}. \tag{5.11}$$

Corrections to the low-energy spectrum from virtual transitions to the higher bands are of order Δ_0^2. We will include these corrections later, but for now assume $\Delta_0 \ll 1$ and neglect them.

The $\boldsymbol{k}$-dependence of ε_n may be linearized near $\boldsymbol{k} = 0$,

$$\varepsilon_0 = 3t_0, \quad \varepsilon_{\pm 1} = \hbar v_0(\mp k_x + i k_y) + \text{order}\,(k^2), \tag{5.12}$$

with Fermi velocity $v_0 = \frac{3}{2} t_0 a_0/\hbar$. The corresponding 4-component Dirac equation has the form

$$\mathcal{H} \begin{pmatrix} \Psi_{K'} \\ \Psi_K \end{pmatrix} = E \begin{pmatrix} \Psi_{K'} \\ \Psi_K \end{pmatrix}, \quad \mathcal{H} = \begin{pmatrix} v_0 \boldsymbol{p}\cdot\boldsymbol{\sigma} & \tilde{\Delta} Q_\nu \\ \tilde{\Delta}^* Q_\nu^{\dagger} & v_0 \boldsymbol{p}\cdot\boldsymbol{\sigma} \end{pmatrix}, \tag{5.13a}$$

$$\Psi_{K'} = \begin{pmatrix} -\psi_{B,K'} \\ \psi_{A,K'} \end{pmatrix}, \quad \Psi_K = \begin{pmatrix} \psi_{A,K} \\ \psi_{B,K} \end{pmatrix}, \tag{5.13b}$$

$$Q_\nu = \begin{pmatrix} \varepsilon_{-\nu}^* & 0 \\ 0 & -\varepsilon_\nu \end{pmatrix} = \begin{cases} 3t_0 \sigma_z & \text{if } \nu = 0, \\ v_0(\nu p_x - i p_y)\sigma_0 & \text{if } |\nu| = 1. \end{cases} \tag{5.13c}$$

The spinor Ψ_K contains the wave amplitudes on the A and B sublattices in valley K and similarly $\Psi_{K'}$ for valley K', but note the different ordering of the components[3]. We have defined the momentum operator $\boldsymbol{p} = -i\hbar\partial/\partial\boldsymbol{r}$, with $\boldsymbol{p}\cdot\boldsymbol{\sigma} = p_x\sigma_x + p_y\sigma_y$. The Pauli matrices $\sigma_x, \sigma_y, \sigma_z$, with σ_0 the unit matrix, act on the sublattice degree of freedom.

For the Kek-O texture we recover the gapped spectrum of Kekulé dimerized graphene [102],

$$E^2 = v_0^2 |\boldsymbol{p}|^2 + (3t_0\Delta_0)^2 \quad \text{for} \quad \nu = 0. \tag{5.14}$$

The Kek-Y texture, instead, has a gapless spectrum,

$$E_\pm^2 = v_0^2 (1 \pm \Delta_0)^2 |\boldsymbol{p}|^2, \quad \text{for} \quad |\nu| = 1, \tag{5.15}$$

consisting of a pair of linearly dispersing modes with different velocities $v_0(1 \pm \Delta_0)$. The two qualitatively different dispersions are contrasted in Fig. 5.2.

[3] The ordering of the spinor components in Eq. (5.13b) is the socalled valley-isotropic representation of Dirac fermions, see [108].

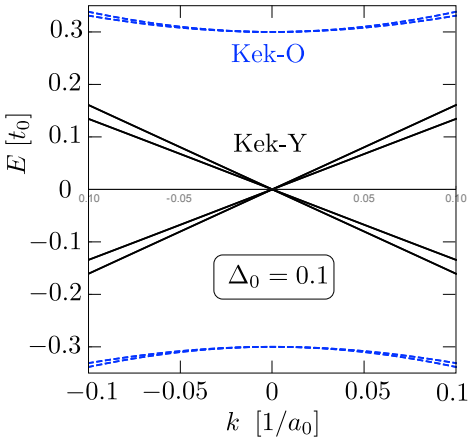

Figure 5.2. Dispersion relation near the center of the superlattice Brillouin zone, for the Kek-O texture (blue dashed curves) and for the Kek-Y texture (black solid). The curves are calculated from the full Hamiltonian (5.9) for $|\tilde{\Delta}| = \Delta_0 = 0.1$.

5.3.2 Valley-momentum locking

The two gapless modes in the Kek-Y superlattice are helical, with both the sublattice pseudospin and the valley isospin locked to the direction of motion. To see this, we consider the $\nu = 1$ Kek-Y texture with a real $\tilde{\Delta} = \Delta_0$. (Complex $\tilde{\Delta}$ and $\nu = -1$ are equivalent upon a unitary transformation.) The Dirac Hamiltonian (5.13) can be written in the compact form

$$\mathcal{H} = v_\sigma\,(\boldsymbol{p}\cdot\boldsymbol{\sigma})\otimes\tau_0 + v_\tau\,\sigma_0\otimes(\boldsymbol{p}\cdot\boldsymbol{\tau}), \tag{5.16}$$

with the help of a second set of Pauli matrices τ_x, τ_y, τ_z and unit matrix τ_0 acting on the valley degree of freedom. The two velocities are defined by $v_\sigma = v_0$ and $v_\tau = v_0\Delta_0$.

An eigenstate of the current operator

$$j_\alpha = \partial\mathcal{H}/\partial p_\alpha = v_\sigma\,\sigma_\alpha\otimes\tau_0 + v_\tau\,\sigma_0\otimes\tau_\alpha \tag{5.17}$$

with eigenvalue $v_\sigma \pm v_\tau$ is an eigenstate of σ_α with eigenvalue $+1$ and an eigenstate of τ_α with eigenvalue ± 1. (The two Pauli matrices act on different degrees of freedom, so they commute and can be diagonalized independently.) This valley-momentum locking does not violate time-reversal symmetry, since the time-reversal operation in the superlattice

inverts all three vectors $\boldsymbol{p}$, $\boldsymbol{\sigma}$, and $\boldsymbol{\tau}$, and hence leaves $\mathcal{H}$ unaffected[4]:

$$(\sigma_y \otimes \tau_y)\mathcal{H}^*(\sigma_y \otimes \tau_y) = \mathcal{H}. \tag{5.18}$$

The valley-momentum locking does break the sublattice symmetry, since $\mathcal{H}$ no longer anticommutes with σ_z, but another chiral symmetry involving both sublattice and valley degrees of freedom remains:

$$(\sigma_z \otimes \tau_z)\mathcal{H} = -\mathcal{H}(\sigma_z \otimes \tau_z). \tag{5.19}$$

5.3.3 Landau level quantization

A perpendicular magnetic field B in the z-direction (vector potential $\boldsymbol{A}$ in the x–y plane), breaks the time-reversal symmetry (5.18) via the substitution $\boldsymbol{p} \mapsto -i\hbar\partial/\partial\boldsymbol{r} + e\boldsymbol{A}(\boldsymbol{r}) \equiv \boldsymbol{\Pi}$. The chiral symmetry (5.19) is preserved, so the Landau levels are still symmetrically arranged around $E = 0$, as in unperturbed graphene. Because the two helicity operators $\boldsymbol{\Pi}\cdot\boldsymbol{\sigma}$ and $\boldsymbol{\Pi}\cdot\boldsymbol{\tau}$ do not commute for $\boldsymbol{A} \neq 0$, they can no longer be diagonalized independently. In particular, this means the Landau level spectrum is not simply a superposition of two spectra of Dirac fermions with different velocities.

It is still possible to calculate the spectrum analytically (see Sec. 5.7.1). We find Landau levels at energies $E_n^+, E_n^-, -E_n^+, -E_n^-$, $n = 0, 1, 2, \ldots$, given by

$$E_n^\pm = E_B \left[2n + 1 \pm \sqrt{1 + n(n+1)(4v_\sigma v_\tau)^2 \bar{v}^{-4}}\right]^{1/2}, \tag{5.20}$$

with the definitions $\bar{v} = \sqrt{v_\sigma^2 + v_\tau^2}$ and $E_B = \bar{v}\sqrt{\hbar e B}$.

In unperturbed graphene all Landau levels have a twofold valley degeneracy[5]: $E_n^+ = E_{n+1}^-$ for $v_\tau = 0$. This includes the zeroth Landau level: $E_0^- = 0 = -E_0^-$. A nonzero v_τ breaks the valley degeneracy of all Landau levels at $E \neq 0$, but a valley-degenerate zero-mode $E_0^- = 0$ remains, see Fig. 5.3.

[4] The time-reversal operation $\mathcal{T} = (\sigma_y \otimes \tau_y)\mathcal{C}$ from Eq. (5.18) (with $\mathcal{C}$ complex conjugation) squares to $+1$ because the electron spin is not explicitly included. If we do include it, we would have $\mathcal{T} = (s_y \otimes \sigma_y \otimes \tau_y)\mathcal{C}$, which squares to -1 as expected for a fermionic quasiparticle. The combination of the time-reversal symmetry (5.18) and the chiral symmetry (5.19) places the superlattice in the BDI symmetry classification of topological states of matter.

[5] The Landau levels also have a twofold spin degeneracy, which could be resolved by the Zeeman energy but is not considered here.

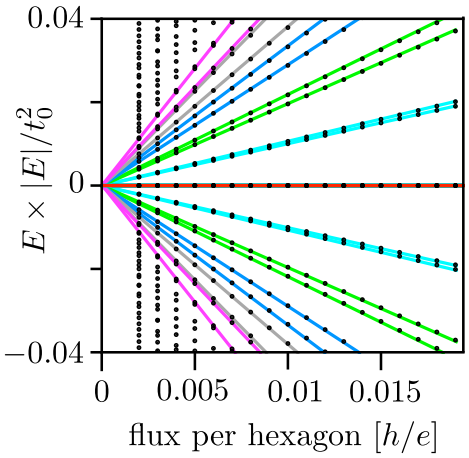

Figure 5.3. Landau levels in the Kek-Y superlattice ($\Delta_0 = 0.1$, $\phi = 0$, $\nu = 1$). The data points are calculated numerically [16] from the tight-binding Hamiltonian (5.1) with bond modulation (5.4). The lines are the analytical result from Eqs. (5.20) and (5.21) for the first few Landau levels. Lines of the same color identify the valley-split Landau level, the zeroth Landau level (red line) is not split.

The absence of a splitting of the zeroth-Landau level can be understood as a topological protection in the context of an index theorem [109–112], which requires that *either* $\Pi_+ \equiv \Pi_x + i\Pi_y$ or $\Pi_- \equiv \Pi_x - i\Pi_y$ has a zero-mode. If we decompose $\mathcal{H} = \Pi_+ S_- + \Pi_- S_+$, with $S_\pm = v_\sigma(\sigma_x \pm i\sigma_y) + v_\tau(\tau_x \pm i\tau_y)$, we see that *both* S_+ and S_- have a rank-two null space[6], spanned by the spinors $\psi_\pm^{(1)}$ and $\psi_\pm^{(2)}$. So if $\Pi_\pm f_\pm = 0$, a twofold degenerate zero-mode of $\mathcal{H}$ is formed by the states $f_\pm \psi_\mp^{(1)}$ and $f_\pm \psi_\mp^{(2)}$.

All of this is distinctive for the Kek-Y bond order: for the Kek-O texture it's the other way around — the Landau levels have a twofold valley degeneracy except for the nondegenerate Landau level at the edge of the band gap[7].

[6] If we define the eigenstates $|\alpha, \beta\rangle$ by $\sigma_z|\alpha,\beta\rangle = \alpha|\alpha,\beta\rangle$, $\tau_z|\alpha,\beta\rangle = \beta|\alpha,\beta\rangle$, then S_+ annihilates $\psi_+^{(1)} = |1,1\rangle$ and $\psi_+^{(2)} = v_\tau|-1,1\rangle - v_\sigma|1,-1\rangle$, while S_- annihilates $\psi_-^{(1)} = |-1,-1\rangle$ and $\psi_-^{(2)} = v_\tau|1,-1\rangle - v_\sigma|-1,1\rangle$.

[7] In a Kek-O superlattice the Landau levels are given by $E_n^2 = (3t_0\Delta_0)^2 + 2n\hbar eBv_0^2$, $n = 0, 1, 2, \ldots$, with a twofold valley degeneracy for $n \geq 1$ and a nondegenerate zeroth Landau level at $\pm 3t_0\Delta_0$.

5.4 Effect of virtual transitions to higher bands

So far we have assumed $\Delta_0 \ll 1$, and one might ask how robust our findings are to finite-Δ_0 corrections, involving virtual transitions from the $\varepsilon_{\pm 1}$ bands near $E = 0$ to the ε_0 band near $E = 3t_0$. We have been able to include these to all orders in Δ_0 (see Sec. 5.7.2), and find that the entire effect is a renormalization of the velocities v_σ and v_τ in the Hamiltonian (5.16), which retains its form as a sum of two helicity operators. For real $\Delta = \Delta_0$ the renormalization is given by $v_\sigma = v_0\rho_+$, $v_\tau = v_0\rho_-$ with

$$\rho_\pm = \tfrac{1}{2}(1 - \Delta_0)\left(\frac{1 + 2\Delta_0}{\sqrt{1 + 2\Delta_0^2}} \pm 1\right). \tag{5.21}$$

For complex $\Delta = \Delta_0 e^{i\phi}$ the nonlinear renormalization introduces a dependence on the phase ϕ modulo $2\pi/3$.

What this renormalization shows is that, as expected for a topological protection, the robustness of the zeroth Landau level to the Kek-Y texture is not limited to perturbation theory — also strong modulations of the bond strength cannot split it away from $E = 0$.

5.5 Pseudospin-valley coupling

In zero magnetic field the low-energy Hamiltonian (5.16) does not couple the pseudospin σ and valley τ degrees of freedom. A $\boldsymbol{\sigma} \otimes \boldsymbol{\tau}$ coupling is introduced in the Kek-Y superlattice by an ionic potential $\mu_{\rm Y}$ on the carbon atoms that line up with the carbon vacancies — the atoms located at each center of a red Y in Fig. 5.1. We consider this effect for the $\nu = 1$ Kek-Y texture with a real $\tilde{\Delta} = \Delta_0$.

The ionic potential acts on one-third of the A sublattice sites, labeled $\boldsymbol{r}_{\rm Y}$. (For $\nu = -1$ it would act on one-third of the B sublattice sites.) Fourier transformation of the on-site contribution $\mu_{\rm Y} \sum_{\boldsymbol{r}_{\rm Y}} a^\dagger_{\boldsymbol{r}_{\rm Y}} a_{\boldsymbol{r}_{\rm Y}}$ to the tight-binding Hamiltonian (5.1) gives with the help of the lattice sum

$$\textstyle\sum_{\boldsymbol{r}_{\rm Y}} e^{i\boldsymbol{k}\cdot\boldsymbol{r}_{\rm Y}} \propto \delta(\boldsymbol{k}) + \delta(\boldsymbol{k} - \boldsymbol{G}) + \delta(\boldsymbol{k} + \boldsymbol{G}) \tag{5.22}$$

the momentum-space Hamiltonian

$$H(\boldsymbol{k}) = -c_{\boldsymbol{k}}^{\dagger} \begin{pmatrix} M_{\mathrm{Y}} & \mathcal{E}_1(\boldsymbol{k}) \\ \mathcal{E}_1^{\dagger}(\boldsymbol{k}) & 0 \end{pmatrix} c_{\boldsymbol{k}}, \tag{5.23a}$$

$$M_{\mathrm{Y}} = -\mu_{\mathrm{Y}} \begin{pmatrix} 1 & 1 & 1 \\ 1 & 1 & 1 \\ 1 & 1 & 1 \end{pmatrix}. \tag{5.23b}$$

The $\mathcal{E}_1$ block is still given by Eq. (5.9). The additional M_{Y}-block breaks the chiral symmetry.

Projection onto the subspace spanned by low-energy modes (Eq. 5.10) gives the effective Hamiltonian

$$H_{\mathrm{eff}} = -u_{\boldsymbol{k}}^{\dagger} \begin{pmatrix} m_{\mathrm{Y}} & h_1 \\ h_1^{\dagger} & 0 \end{pmatrix} u_{\boldsymbol{k}}, \quad m_{\mathrm{Y}} = -\mu_{\mathrm{Y}} \begin{pmatrix} 1 & 1 \\ 1 & 1 \end{pmatrix}. \tag{5.24}$$

The corresponding Dirac Hamiltonian has the form (5.13) with an additional $\boldsymbol{\sigma} \otimes \boldsymbol{\tau}$ coupling,

$$\begin{aligned} \mathcal{H} = v_\sigma\, (\boldsymbol{p} \cdot \boldsymbol{\sigma}) \otimes \tau_0 + v_\tau\, \sigma_0 \otimes (\boldsymbol{p} \cdot \boldsymbol{\tau}) + \tfrac{1}{2}\mu_{\mathrm{Y}} \\ + \tfrac{1}{2}\mu_{\mathrm{Y}}(\sigma_x \otimes \tau_x + \sigma_y \otimes \tau_y - \sigma_z \otimes \tau_z). \end{aligned} \tag{5.25}$$

The energy spectrum,

$$\begin{aligned} E_{\pm}^{(1)} &= \pm(v_\sigma - v_\tau)|\boldsymbol{p}|, \\ E_{\pm}^{(2)} &= \mu_{\mathrm{Y}} \pm \sqrt{(v_\sigma + v_\tau)^2 |\boldsymbol{p}|^2 + \mu_{\mathrm{Y}}^2}, \end{aligned} \tag{5.26}$$

has two bands that cross linearly in p at $E = 0$, while the other two bands have a quadratic p-dependence. (See Fig. 5.4.)

The three bands $E_{+}^{(1)}$, $E_{-}^{(1)}$, $E_{-}^{(2)}$ that intersect at $p = 0$ are reminiscent of a spin-one Dirac one. Such a dispersion is a known feature of a potential modulation that involves only one-third of the atoms on one sublattice [13, 106]. The spectrum remains gapless even though the chiral symmetry is broken. This is in contrast to the usual staggered potential between A and B sublattices, which opens a gap via a $\sigma_z \otimes \tau_z$ term [107].

5.6 Discussion

In summary, we have shown that the Y-shaped Kekulé bond texture (Kek-Y superlattice) in graphene preserves the massless character of the Dirac

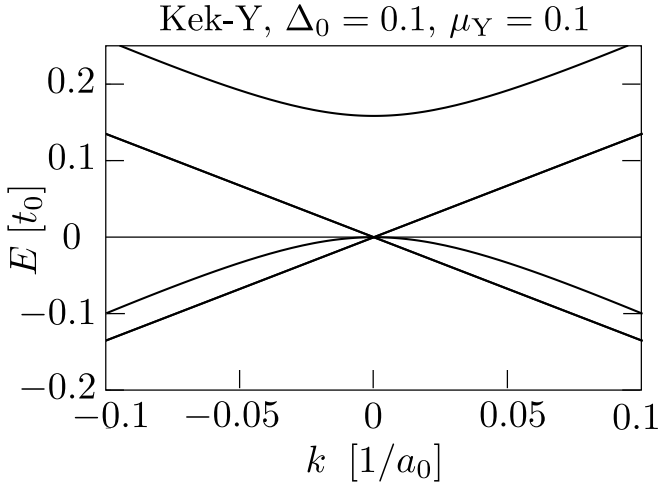

Figure 5.4. Effect of an on-site potential μ_Y on the Kek-Y bandstructure of Fig. 5.2. The three bands that intersect linearly and quadratically at the center of the superlattice Brillouin zone form the "spin-one Dirac cone" of Refs. [106] and [13]. The curves are calculated from the full Hamiltonian (5.23) for $\Delta_0 = 0.1 = \mu_Y$.

fermions. This is fundamentally different from the gapped band structure resulting from the original Kekulé dimerization [27, 28, 102, 103] (Kek-O superlattice), and contrary to expectations from its experimental realization [15, 101].

The gapless low-energy Hamiltonian $\mathcal{H} = v_\sigma \boldsymbol{p} \cdot \boldsymbol{\sigma} + v_\tau \boldsymbol{p} \cdot \boldsymbol{\tau}$ is the sum of two helicity operators, with the momentum $\boldsymbol{p}$ coupled independently to both the sublattice pseudospin $\boldsymbol{\sigma}$ and the valley isospin $\boldsymbol{\tau}$. This valley-momentum locking is distinct from the coupling of the valley to a pseudomagnetic field that has been explored as an enabler for valleytronics [113], and offers a way for a momentum-controlled valley precession. The broken valley degeneracy would also remove a major obstacle for spin qubits in graphene [114].

A key experimental test of our theoretical predictions would be a confirmation that the Kek-Y superlattice has a gapless spectrum, in stark contrast to the gapped Kek-O spectrum. In the experiment by Gutiérrez *et al.* on a graphene/Cu heterostructure the Kek-Y superlattice is formed by copper vacancies that are in registry with one out of six carbon atoms [15, 101]. These introduce the Y-shaped hopping modulations shown in Fig. 5.1, but in addition will modify the ionic potential felt by

the carbon atom at the center of the Y. Unlike the usual staggered potential between A and B sublattices, this potential modulation in an enlarged unit cell does not open a gap [13, 106]. We have also checked that the Dirac cone remains gapless if we include hoppings beyond nearest neigbor. All of this gives confidence that the gapless spectrum will survive in a realistic situation.

Further research in other directions could involve the Landau level spectrum, to search for the unique feature of a broken valley degeneracy coexisting with a valley-degenerate zero-mode. The graphene analogues in optics and acoustics [115] could also provide an interesting platform for a Kek-Y superlattice with a much stronger amplitude modulation than can be realized with electrons.

5.7 Appendix

5.7.1 Calculation of the Landau level spectrum in a Kek-Y superlattice

We calculate the spectrum in a perpendicular magnetic field of a graphene sheet with a Kekulé-Y bond texture. We start by rewriting the Hamiltonian (5.16), with $\boldsymbol{\Pi} = \boldsymbol{p} + e\boldsymbol{A}$, in the form

$$\mathcal{H} = \tfrac{1}{2}\Pi_+ S_- + \tfrac{1}{2}\Pi_- S_+ + \mu\sigma_z \otimes \tau_z, \tag{5.27}$$

in terms of the raising and lowering operators

$$\begin{aligned} &\Pi_\pm = \Pi_x \pm i\Pi_y, \;\; \sigma_\pm = \sigma_x \pm i\sigma_y, \;\; \tau_\pm = \tau_x \pm i\tau_y, \\ &S_\pm = v_\sigma\, \sigma_\pm \otimes \tau_0 + v_\tau\, \sigma_0 \otimes \tau_\pm. \end{aligned} \tag{5.28}$$

The chiral-symmetry breaking term $\mu\sigma_z \otimes \tau_z$ that we have added will serve a purpose later on.

We know that the Hermitian operator $\Omega = \Pi_+\Pi_-$ has eigenvalues $\omega_n = 2n\hbar eB$, $n = 0, 1, 2, \ldots$, in view of the commutator $[\Pi_-, \Pi_+] = 2\hbar eB$. So the strategy is to express the secular equation $\det(E - \mathcal{H}) = 0$ in a form that involves only the mixed products $\Pi_+\Pi_-$, and no Π_+^2 or Π_-^2. This is achieved by means of a unitary transformation, as follows.

We define the unitary matrix

$$U = \exp[\tfrac{1}{4}i\pi(\sigma_0 + \sigma_z) \otimes \tau_y] \tag{5.29}$$

and reduce the determinant of a 4×4 matrix to that of a 2×2 matrix:

$$\begin{aligned}\det(\mathcal{H}-E) &= \det U^\dagger(\mathcal{H}-E)U \\ &= \det\begin{pmatrix} -E+\mu & R^\dagger \\ R & -E-\mu \end{pmatrix} \\ &= \begin{cases} \det(E^2-\mu^2-RR^\dagger) & \text{if } E \neq \mu, \\ \det(E^2-\mu^2-R^\dagger R) & \text{if } E \neq -\mu, \end{cases} \end{aligned} \tag{5.30}$$

$$\text{with } R = \begin{pmatrix} -v_\tau \Pi_- & v_\sigma \Pi_- \\ -v_\sigma \Pi_+ & v_\tau \Pi_+ \end{pmatrix}. \tag{5.31}$$

The matrix product $RR^\dagger$ is not of the desired form, but $R^\dagger R$ is,

$$R^\dagger R = \begin{pmatrix} v_\sigma^2 \Pi_- \Pi_+ + v_\tau^2 \Pi_+ \Pi_- & -v_\sigma v_\tau(\Pi_-\Pi_+ + \Pi_+\Pi_-) \\ -v_\sigma v_\tau(\Pi_-\Pi_+ + \Pi_+\Pi_-) & v_\sigma^2 \Pi_+\Pi_- + v_\tau^2 \Pi_-\Pi_+ \end{pmatrix}, \tag{5.32}$$

involving only $\Pi_+\Pi_- = \Omega$ and $\Pi_-\Pi_+ = \Omega + \omega_1$. Hence the determinant is readily evaluated for $E \neq -\mu$,

$$\begin{aligned}&\det(\mathcal{H}-E) = \det(E^2-\mu^2-R^\dagger R) \\ &= \prod_{n=0}^{\infty} \det\begin{pmatrix} E^2-\mu^2-\bar{v}^2\omega_n - v_\sigma^2\omega_1 & v_\sigma v_\tau(2\omega_n+\omega_1) \\ v_\sigma v_\tau(2\omega_n+\omega_1) & E^2-\mu^2-\bar{v}^2\omega_n - v_\tau^2\omega_1 \end{pmatrix}, \end{aligned} \tag{5.33}$$

where we have abbreviated $\bar{v} = \sqrt{v_\sigma^2 + v_\tau^2}$.

Equating the determinant to zero and solving for E we find four sets of energy eigenvalues $E_n^+, E_n^-, -E_n^+, -E_n^-$, given by

$$\begin{aligned}(E_n^\pm)^2 - \mu^2 &= (\omega_n + \tfrac{1}{2}\omega_1)\bar{v}^2 \pm \tfrac{1}{2}\sqrt{\omega_1^2\bar{v}^4 + (4v_\sigma v_\tau)^2 \omega_n \omega_{n+1}} \\ &= E_B^2\left[2n+1 \pm \sqrt{1+n(n+1)(4v_\sigma v_\tau)^2\bar{v}^{-4}}\right]. \end{aligned} \tag{5.34}$$

In the second equation we introduced the energy scale $E_B = \hbar\bar{v}/l_m$, with $l_m = \sqrt{\hbar/eB}$ the magnetic length. The B-independent level $E_0^- = \mu$ becomes a zero-mode in the limit $\mu \to 0$.

As a check on the calculation, we note that for $\mu = 0$, $v_\tau = 0$ we recover the valley-degenerate Landau level spectrum of graphene [107],

$$E_n^- = (\hbar v_\sigma/l_m)\sqrt{2n}, \quad E_n^+ = E_{n+1}^-. \tag{5.35}$$

Another special case of interest is $\mu = 0$, $v_\sigma = v_\tau \equiv v_0$, when the two modes of Dirac fermions have velocities $v_\sigma \pm v_\tau$ equal to 0 and $2v_0$. From Eq. (5.34) we find the Landau level spectrum

$$E_n^- = 0, \quad E_n^+ = 2(\hbar v_0/l_m)\sqrt{2n+1}. \tag{5.36}$$

The mode with zero velocity remains B-independent, while the mode with velocity $2v_0$ produces a sequence of Landau levels with a 1/2 offset in the n-dependence.

5.7.2 Calculation of the low-energy Hamiltonian to all orders in the Kek-Y bond modulation

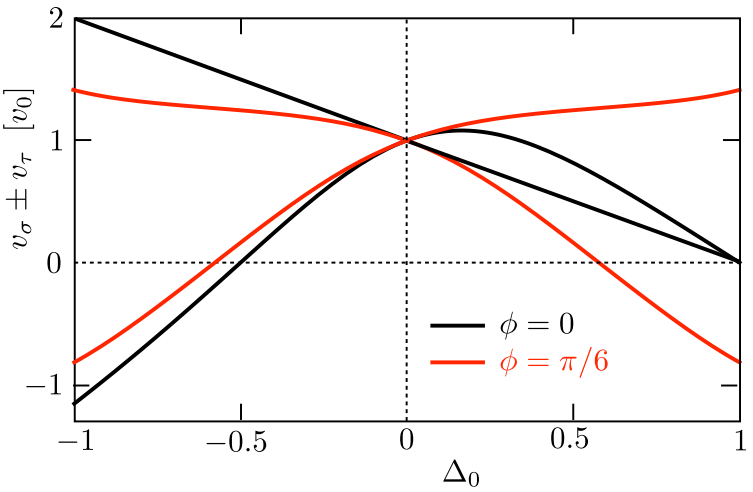

Figure 5.5. Velocities $v_1 = v_\sigma + v_\tau$ and $v_2 = v_\sigma - v_\tau$ of the two gapless modes in the Kek-Y superlattice, as a function of the bond modulation amplitude Δ_0 for two values of the modulation phase ϕ. The ϕ-dependence modulo $2\pi/3$ appears to second order in Δ_0. The curves are calculated from Eq. (5.43). Note that positive and negative values of v_1, v_2 are equivalent.

We seek to reduce the six-band Hamiltonian (5.9) to an effective 4×4 Hamiltonian that describes the low-energy spectrum near $\boldsymbol{k} = 0$. For $\Delta_0 \ll 1$ we can simply project onto the 2×2 lower-right subblock of $\mathcal{E}_\nu$, which for the $|\nu| = 1$ Kek-Y bond modulation vanishes linearly in $\boldsymbol{k}$. This subblock is coupled to the ε_0 band near $E = 3t_0$ by matrix elements of order Δ_0, so virtual transitions to this higher band contribute to the

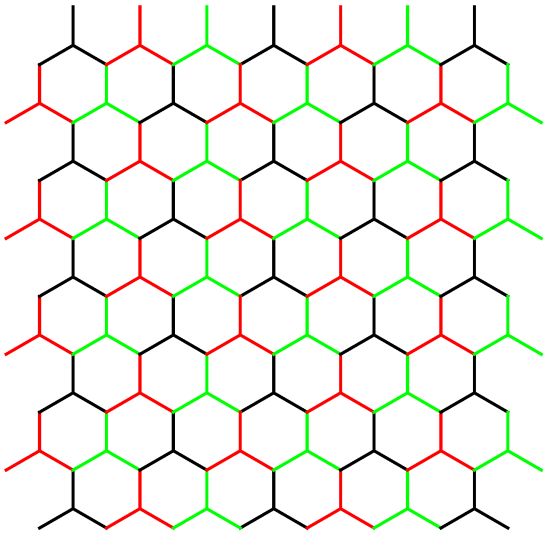

Figure 5.6. Kek-Y superlattice with a complex bond amplitude $\Delta = e^{i\phi}\Delta_0$, according to Eq. (5.4) with $\nu = 1$. The three colors of the bonds refer to three different bond strengths, adding up to $3t_0$. For $\phi = 0$ two of the bond strengths are equal to $t_0(1-\Delta_0)$ and the third equals $t_0(1+2\Delta_0)$. This is the case shown in Fig. 5.1. For $\phi = \pi/6$ the bond strengths are equidistant: $t_0(1-\Delta_0\sqrt{3})$, t_0, and $t_0(1+\Delta_0\sqrt{3})$. The value of Δ_0 where a bond strength vanishes shows up in Fig. 5.5 as a point of vanishing velocity.

low-energy spectrum in order Δ_0^2. We will now show how to include these effects to all order in Δ_0.

One complication when we go beyond the small-Δ_0 regime is that the phase ϕ of the modulation amplitude can no longer be removed by a unitary transformation. As we will see, the low-energy Hamiltonian depends on ϕ modulo $2\pi/3$ — so we don't need to distinguish between the phase of $\tilde{\Delta} = e^{2\pi i(p+q)/3}\Delta$ and the phase of Δ. The choice between $\nu = \pm 1$ still does not matter, the two Kek-Y modulations being related by a mirror symmetry. For definiteness we take $\nu = +1$.

We define the unitary matrix

$$V = \begin{pmatrix} \Phi & 0 \\ 0 & \Phi \end{pmatrix} \begin{pmatrix} \mathcal{V} & 0 \\ 0 & \mathbb{1} \end{pmatrix}, \quad \Phi = \begin{pmatrix} 1 & 0 & 0 \\ 0 & e^{-i\phi} & 0 \\ 0 & 0 & e^{i\phi} \end{pmatrix}, \tag{5.37a}$$

$$\mathcal{V} = \frac{1}{2D_0} \begin{pmatrix} 2 & -2\Delta_0 & -2\Delta_0 \\ 2\Delta_0 & 1+D_0 & 1-D_0 \\ 2\Delta_0 & 1-D_0 & 1+D_0 \end{pmatrix}, \tag{5.37b}$$

with $D_0 = \sqrt{1+2\Delta_0^2}$ and evaluate

$$V^\dagger \begin{pmatrix} 0 & \mathcal{E}_1 \\ \mathcal{E}_1^\dagger & 0 \end{pmatrix} V = \begin{pmatrix} 0 & \tilde{\mathcal{E}}_1 \\ \tilde{\mathcal{E}}_1^\dagger & 0 \end{pmatrix}, \tag{5.38a}$$

$$\tilde{\mathcal{E}}_1 = \mathcal{V}^\dagger \mathcal{E}_1 = \begin{pmatrix} D_0\varepsilon_0 & \rho_0^*\varepsilon_{-1} & \rho_0\varepsilon_1 \\ 0 & \rho_+\varepsilon_{-1} & \rho_-^*\varepsilon_1 \\ 0 & \rho_-\varepsilon_{-1} & \rho_+^*\varepsilon_1 \end{pmatrix}, \tag{5.38b}$$

$$\rho_\pm = \frac{1}{2D_0}\left[1 - 2\Delta_0^2 \pm D_0 + e^{-3i\phi}\Delta_0(1 \mp D_0)\right], \tag{5.38c}$$

$$\rho_0 = \frac{\Delta_0}{D_0}(2 + e^{3i\phi}\Delta_0). \tag{5.38d}$$

The matrix elements that couple the lower-right 2×2 subblock of $\tilde{\mathcal{E}}_1$ to ε_0 are now of order k, so the effect on the low-energy spectrum is of order k^2 and can be neglected — *to all orders in* Δ_0.

The resulting effective low-energy Hamiltonian has the 4×4 form (5.11), with h_1 replaced by

$$h_1 = \begin{pmatrix} \rho_+\varepsilon_{-1} & \rho_-^*\varepsilon_1 \\ \rho_-\varepsilon_{-1} & \rho_+^*\varepsilon_1 \end{pmatrix}. \tag{5.39}$$

The phases of $\rho_\pm = |\rho_\pm| e^{i\theta_\pm}$ can be eliminated by one more unitary transformation, with the 4×4 diagonal matrix

$$\Theta = \mathrm{diag}\,(e^{i\theta_-}, e^{i\theta_+}, e^{i\theta_+ + i\theta_-}, 1), \tag{5.40}$$

which results in

$$\Theta^\dagger \begin{pmatrix} 0 & h_1 \\ \tilde{h}_1^\dagger & 0 \end{pmatrix} \Theta = \begin{pmatrix} 0 & \tilde{h}_1 \\ \tilde{h}_1^\dagger & 0 \end{pmatrix}, \quad \tilde{h}_1 = \begin{pmatrix} |\rho_+|\varepsilon_{-1} & |\rho_-|\varepsilon_1 \\ |\rho_-|\varepsilon_{-1} & |\rho_+|\varepsilon_1 \end{pmatrix}. \tag{5.41}$$

Finally, we arrive at the effective Hamiltonian (5.16), with renormalized velocities:

$$\mathcal{H} = v_\sigma\,(\boldsymbol{p}\cdot\boldsymbol{\sigma})\otimes\tau_0 + v_\tau\,\sigma_0\otimes(\boldsymbol{p}\cdot\boldsymbol{\tau}),\quad v_\sigma = |\rho_+|v_0,\quad v_\tau = |\rho_-|v_0, \tag{5.42}$$

$$|\rho_\pm|^2 = \frac{1}{2D_0^2}\Big(1 + 3\Delta_0^4 \pm D_0(1-3\Delta_0^2) + 2\Delta_0^3(\pm D_0 - 2)\cos 3\phi\Big). \tag{5.43}$$

To third order in Δ_0 we have

$$\begin{aligned} v_\sigma/v_0 &= 1 - \tfrac{3}{2}\Delta_0^2 - \tfrac{1}{2}\Delta_0^3\cos 3\phi,\\ v_\tau/v_0 &= \Delta_0 - \tfrac{3}{2}\Delta_0^2\cos 3\phi + \tfrac{1}{16}\Delta_0^3(1 - 9\cos 6\phi) + \mathcal{O}(\Delta_0^4). \end{aligned} \tag{5.44}$$

For real Δ, when $\phi = 0$ and $\rho_\pm$ is real, Eq. (5.43) simplifies to

$$\rho_\pm = \tfrac{1}{2}(1-\Delta_0)\left(\frac{1+2\Delta_0}{\sqrt{1+2\Delta_0^2}} \pm 1\right). \tag{5.45}$$

The velocities of the two Dirac modes are then given by

$$\begin{aligned} v_1 &= v_\sigma + v_\tau = v_0\frac{(1-\Delta_0)(1+2\Delta_0)}{\sqrt{1+2\Delta_0^2}}\\ v_2 &= v_\sigma - v_\tau = v_0(1-\Delta_0). \end{aligned} \tag{5.46}$$

More generally, for complex $\Delta = \Delta_0 e^{i\phi}$ both v_1 and v_2 become ϕ-dependent to second order in Δ_0, see Fig. 5.5.

Note that the asymmetry in $\pm\Delta_0$ vanishes for $\phi = \pi/6$. For this phase the superlattice has three different bond strengths (see Fig. 5.6) that are symmetrically arranged around the unperturbed value t_0.

Bibliography

[1] D. Drung, C. Abmann, J. Beyer, A. Kirste, M. Peters, F. Ruede, and T. Schurig. *Highly sensitive and easy-to-use SQUID sensors.* IEEE Transactions on Applied Superconductivity **17**, 699–704 (2007).

[2] P. Joyez, P. Lafarge, A. Filipe, D. Esteve, and M. H. Devoret. *Observation of parity-induced suppression of Josephson tunneling in the superconducting single electron transistor.* Phys. Rev. Lett. **72**, 2458–2461 (1994).

[3] I. Chiorescu, Y. Nakamura, C. J. P. M. Harmans, and J. E. Mooij. *Coherent quantum dynamics of a superconducting flux qubit.* Science **299**, 1869–1871 (2003).

[4] T. Yamamoto, Y. A. Pashkin, O. Astafiev, Y. Nakamura, and J.-S. Tsai. *Demonstration of conditional gate operation using superconducting charge qubits.* Nature **425**, 941 (2003).

[5] F. W. Strauch, P. R. Johnson, A. J. Dragt, C. J. Lobb, J. R. Anderson, and F. C. Wellstood. *Quantum logic gates for coupled superconducting phase qubits.* Phys. Rev. Lett. **91**, 167005 (2003).

[6] C. Foley and H. Hilgenkamp. *Why nanoSQUIDs are important: an introduction to the focus issue.* Supercond. Sci. Technol. **22**, 064001 (2009).

[7] C. A. Hamilton, R. L. Kautz, R. L. Steiner, and F. L. Lloyd. *A practical Josephson voltage standard at 1 V.* IEEE Electron Device Lett. **6**, 623–625 (1985).

[8] J. Niemeyer, L. Grimm, W. Meier, J. Hinken, and E. Vollmer. *Stable Josephson reference voltages between 0.1 and 1.3 V for high-precision voltage standards.* Appl. Phys. Lett. **47**, 1222–1223 (1985).

[9] M. Tinkham. *Introduction to superconductivity: second edition.* (Dover Publications, 2004).

[10] C. W. J. Beenakker, *Three "universal" mesoscopic josephson effects*, in Transport phenomena in mesoscopic systems, edited by H. Fukuyama and T. Ando (1992), pp. 235–253.

[11] R. C. Dynes and T. A. Fulton. *Supercurrent density distribution in Josephson junctions.* Phys. Rev. B **3**, 3015–3023 (1971).

[12] `https://graphene-flagship.eu/` (visited on 2018-04-09).

[13] Y. Ren, X. Deng, Z. Qiao, C. Li, J. Jung, C. Zeng, Z. Zhang, and Q. Niu. *Single-valley engineering in graphene superlattices.* Phys. Rev. B **91**, 245415 (2015).

[14] M. Yankowitz, J. Xue, D. Cormode, J. D. Sanchez-Yamagishi, K. Watanabe, T. Taniguchi, P. Jarillo-Herrero, P. Jacquod, and B. J. LeRoy. *Emergence of superlattice Dirac points in graphene on hexagonal boron nitride.* Nature Phys. **8**, 382 (2012).

[15] C. Gutiérrez, C.-J. Kim, L. Brown, T. Schiros, D. Nordlund, E. B. Lochocki, K. M. Shen, J. Park, and A. N. Pasupathy. *Imaging chiral symmetry breaking from Kekulé bond order in graphene.* Nature Phys. **12**, 950 (2016).

[16] C. W. Groth, M. Wimmer, A. R. Akhmerov, and X. Waintal. *Kwant: a software package for quantum transport.* New J. Phys. **16**, 063065 (2014).

[17] M. Wimmer. *Quantum transport in nanostructures: from computational concepts to spintronics in graphene and magnetic tunnel junctions.* PhD thesis (University of Regensburg, 2009-12).

[18] L. Kadanoff and G. Baym. *Quantum statistical mechanics: Green's function methods in equilibrium and nonequilibrium problems.* (W.A. Benjamin, 1962).

[19] V. S. Pribiag, A. J. Beukman, F. Qu, M. C. Cassidy, C. Charpentier, W. Wegscheider, and L. P. Kouwenhoven. *Edge-mode superconductivity in a two-dimensional topological insulator.* Nature Nanotech. **10**, 593 (2015).

[20] C. Liu, T. L. Hughes, X.-L. Qi, K. Wang, and S.-C. Zhang. *Quantum spin Hall effect in inverted type-II semiconductors.* Phys. Rev. Lett. **100**, 236601 (2008).

[21] L. Du, I. Knez, G. Sullivan, and R.-R. Du. *Robust helical edge transport in gated InAs/GaSb bilayers*. Phys. Rev. Lett. **114**, 096802 (2015).

[22] C. W. J. Beenakker, D. I. Pikulin, T. Hyart, H. Schomerus, and J. P. Dahlhaus. *Fermion-parity anomaly of the critical supercurrent in the quantum spin-Hall effect*. Phys. Rev. Lett. **110**, 017003 (2013).

[23] S.-P. Lee, K. Michaeli, J. Alicea, and A. Yacoby. *Revealing topological superconductivity in extended quantum spin Hall Josephson junctions*. Phys. Rev. Lett. **113**, 197001 (2014).

[24] U. Essmann and H. Träuble. *The direct observation of individual flux lines in type II superconductors*. Phys. Lett. A **24**, 526–527 (1967).

[25] J. C. Cuevas and F. S. Bergeret. *Magnetic interference patterns and vortices in diffusive SNS junctions*. Phys. Rev. Lett. **99**, 217002 (2007).

[26] A. Abrikosov. *The magnetic properties of superconducting alloys*. J. Phys. Chem. Solids **2**, 199–208 (1957).

[27] C.-Y. Hou, C. Chamon, and C. Mudry. *Electron fractionalization in two-dimensional graphenelike structures*. Phys. Rev. Lett. **98**, 186809 (2007).

[28] V. Cheianov, V. Fal'ko, O. Syljuåsen, and B. Altshuler. *Hidden Kekulé ordering of adatoms on graphene*. Solid State Communications **149**, 1499–1501 (2009).

[29] J. A. M. van Ostaay, A. R. Akhmerov, C. W. J. Beenakker, and M. Wimmer. *Dirac boundary condition at the reconstructed zigzag edge of graphene*. Phys. Rev. B **84**, 195434 (2011).

[30] G. Tkachov, P. Burset, B. Trauzettel, and E. M. Hankiewicz. *Quantum interference of edge supercurrents in a two-dimensional topological insulator*. Phys. Rev. B **92**, 045408 (2015).

[31] I. Knez, R.-R. Du, and G. Sullivan. *Andreev reflection of helical edge modes in InAs/GaSb quantum spin Hall insulator*. Phys. Rev. Lett. **109**, 186603 (2012).

[32] S. Hart, H. Ren, T. Wagner, P. Leubner, M. Mühlbauer, C. Brüne, H. Buhmann, L. W. Molenkamp, and A. Yacoby. *Induced superconductivity in the quantum spin hall edge.* Nature Phys. **10**, 638 (2014).

[33] X. Shi, W. Yu, Z. Jiang, B. Andrei Bernevig, W. Pan, S. Hawkins, and J. Klem. *Giant supercurrent states in a superconductor-InAs/GaSb-superconductor junction.* J. Appl. Phys. **118**, 133905 (2015).

[34] H.-Y. Hui, A. M. Lobos, J. D. Sau, and S. Das Sarma. *Proximity-induced superconductivity and Josephson critical current in quantum spin Hall systems.* Phys. Rev. B **90**, 224517 (2014).

[35] U. Smilansky. *Exterior–interior duality for discrete graphs.* J. Phys. A **42**, 035101 (2009).

[36] J. T. Chalker and P. D. Coddington. *Percolation, quantum tunnelling and the integer Hall effect.* J. Phys. C: Solid State Physics **21**, 2665 (1988).

[37] B. Kramer, T. Ohtsuki, and S. Kettemann. *Random network models and quantum phase transitions in two dimensions.* Phys. Rep. **417**, 211–342 (2005).

[38] Y. Jiang, X. Lu, and F. Zhai. *Standard form of the scattering matrix for time reversal symmetric system.* arXiv:1310.3733 (2013).

[39] C. W. J. Beenakker. *Universal limit of critical-current fluctuations in mesoscopic Josephson junctions.* Phys. Rev. Lett. **67**, 3836–3839 (1991).

[40] P. Brouwer and C. Beenakker. *Anomalous temperature dependence of the supercurrent through a chaotic Josephson junction.* Chaos, Solitons & Fractals **8**, Chaos and Quantum Transport in Mesoscopic Cosmos, 1249–1260 (1997).

[41] U. Ledermann, A. L. Fauchère, and G. Blatter. *Nonlocality in mesoscopic josephson junctions with strip geometry.* Phys. Rev. B **59**, R9027–R9030 (1999).

[42] V. Barzykin and A. M. Zagoskin. *Coherent transport and nonlocality in mesoscopic SNS junctions: anomalous magnetic interference patterns.* Superlatt. Microstruct. **25**, 797–807 (1999).

[43] J. P. Heida, B. J. van Wees, T. M. Klapwijk, and G. Borghs. *Nonlocal supercurrent in mesoscopic Josephson junctions*. Phys. Rev. B **57**, R5618–R5621 (1998).

[44] Y. Harada, S. Jensen, T. Akazaki, and H. Takayanagi. *Anomalous magnetic flux periodicity of supercurrent in mesoscopic SNS josephson junctions*. Physica C **367**, 229–233 (2002).

[45] L. Fu and C. L. Kane. *Josephson current and noise at a superconductor/quantum-spin-Hall-insulator/superconductor junction*. Phys. Rev. B **79**, 161408 (2009).

[46] Q.-Z. Wang, X. Liu, H.-J. Zhang, N. Samarth, S.-C. Zhang, and C.-X. Liu. *Quantum anomalous hall effect in magnetically doped InAs/GaSb quantum wells*. Phys. Rev. Lett. **113**, 147201 (2014).

[47] S. V. Mironov, A. S. Mel'nikov, and A. I. Buzdin. *Double path interference and magnetic oscillations in cooper pair transport through a single nanowire*. Phys. Rev. Lett. **114**, 227001 (2015).

[48] C. Li, A. Kasumov, A. Murani, S. Sengupta, F. Fortuna, K. Napolskii, D. Koshkodaev, G. Tsirlina, Y. Kasumov, I. Khodos, R. Deblock, M. Ferrier, S. Guéron, and H. Bouchiat. *Magnetic field resistant quantum interferences in josephson junctions based on bismuth nanowires*. Phys. Rev. B **90**, 245427 (2014).

[49] D. Giuliano and I. Affleck. *The Josephson current through a long quantum wire*. J. Stat. Mech. Theory Exp. **2013**, P02034 (2013).

[50] E. Akkermans, A. Auerbach, J. E. Avron, and B. Shapiro. *Relation between persistent currents and the scattering matrix*. Phys. Rev. Lett. **66**, 76–79 (1991).

[51] M. Z. Hasan and C. L. Kane. *Colloquium: Topological insulators*. Rev. Mod. Phys. **82**, 3045–3067 (2010).

[52] C. L. Kane and E. J. Mele. *Quantum spin Hall effect in graphene*. Phys. Rev. Lett. **95**, 226801 (2005).

[53] M. König, S. Wiedmann, C. Brüne, A. Roth, H. Buhmann, L. W. Molenkamp, X.-L. Qi, and S.-C. Zhang. *Quantum spin Hall insulator state in HgTe quantum wells*. Science **318**, 766–770 (2007).

[54] B. van Wees, G. Meijer, J. Kuipers, T. Klapwijk, W. v. d. Graaf, and G. Borghs. *Breakdown of the quantum hall effect in InAs/AlSb quantum wells due to counterflowing edge channels*. Phys. Rev. B **51**, 7973–7976 (1995).

[55] B.-M. Nguyen, A. A. Kiselev, R. Noah, W. Yi, F. Qu, A. J. A. Beukman, F. K. de Vries, J. van Veen, S. Nadj-Perge, L. P. Kouwenhoven, M. Kjaergaard, H. J. Suominen, F. Nichele, C. M. Marcus, M. J. Manfra, and M. Sokolich. *Decoupling edge versus bulk conductance in the trivial regime of an InAs/GaSb double quantum well using corbino ring geometry.* Phys. Rev. Lett. **117**, 077701 (2016).

[56] F. Nichele, H. J. Suominen, M. Kjaergaard, C. M. Marcus, E. Sajadi, J. A. Folk, F. Qu, A. J. A. Beukman, F. K. de Vries, J. van Veen, S. Nadj-Perge, L. P. Kouwenhoven, B.-M. Nguyen, A. A. Kiselev, W. Yi, M. Sokolich, M. J. Manfra, E. M. Spanton, and K. A. Moler. *Edge transport in the trivial phase of InAs/GaSb.* New J. Phys. **18**, 083005 (2016).

[57] I. Tamm. *On the possible bound states of electrons on a crystal surface.* Phys. Z. Soviet Union **1** (1932).

[58] W. Shockley. *On the surface states associated with a periodic potential.* Phys. Rev. **56**, 317–323 (1939).

[59] J. Bardeen. *Surface states and rectification at a metal semiconductor contact.* Phys. Rev. **71**, 717–727 (1947).

[60] A. Furukawa. *Dependence of electron accumulation in AlSb/InAs quantum well on thin surface materials of InAs and GaSb.* Appl. Phys. Lett. **62**, 3150–3152 (1993).

[61] L. Ö. Olsson, C. B. M. Andersson, M. C. Håkansson, J. Kanski, L. Ilver, and U. O. Karlsson. *Charge accumulation at InAs surfaces.* Phys. Rev. Lett. **76**, 3626–3629 (1996).

[62] K. Flensberg, J. B. Hansen, and M. Octavio. *Subharmonic energy-gap structure in superconducting weak links.* Phys. Rev. B **38**, 8707–8711 (1988).

[63] M. T. Allen, O. Shtanko, I. C. Fulga, A. Akhmerov, K. Watanabe, T. Taniguchi, P. Jarillo-Herrero, L. S. Levitov, and A. Yacoby. *Spatially resolved edge currents and guided-wave electronic states in graphene.* Nature Phys. **12**, 128 (2016).

[64] W. Haberkorn, H. Knauer, and J. Richter. *A theoretical study of the current-phase relation in Josephson contacts.* Phys. Status Solidi A **47**, K161–K164 (1978).

[65] A. Rasmussen, J. Danon, H. Suominen, F. Nichele, M. Kjaergaard, and K. Flensberg. *Effects of spin-orbit coupling and spatial symmetries on the Josephson current in SNS junctions*. Phys. Rev. B **93**, 155406 (2016).

[66] H. J. Suominen, J. Danon, M. Kjaergaard, K. Flensberg, J. Shabani, C. J. Palmstrøm, F. Nichele, and C. M. Marcus. *Anomalous Fraunhofer interference in epitaxial superconductor-semiconductor Josephson junctions*. Phys. Rev. B **95**, 035307 (2017).

[67] M. Ben Shalom, M. Zhu, V. Fal'ko, A. Mishchenko, A. Kretinin, K. Novoselov, C. Woods, K. Watanabe, T. Taniguchi, A. Geim, et al. *Quantum oscillations of the critical current and high-field superconducting proximity in ballistic graphene*. Nature Phys. **12**, 318–322 (2016).

[68] T. Yokoyama, M. Eto, and Y. V. Nazarov. *Josephson current through semiconductor nanowire with spin–orbit interaction in magnetic field*. J. Phys. Soc. Jpn. **82**, 054703 (2013).

[69] H. Meier, V. I. Fal'ko, and L. I. Glazman. *Edge effects in the magnetic interference pattern of a ballistic SNS junction*. Phys. Rev. B **93**, 184506 (2016).

[70] S. Russo, M. Kroug, T. M. Klapwijk, and A. F. Morpurgo. *Experimental observation of bias-dependent nonlocal Andreev reflection*. Phys. Rev. Lett. **95**, 027002 (2005).

[71] J. A. M. van Ostaay, A. R. Akhmerov, and C. W. J. Beenakker. *Spin-triplet supercurrent carried by quantum hall edge states through a Josephson junction*. Phys. Rev. B **83**, 195441 (2011).

[72] P. Recher, E. V. Sukhorukov, and D. Loss. *Andreev tunneling, Coulomb blockade, and resonant transport of nonlocal spin-entangled electrons*. Phys. Rev. B **63**, 165314 (2001).

[73] A. Furusaki. *DC Josephson effect in dirty SNS junctions: numerical study*. Physica B **203**, 214–218 (1994).

[74] J. M. Rowell. *Magnetic field dependence of the josephson tunnel current*. Phys. Rev. Lett. **11**, 200–202 (1963).

[75] V. E. Calado, S. Goswami, G. Nanda, M. Diez, A. R. Akhmerov, K. Watanabe, T. Taniguchi, T. M. Klapwijk, and L. M. Vandersypen. *Ballistic Josephson junctions in edge-contacted graphene*. Nature Nanotech. **10**, 761–764 (2015).

[76] S. Hart, H. Ren, M. Kosowsky, G. Ben-Shach, P. Leubner, C. Brüne, H. Buhmann, L. W. Molenkamp, B. I. Halperin, and A. Yacoby. *Controlled finite momentum pairing and spatially varying order parameter in proximitized HgTe quantum wells.* Nature Phys. **13**, 87 (2017).

[77] M. Kim, D. Jeong, G.-H. Lee, Y.-S. Shin, H.-W. Lee, and H.-J. Lee. *Tuning locality of pair coherence in graphene-based Andreev interferometers.* Sci. Rep. **5**, 8715 (2015).

[78] F. Bergeret and J. Cuevas. *The vortex state and Josephson critical current of a diffusive sns junction.* J. Low Temp. Phys. **153**, 304–324 (2008).

[79] M. Alidoust, G. Sewell, and J. Linder. *Non-fraunhofer interference pattern in inhomogeneous ferromagnetic josephson junctions.* Phys. Rev. Lett. **108**, 037001 (2012).

[80] M. Alidoust and K. Halterman. *Proximity induced vortices and long-range triplet supercurrents in ferromagnetic Josephson junctions and spin valves.* J. Appl. Phys. **117**, 123906 (2015).

[81] M. Amundsen and J. Linder. *General solution of 2d and 3d superconducting quasiclassical systems: coalescing vortices and nanoisland geometries.* Sci. Rep. **6**, 22765 (2016).

[82] J. Bardeen, R. Kümmel, A. E. Jacobs, and L. Tewordt. *Structure of vortex lines in pure superconductors.* Phys. Rev. **187**, 556–569 (1969).

[83] A. F. Andreev. *The thermal conductivity of the intermediate state in superconductors.* Sov. Phys. JETP **19**, 1228–1231 (1964).

[84] C. W. J. Beenakker and H. van Houten. *Josephson current through a superconducting quantum point contact shorter than the coherence length.* Phys. Rev. Lett. **66**, 3056–3059 (1991).

[85] I. O. Kulik and A. N. Omel'Yanchuk. *Properties of superconducting microbridges in the pure limit.* Sov. J. Low Temp. Phys. (Engl. Transl.) **3**, 459 (1977).

[86] T. Yokoyama, M. Eto, and Y. V. Nazarov. *Anomalous Josephson effect induced by spin-orbit interaction and Zeeman effect in semiconductor nanowires.* Phys. Rev. B **89**, 195407 (2014).

[87] P. Rakyta, A. Kormányos, and J. Cserti. *Magnetic field oscillations of the critical current in long ballistic graphene Josephson junctions*. Phys. Rev. B **93**, 224510 (2016).

[88] M. Z. Hasan, H. Lin, and A. Bansil. *Warping the cone on a topological insulator*. Physics **2**, 108 (2009).

[89] L. Fu. *Hexagonal warping effects in the surface states of the topological insulator* Bi_2Te_3. Phys. Rev. Lett. **103**, 266801 (2009).

[90] O. M. Auslaender, L. Luan, E. W. Straver, J. E. Hoffman, N. C. Koshnick, E. Zeldov, D. A. Bonn, R. Liang, W. N. Hardy, and K. A. Moler. *Mechanics of individual isolated vortices in a cuprate superconductor*. Nature Phys. **5**, 35 (2009).

[91] A. Finkler, D. Vasyukov, Y. Segev, L. Neeman, Y. Anahory, Y. Myasoedov, M. Rappaport, M. Huber, J. Martin, A. Yacoby, and E. Zeldov. *Nano-sized SQUID-on-tip for scanning probe microscopy*. J. Phys. Conf. Ser. **400**, 052004 (2012).

[92] D. Roditchev, C. Brun, L. Serrier-Garcia, J. C. Cuevas, V. H. L. Bessa, M. V. Milošević, F. Debontridder, V. Stolyarov, and T. Cren. *Direct observation of Josephson vortex cores*. Nature Phys. **11**, 332 (2015).

[93] F. Chiodi, M. Ferrier, S. Guéron, J. C. Cuevas, G. Montambaux, F. Fortuna, A. Kasumov, and H. Bouchiat. *Geometry-related magnetic interference patterns in long SNS josephson junctions*. Phys. Rev. B **86**, 064510 (2012).

[94] B. Crouzy and D. A. Ivanov. *Magnetic interference patterns in long disordered Josephson junctions*. Phys. Rev. B **87**, 024514 (2013).

[95] A. Fert. *Origin, development, and future of spintronics*. Angew. Chem. Int. Ed. **47**, Nobel lecture, 5956–5967 (2008).

[96] D. Awschalom and N. Samarth. *Trend: spintronics without magnetism*. Physics **2**, 50 (2009).

[97] T. Kuschel and G. Reiss. *Spin orbitronics: charges ride the spin wave*. Nat. Nanotech. **10**, 22 (2015).

[98] P. Recher and B. Trauzettel. *A defect controls transport in graphene*. Physics **4**, 25 (2011).

[99] D. Pesin and A. H. MacDonald. *Spintronics and pseudospintronics in graphene and topological insulators*. Nature Mater. **11**, 409 (2012).

[100] C. Mudry. *Two-dimensional materials: heavy going*. Nature Phys. **12**, 895 (2016).

[101] C. Gutiérrez. *Visualizing ordered electronic states in epitaxial graphene*. PhD thesis (Columbia University, 2015).

[102] C. Chamon. *Solitons in carbon nanotubes*. Phys. Rev. B **62**, 2806–2812 (2000).

[103] V. V. Cheianov, O. Syljuåsen, B. L. Altshuler, and V. Fal'ko. *Ordered states of adatoms on graphene*. Phys. Rev. B **80**, 233409 (2009).

[104] K. K. Gomes, W. Mar, W. Ko, F. Guinea, and H. C. Manoharan. *Designer Dirac fermions and topological phases in molecular graphene*. Nature **483**, 306 (2012).

[105] G. Giovannetti, P. A. Khomyakov, G. Brocks, P. J. Kelly, and J. van den Brink. *Substrate-induced band gap in graphene on hexagonal boron nitride: ab initio density functional calculations*. Phys. Rev. B **76**, 073103 (2007).

[106] G. Giovannetti, M. Capone, J. van den Brink, and C. Ortix. *Kekulé textures, pseudospin-one dirac cones, and quadratic band crossings in a graphene-hexagonal indium chalcogenide bilayer*. Phys. Rev. B **91**, 121417 (2015).

[107] A. H. Castro Neto, F. Guinea, N. M. R. Peres, K. S. Novoselov, and A. K. Geim. *The electronic properties of graphene*. Rev. Mod. Phys. **81**, 109–162 (2009).

[108] C. W. J. Beenakker. *Andreev reflection and Klein tunneling in graphene*. Rev. Mod. Phys. **80**, 1337–1354 (2008).

[109] Y. Aharonov and A. Casher. *Ground state of a spin-1/2 charged particle in a two-dimensional magnetic field*. Phys. Rev. A **19**, 2461–2462 (1979).

[110] X. G. Wen and A. Zee. *Winding number, family index theorem, and electron hopping in a magnetic field*. Nucl. Phys. B **316**, 641–662 (1989).

[111] M. I. Katsnelson and M. F. Prokhorova. *Zero-energy states in corrugated bilayer graphene*. Phys. Rev. B **77**, 205424 (2008).

[112] J. Kailasvuori. *Pedestrian index theorem à la Aharonov-Casher for bulk threshold modes in corrugated multilayer graphene*. Europhys. Lett. **87**, 47008 (2009).

[113] S. K. Wang and J. Wang. *Valley precession in graphene superlattices*. Phys. Rev. B **92**, 075419 (2015).

[114] B. Trauzettel, D. V. Bulaev, D. Loss, and G. Burkard. *Spin qubits in graphene quantum dots*. Nature Phys. **3**, 192 (2007).

[115] M. Polini, F. Guinea, M. Lewenstein, H. C. Manoharan, and V. Pellegrini. *Artificial honeycomb lattices for electrons, atoms and photons*. Nature Nanotech. **8**, 625 (2013).

Summary

In this thesis we study quantum transport phenomena on the nanometer scale, in two classes of materials: topological insulators with induced superconductivity and graphene superlattices. Both topics are motivated by recent experimental developments: the first topic arose from the search for Majorana fermions in a quantum spin Hall insulator, the second topic arose from the search for massive Dirac fermions in the Kekulé band structure of graphene on a copper substrate.

The first two chapters address the experimental observation in Delft of an h/e-periodic component in the magnetic-field dependence of the critical supercurrent in a Josephson junction formed out of a quantum spin Hall insulator. This doubled Fraunhofer periodicity is suggestive of the appearance of Majorana zero-modes in the junction, however the theory presented in Chapter 2 indicates a more mundane explanation. Using a network model of an edge-conducting Josephson junction, we demonstrate that the existence of a conducting channel along the normal-superconductor interface can explain the coexistence of h/e and $h/2e$ Fraunhofer periodicities — without requiring any contribution from Majorana fermions.

In the next Chapter 3 we describe our collaboration with the experimentalists in Delft to test our theory against new experimental data. We take into account the details of the experimental setup, which lead to partial screening of the normal part of the Josephson junction from the gate electrode. Using a realistic tight-binding model, we could explain the observations along the lines of the theory of the preceding chapter.

In Chapter 4 we continue our study of Josephson junctions in a different system, the conducting surface of a three-dimensional topological insulator. The circular Fermi surface of free electrons has a square deformation, which as we have found strongly influences the lattice of magnetic vortices. Unlike the one-dimensional array of Josephson vortices of pre-

vious studies, we find a fully two-dimensional vortex lattice. We predict that this vortex lattice leads to observable effects in the decay rate of the Fraunhofer oscillations. The lattice might also be directly measurable using scanning tunneling microscopy.

In Chapter 5 we turn to the second topic of our thesis, the superlattice of a carbon monolayer (graphene) on an epitaxial substrate. Experiments on a graphene/copper superlattice had observed a periodic modulation of the potential with a structure that resembles the Kekulé dimerization of a benzene ring. The conclusion from the published experiments was that this modulation converts the massless Dirac fermions of graphene into massive electrons, by opening a band gap at the Dirac point. We have found that the physics of this problem is different: the electrons remain massless, but the superlattice potential introduces a coupling between the valley degree of freedom and the momentum. This valley-momentum locking could be useful in so-called valleytronics applications.

Samenvatting

In dit proefschrift onderzoeken wij quantum transportverschijnselen op de nanometerschaal, in twee type materialen: topologische isolatoren met geïnduceerde supergeleiding en superroosters in grafeen. Beide onderwerpen zijn gemotiveerd door recente experimentele ontwikkelingen: het eerste onderwerp ontstond uit de zoektocht naar Majorana fermionen in een quantum-spin-Hall-isolator, het tweede onderwerp ontstond uit de zoektocht naar massieve Dirac fermionen in de Kekulé bandstructuur van grafeen op een koper-substraat.

In de eerste twee hoofdstukken onderzoeken wij de experimentele waarneming in Delft van een h/e-periodieke component in de magneetveldafhankelijkheid van de kritische superstroom in een Josephsonjunctie die gevormd is uit een quantum-spin-Hall-isolator. Deze verdubbelde Fraunhoferperiodiciteit suggereert de aanwezigheid van Majoranadeeltjes in de junctie, echter de theorie in hoofdstuk 2 geeft een minder exotische interpretatie. Gebruikmakend van een netwerkmodel van randgeleiding in een Josephsonjunctie tonen wij aan dat het optreden van een geleidend kanaal langs de grens tussen het normale materiaal en de supergeleider heel goed het samengaan van h/e en $h/2e$ Fraunhoferperiodiciteiten kan verklaren — zonder dat er een bijdrage nodig is van Majorana fermionen.

Hoofdstuk 3 betreft een samenwerking met de experimentatoren in Delft, waarin we onze theorie testen aan nieuwe waarnemingen. We houden rekening met de details van het experiment, in het bijzonder de gedeeltelijke afscherming van het normale deel van de Josephsonjunctie door de metalen elektrodes. Gebruikmakend van een realistische roostermodel kunnen we de experimenten verklaren volgens de theorie van het voorafgaande hoofdstuk.

In hoofdstuk 4 vervolgen we de studie van Josephsonjuncties in een ander systeem, het geleidende oppervlak van een drie-dimensionale topologische isolator. Het circulaire Fermi-oppervlak van vrije elektronen

heeft een vierkante vervorming, die een sterke invloed blijkt te hebben op het rooster van magnetische vortices. Een één-dimensionaal rooster van Josephson-vortices is bekend uit eerder werk, wij vinden echter een volledig twee-dimensionaal vortexrooster. We voorspellen dat dit rooster waarneembare consequenties heeft voor de vervalsnelheid van de Fraunhofer-oscillaties. Het rooster zou ook direct waarneembaar kunnen zijn met behulp van een rastermicroscoop.

In hoofdstuk 5 gaan we over tot het tweede onderwerp van het proefschrift, het superrooster van een koolstof-monolaag (grafeen) dat epitaxiaal gegroeid is op een substraat. Experimenten aan een grafeen/koper superrooster hadden een periodieke modulatie waargenomen van de elektrische potentiaal, met een struktuur die lijkt op de periodieke modulatie van de bindingen in een benzeenring (bekend als Kekulé dimerisatie). De conclusie van de gepubliceerde experimenten was dat deze modulatie de massaloze Dirac-fermionen in grafeen omzet in gewone massieve elektronen. Wij hebben echter gevonden dat het probleem heel anders in elkaar zit: de elektronen blijven massaloos, maar wat het superrooster bewerkt is dat er een koppeling optreedt tussen de beweging van de elektronen en hun "valley" vrijheidsgraad. Deze "valley-momentum locking" zou toegepast kunnen worden in het vakgebied van de "valleytronics" (een variant op "spintronics" waar de elektronspin vervangen wordt door de "valley" pseudo-spin).

Підсумки

У цій дисертації ми вивчаємо явище квантового транспорту на рівні нанометрових розмірів у двох класах матеріалів: топологічних ізоляторах з наведеною надпровідністю і суперґратках графену. Обидва напрямки мотивовані сучасними експериментальними наробками: перший напрямок є результатом пошуку майоранівських ферміонів у системах з квантовим спіновим ефектом Хола, другий — з пошуку масивних дираківських ферміонів у зонній структурі графену на мідній підкладці, у якому виникає модуляція міжатомних зв'язків типу Кекуле.

Перші дві глави присвячені експериментам, зробленим у Делфті, які виявили h/e-періодичну компоненту у залежності критичного надпровідного струму від магнітного поля у джозефсонівському контакті, зробленому з ізолятору з квантовим спіновим ефектом Хола. Ця подвоєна фраунгоферівська періодичність натякає на появу майоранівських нульових мод у контакті, проте теорія, презентована у Главі 2 надає тривіальніше пояснення. За допомогою сіткової моделі ми демонструємо, що існування провідного каналу на границі між надпровідником і ізолятором може пояснити співіснування h/e- і $h/2e$-періодичних компонент, потребуючи існування майоранівських нульових мод.

У наступній Главі 3 ми описуємо колаборацію з експериментаторами з університету Делфта, де ми перевіряємо цю теорію за допомогою нових експериментальних даних. Ми враховуємо деталі експериментальної установки, які приводять до часткового екранування нормальної частини джозефсонівського контакту від електричного поля затвору. За допомогою реалістичної моделі найближчих сусідів ми змогли пояснити це явище, базуючись на теорії, представленій у попередній главі.

У Главі 4 ми продовжуємо вивчати джозефсонівські контакти у іншій системі, поверхні тривимірного топологічного ізолятора, яка є

провідником. Поверхня Фермі електронів без взаємодії деформується від круглої до квадратної, що сильно впливає на формування магнітних вихорів. На відміну від одновимірного розташування джозефсонівських вихорів, яке було відомо з попередніх досліджень, ми знайшли повноцінну двовимірну вихрову ґратку. Ми прогнозуємо, що ця ґратка приводить до помітного уповільнення у затуханні фраунгоферівських осциляцій при збільшенні поперечного магнітного поля. Вона може також бути виявлена напряму за допомогою скануючої тунельної мікроскопії.

У Главі 5 ми звертаємось до другої теми цій дисертації, суперґратки у одноатомному шарі вуглецю (графені) на епітаксіальній підкладці. Експерименти з графеном на мідній підкладці продемонстрували існування періодичної модуляції у енергії взаємодії між атомами карбону, яка нагадує димерізацію типу Кекуле у кільці бензолу. Висновок опублікованої експериментальної статті стверджує, що така модуляція перетворює безмасові дираківскі ферміони у спектрі графену у масивні, тобто відкриває щілину у спектрі. Ми демонструємо, що поведінка системи у цьому випадку інакша: електрони залишаються ефективно безмасовими, але суперґратка приводить до взаємодії між імпульсом і долиною у графенівському спектрі. Цей зв'язок долини і імпульсу може бути корисним для використання у "долинотроніці" (за аналогією до спінтроніки).

Curriculum Vitæ

I was born in Lugansk, Ukraine (at that time part of the Soviet Union), on the 21st of May 1991, and received there my primary and secondary education (at Municipal School №57). I started advanced study in physics already then, being a regular participant of the Ukrainian State Physics Olympiad (in the years 2005–2008).

After graduating from school in 2008, I started my study in Taras Shevchenko National University of Kyiv at the Faculty of Physics. After two years of study I chose the specialization in theoretical physics. I obtained my Bachelor (2012, red diploma, equivalent to *cum laude*) and Master (2014) degrees under the supervision of Prof. Dr. Bohdan Lev (head of the Synergetics department in the Boholyubov Institute for Theoretical Physics). The title of my master thesis was "Phase transitions in two-dimensional electron systems on the surface of liquid helium". This work also resulted in my first publication.

During my master study I held a part-time job at Samsung Research Ukraine as a software engineer. This provided me much experience at working in industry and helped me to acquire advanced software development skills.

In 2014 I joined the group of Prof. Dr. Carlo Beenakker at the Instituut-Lorentz of Leiden University as a Ph.D. student, employed by the Foundation for Fundamental Research on Matter (FOM). I collaborated with the theoretical nanoscience group of Dr. Anton Akhmerov and Dr. Michael Wimmer at Delft University of Technology. I greatly benefited from the opportunity to work with experimentalists in the group of Prof. Dr. Ir. Leo Kouwenhoven at QuTech in Delft.

During my Ph.D. study I was a teaching assistant for the theoretical condensed matter physics course. I presented my research at workshops, schools, and conferences in The Netherlands, Ukraine, Spain, and Italy.

List of Publications

- B. I. Lev, V. P. Ostroukh, V. B. Tymchyshyn, and A. G. Zagorodny. *Statistical description of the system electrons on the liquid helium surface.* Eur. Phys. J. B **87**, 253 (2014).

- B. Baxevanis, V. P. Ostroukh, and C. W. J. Beenakker. *Even-odd flux quanta effect in the Fraunhofer oscillations of an edge-channel Josephson junction.* Phys. Rev. B **91**, 041409(R) (2015) [Chapter 2].

- V. P. Ostroukh, B. Baxevanis, A. R. Akhmerov, and C. W. J. Beenakker. *Two-dimensional Josephson vortex lattice and anomalously slow decay of the Fraunhofer oscillations in a ballistic SNS junction with a warped Fermi surface.* Phys. Rev. B **94**, 094514 (2016) [Chapter 4].

- K. Zuo, V. Mourik, D. B. Szombati, B. Nijholt, D. J. van Woerkom, A. Geresdi, J. Chen, V. P. Ostroukh, A. R. Akhmerov, S. R. Plissard, D. Car, E. P. A. M. Bakkers, D. I. Pikulin, L. P. Kouwenhoven, and S. M. Frolov. *Supercurrent interference in few-mode nanowire Josephson junctions.* Phys. Rev. Lett. **119**, 187704 (2017).

- F. K. de Vries, T. Timmerman, V. P. Ostroukh, J. van Veen, A. J. A. Beukman, F. Qu, M. Wimmer, B.-M. Nguyen, A. A. Kiselev, W. Yi, M. Sokolich, M. J. Manfra, C. M. Marcus, and L. P. Kouwenhoven. *h/e superconducting quantum interference through trivial edge states in InAs.* Phys. Rev. Lett. **120**, 047702 (2018) [Chapter 3].

- O. V. Gamayun, V. P. Ostroukh, N. V. Gnezdilov, İ. Adagideli, and C. W. J. Beenakker. *Valley-momentum locking in a graphene su-*

perlattice with Y-shaped Kekulé bond texture. New J. Phys. **20**, 023016 (2018) [Chapter 5].

- C. W. J. Beenakker, N. V. Gnezdilov, E. Dresselhaus, V. P. Ostroukh, İ. Adagideli, and J. Tworzydło. *Valley switch in a graphene superlattice due to pseudo-Andreev reflection.* arXiv:1805.02487.

Stellingen

behorende bij het proefschrift

Lattice models for Josephson junctions and graphene superlattices

1. The doubled Fraunhofer periodicity observed in an edge-channel Josephson junction can be explained by the appearance of a conducting channel along the interface with the superconductor.

   Chapter 2

2. The SQUID-like Fraunhofer diffraction pattern observed in InAs quantum wells is not conclusive evidence for topologically protected edge channels.

   Chapter 3

3. A non-circular Fermi surface may induce a two-dimensional vortex lattice in the normal region of a ballistic Josephson junction.

   Chapter 4

4. An index theorem protects the valley degeneracy of the lowest Landau level in the presence of valley-momentum locking.

   Chapter 5

5. Contrary to the claim by Gutiérrez *et al.*, the Kekulé bond texture in a graphene-on-copper superlattice does not produce a gapped spectrum.

   C. Gutiérrez *et al.*, Nature Phys. **12**, 950 (2016).

6. The topologically protected valley switch in a graphene superlattice, reported by Beenakker *et al.* for electron reflection, exists also in transmission.

   C. W. J. Beenakker *et al.*, Phys. Rev. B **97**, 241403(R) (2018).

7. The Dynes-Fulton relationship, used to reconstruct the current density from the magnetic-field dependence of the Josephson effect, can be relied upon only in tunnel junctions.

   R. C. Dynes and T. A. Fulton, Phys. Rev. B **3**, 3015 (1971).

8. The dispersion relation of a spin-1 Weyl semimetal can be understood as the effect of a non-Abelian gauge field, by application of the theory of de Juan.

   F. de Juan, Phys. Rev. B **87**, 125419 (2013).

Viacheslav Ostroukh

27 June 2018